Materials Advances

ROYAL SOCIETY OF CHEMISTRY

REVIEW

View Article Online
View Journal



Cite this: DOI: 10.1039/d6ma00306k

# Additive manufacturing of biodegradable metals for medical implants: current progress, key challenges, and future perspectives

Dayanidhi Krishana Pathak,†[a] Ajit Kumar,†[bc] Muralidhar Yadav,†[cd] Pawan Sharma,*[e] Jiaojiao Wang,[d] Parth Patankar,[f] Nichenametla Jai Sai,[g] Dipesh Kumar Mishra,[h] Girish Chandra Verma[i] and Rohit Kumar Singh Gautam[j]

The additive manufacturing process (AM) plays a vital role in the medical field, such as manufacturing surgical tools, models, implants, and medical equipment, owing to its capability to fabricate customized and intricate shape parts. Although considerable development is shown in the research area of the AM processes compared to traditional methods for the fabrication of metal-based degradable biomaterials, *viz.*, iron (Fe), magnesium (Mg), and zinc (Zn), it is still at an early stage. It may be noted that while Zn has a medium degradation rate and strong biocompatibility, the AM is difficult due to porosity issues and element loss. These complications are primarily due to evaporation under a high-energy electron beam during melting. While Mg is biocompatible and possesses sufficient mechanical properties comparable to human bone, its nature is explosive and corrosive. Fe has good mechanical properties and the highest strength relative to Mg and Zn; its degradation rate is poor. Thus, all these biodegradable materials have unique benefits and drawbacks, making the bioimplant manufacturing methodology for each substance distinctive. This work has conducted an extensive review of the mechanical, corrosion behaviour, and biological properties of different degradable biomaterials using different AM techniques. The effect of AM techniques on different materials and their final product properties has been studied in this review. The characteristics of the final product depend on the materials, design, processing, and application that make biodegradable metals (BMs) a typical subject that covers various fields of study, such as biomaterials, engineering, and medicine.

Received 5th March 2026,
Accepted 20th April 2026

DOI: 10.1039/d6ma00306k

rsc.li/materials-advances



## 1. Introduction

### 1.1 Biomaterials and implants

An implant is an artificial device surgically introduced into the human body to support, restore, or replace damaged biological structures, or to enhance the performance of existing tissues. The long-term success of an implant depends on several factors, such as biomaterial type, biomechanics, host biological tissues, and physiological service conditions. Over the past several decades, significant advances in materials science have enabled the replacement of numerous anatomical components.[1–19] Biomaterials are defined as substances, other than pharmaceuticals, that are designed to deal with biological systems for the treatment, replacement, or augmentation of tissues, organs, or physiological functions. Despite extensive material development, no foreign material is completely inert within the human body.[20] When implanted, synthetic materials cause a host tissue response whose nature and severity depend strongly on the material's chemistry, structure, and surface properties. Consequently, material availability, biocompatibility,

[a] Department of Mechanical Engineering, G.B. Pant Govt. Engineering College (now G.B. Pant DSEU Campus), New Delhi, 110020, India
[b] Department of Smart Manufacturing, New Age Makers Institute of Technology (NAMTECH), Gandhinagar, Gujarat, 382355, India
[c] Department of Materials Engineering, Indian Institute of Science, Bangalore, 560012, India
[d] School of Materials Science and Engineering, Nanyang Technological University, 50 Nanyang Avenue, Singapore, 639798, Singapore
[e] Department of Mechanical Engineering, Indian Institute of Technology-Banaras Hindu University, Varanasi, 221005, India. E-mail: pawan.mec@iitbhu.ac.in
[f] School of Chemistry, Chemical Engineering and Biotechnology, Nanyang Technological University, 62 Nanyang Drive, 637459, Singapore
[g] Department of Materials Science and Metallurgy, University of Cambridge, 27 Charles Babbage Road, Cambridge, CB3 0FS, UK
[h] Department of Mechanical Engineering, Madan Mohan Malviya University of Technology, Gorakhpur, Uttar Pradesh, 273016, India
[i] Department of Mechanical Engineering, Indian Institute of Technology, Indore, 453552, India
[j] Department of Mechanical Engineering, Teerthanker Mahaveer University, Moradabad, 244001, India
† These authors contributed equally to this work.

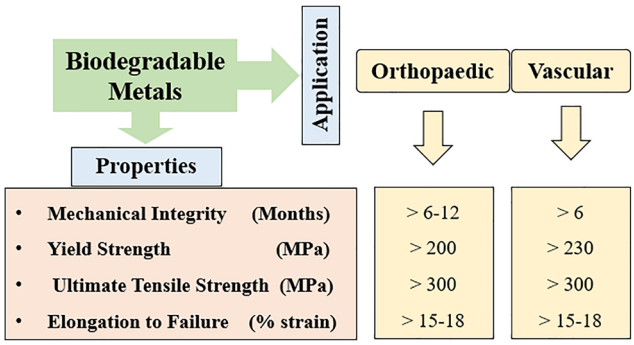


Fig. 1 Desired mechanical properties for biodegradable implant materials based on the applications.[21]

and bifunctionality are critical requirements for implantable biomaterials. Fig. 1 represents the minimal mechanical properties of biodegradable implants as per their application in vascular and orthopedic devices.[21] Biomaterials are commonly classified into three categories based on their interaction with biological tissues.[22] Bioinert materials exhibit minimal interaction with surrounding tissues and include titanium and its alloys, stainless steel, zirconia, and ultra-high-molecular-weight polyethylene. Bioactive materials actively interact with bone or soft tissues and promote interfacial bonding; examples include hydroxyapatite, bioglass, and glass-ceramics. Bioresorbable materials are designed to degrade progressively *in vivo* and be replaced by regenerating tissue, with magnesium, iron, zinc, polyglycolic acid (PGA), and polylactic acid (PLA) being common examples.

### 1.2 Biodegradable metals and applications

Biodegradable metals (BMs) are designed to degrade gradually within the body while primarily providing mechanical support during tissue regeneration, particularly in orthopaedic, paediatric, and cardiovascular applications. Unlike polymeric biodegradable materials, BMs combine controlled degradation with mechanical properties comparable to those of conventional metals. Ideally, biodegradable metals corrode *in vivo* at a controlled rate, elicit an acceptable host response to corrosion products, and fully dissolve after fulfilling their functional role, without leaving residual stress or harmful by-products.[23] Among the various candidates investigated to date, magnesium (Mg), iron (Fe), and zinc (Zn) are the most extensively studied biodegradable metals. These materials are used in the form of pure metals, alloys, or biodegradable metal matrix composites. While impurity levels influence the corrosion behaviour of pure metals, alloying elements such as lithium, calcium, strontium, manganese, and tin are commonly introduced to tailor mechanical performance and degradation rates. However, the selection and concentration of alloying elements must be carefully controlled to avoid adverse toxicological and physiological effects arising from ionic release in the body.[24,25] Zinc exhibits a moderate degradation rate and good biocompatibility, making it attractive for biodegradable implant applications. Nevertheless, additive manufacturing of Zn remains challenging due to evaporation, porosity formation, and relatively low mechanical strength, issues that are primarily associated with high-energy beam-based melting processes.[26,27] Magnesium, by contrast, offers excellent biocompatibility and mechanical properties comparable to human bone, but its high corrosion rate, hydrogen evolution, and flammability greatly limit its structural integrity and clinical applicability.[28,29] Alloying strategies and surface modifications have therefore been widely explored to mitigate these limitations.[30–32] Fe possesses superior mechanical strength and ductility in comparison to Mg and Zn; however, its slow degradation rate restricts its use as a fully biodegradable implant material. Strategies such as introducing porosity have been shown to accelerate iron corrosion, while its essential biological roles in oxygen transport, electron transfer, and enzymatic catalysis further support its biocompatibility.[21,24,33] Additive manufacturing has emerged as a promising approach for fabricating biodegradable metal implants, enabling the production of customizable geometries with controlled porosity and complex architectures. AM enables layer-by-layer fabrication directly from three-dimensional digital models, offering design freedom beyond that of conventional manufacturing techniques. Powder bed fusion (PBF) methods are the most widely explored for biodegradable metals owing to the availability of metallic powders, while alternative techniques such as inkjet printing, fused filament fabrication, and binder-based approaches followed by sintering have also been reported. Compared with other biomaterials, metals offer higher toughness, wear resistance, ductility, and load-bearing capability, making them particularly suitable for orthopaedic devices, bone plates, screws, dental implants, and cardiovascular stents. Though Mg-, Fe-, and Zn-based biodegradable metal implants have demonstrated promising preclinical and early clinical outcomes, significant challenges remain. In particular, the fabrication of porous, mechanically robust scaffolds with precisely controlled degradation behaviour remains difficult using conventional routes. Additive manufacturing, therefore, represents a critical enabling technology for advancing biodegradable metal implants toward widespread clinical translation.

Although a substantial body of literature exists on the additive manufacturing of biodegradable metals, most previously published reviews predominantly focus on individual material systems, particularly Mg-based or Zn-based alloys, or emphasize specific processing techniques.[34–36] Recent studies have further highlighted the role of additive manufacturing and composite design strategies in tailoring the degradation behaviour and biological performance of biodegradable metallic biomaterials.[37] A comprehensive and comparative understanding across the three major biodegradable metal systems – Mg, Zn, and Fe remains limited. The present review distinguishes itself by providing an integrated analysis of additive manufacturing of biodegradable metals through a process-structure–property–performance framework, enabling a deeper understanding of how manufacturing parameters influence microstructure, mechanical behaviour, degradation characteristics, and biological response. Furthermore, this work offers a systematic comparative evaluation of Mg-, Zn-, and Fe-based alloys,

highlighting their relative advantages, limitations, and suitability for specific biomedical applications such as orthopedic implants and cardiovascular stents. In addition, emerging aspects such as machine learning-assisted additive manufacturing and advanced design strategies are incorporated to provide insights into future research directions. Therefore, this review aims to bridge the gap between materials selection, additive manufacturing processes, and clinical performance, offering a comprehensive perspective that is not fully addressed in existing literature.

## 2. The current scenario in manufacturing of Mg, Zn, and Fe-based BMs

Due to their beneficial mechanical characteristics and biocompatibility, biodegradable metallic biomaterials (BMs), especially based on magnesium (Mg), zinc (Zn), and iron (Fe), have demonstrated considerable promise for use in bone grafting and medical implant applications. But even with their benefits, this field's study is still infancy in many aspects. Making BM porous scaffolds with customized macro- and micro-architectures that properly match each patient's anatomical characteristics is a significant problem. For the best mechanical performance, osseointegration, and cell ingrowth, these porous structures are crucial.

### 2.1 Conventional manufacturing techniques and limitations

Metallic biomaterial (BM) scaffolds have long been made using conventional manufacturing techniques such as casting, powder metallurgy (PM), machining, and forming, each of which has unique benefits and drawbacks. Because of its affordability and versatility, casting remains one of the most traditional and widely used methods. Mg-based BMs are often produced by die casting and sand casting.[36] However, because of its strong oxygen reactivity, magnesium requires controlled conditions to avoid porosity and oxidation, which can weaken its mechanical properties. Sand casting is more cost-effective, but it frequently results in uneven cooling and poor surface finish, which, if left untreated, can impair fatigue performance. Die casting is the recommended method for producing precise parts in large quantities, such as orthopedic implants. Although brittleness and defects such as cracks and pinholes continue to be problems, zinc (Zn) alloys, which are commonly alloyed with copper and aluminum, are also cast for medical applications, such as dental implants and temporary orthopedic devices.[38] Casting, especially stainless steel and cast iron, is used in a similar manner to treat Fe-based BMs.[39] However, the high melting point and density of Fe make processing difficult, frequently resulting in porosity and uneven composition that necessitate post-processing to enhance biocompatibility and degradation resistance. For the fabrication of porous implants that promote bone ingrowth, PM offers an alternate manufacturing method that allows for exact control over composition and porosity.[40] PM techniques use space-holder agents to create regulated, interconnected porosity in Mg-based BMs.[18] PM is essential for creating biodegradable Mg-based implants and can produce magnesium–zinc scaffolds with porosity like that of cancellous bone, thereby enhancing mechanical compatibility and biointegration. Controlling the reactivity of magnesium powder and preserving material purity are still challenging tasks, nevertheless.[41] Like this, PM allows for customized porosity in Zn-based biomaterials, however because of low-temperature sintering limitations, mechanical strength may be compromised.[42] PM also helps Fe-based biomaterials by allowing for the modification of breakdown rates and the creation of extremely porous structures that are essential for tissue integration.[40] However, contamination and oxidation during processing continue to be significant issues. Additional approaches for precisely sculpting biomaterials based on Mg, Zn, and Fe are provided by machining and forming procedures. Researchers employ CNC machining, milling, and turning to make implants with complex, patient-specific geometry.[43] Although magnesium is comparatively machinable, its low ductility and reactivity make it vulnerable to tool wear and fire hazards.[44] Although zinc-based materials often have smooth surfaces, they need careful cutting control to avoid flaws.[45,46] Stainless steel and other Fe-based biomaterials are widely machined for use in dental and joint implants, despite their high hardness, which requires specialist tools and increases production costs due to material waste.[47] Mechanical properties are further improved through forming techniques such as extrusion and forging. While temperature control is crucial, forging enhances grain structure, strength, and fatigue resistance, making it appropriate for orthopedic applications. Extrusion is frequently utilized for magnesium[48] and Zn[16] components, such as stents, since it provides consistent mechanical properties and near-net-shape efficiency; nonetheless, issues with tool wear and process sensitivity still exist. Because of its hardness, forging is more popular for Fe,[49] whereas extrusion is only used rarely when consistent cross-sections are needed. Traditional manufacturing techniques are useful but have limitations. They frequently have adverse environmental effects, significant energy consumption, and material waste.[50] It is challenging to achieve controlled porosity and ideal surface quality, both of which are necessary for tissue integration and biocompatibility. These methods may introduce impurities or alter the material's properties, and they are not flexible enough to produce complex geometries or gradient materials. Production costs are further raised by the need for trained labour, high tooling costs, and maintenance requirements.[51] To improve customisation, efficiency, and performance for next-generation metallic biomaterials, the sector is progressively investigating cutting-edge alternatives like hybrid fabrication, sustainable processing, and additive manufacturing.

### 2.2 Additive manufacturing solutions

Additive manufacturing (AM) has evolved as a revolutionary approach to overcoming the limitations of conventional fabrication methods for biodegradable metal implants.[52] Layer-by-layer manufacturing directly from digital models is made possible by AM, which offers unprecedented control over geometry, internal architecture, and porosity, while minimizing

material waste,[51,53,54] AM techniques make it easier to produce complicated implants with complex lattice structures tailored to each patient[55] that promote osseointegration and allow precise tuning of mechanical properties and degradation behaviour.[55,56]

Compared to traditional routes, AM offers enhanced design freedom, improved porosity control,[51] reduced tool wear, and improved cost-effectiveness for customized or low-volume production. Furthermore, the ability to fabricate functionally graded materials and complex porous architectures positions AM as a key enabling technology for next-generation biodegradable implants. Consequently, AM is increasingly recognized as a critical pathway for advancing Mg-, Zn-, and Fe-based biodegradable metals toward clinical translation.

## 3. Additive manufacturing of biodegradable metals

AM provides unmatched design flexibility and complexity by adding material precisely where needed, in contrast to subtractive processes that cut a final shape out of a block of material. This technology is applied to various industries, including aerospace and medicine. It facilitates quick prototyping, product customization, and the production of complex geometries that were previously impractical or unfeasible. Fig. 2 represents the schematics of various metal AM processes commonly used to fabricate biomedical products.

### 3.1 Mg-based BMs

Because of their design capabilities, the AM process of Mg and its alloys became more popular than traditional manufacturing, thereby enhancing their potential for biodegradable implant development. AM of Mg has been demonstrated using laser powder bed fusion (LPBF),[58–64,66–72,124] capillary-mediated binder less 3D printing,[19] inkjet 3D printing,[73] and the fused filament fabrication (FFF) method.[74] These methods use different raw materials and different process mechanisms, where different AM components are fabricated. Even highly complex structures can be easily fabricated. Pure Mg has a density of 1.74 g $cm^{-3}$, and pure cast Mg samples have an ultimate tensile property of around 90 MPa. However, the Mg alloys' strength can be increased to 200–300 MPa through suitable alloying and refinement. Biocompatible elements like Zn, Ca, Sr, and Si, and earth elements like Gd, Nd, Sc, and Y, are acceptable for biodegradable Mg-based alloys.[75] In 2010, by combining a shielding box and an Nd: YAG laser system, Ng *et al.*[62,76] developed the SLS system and successfully melted the Mg tracks, showing a possible alternative to traditional approaches for manufacturing Mg scaffolds. However, oxidation effects that restrict a wider choice of laser powers and scan speeds for efficient processing were observed. Furthermore, surface contamination, internal oxidation, and poor wetting were reported,

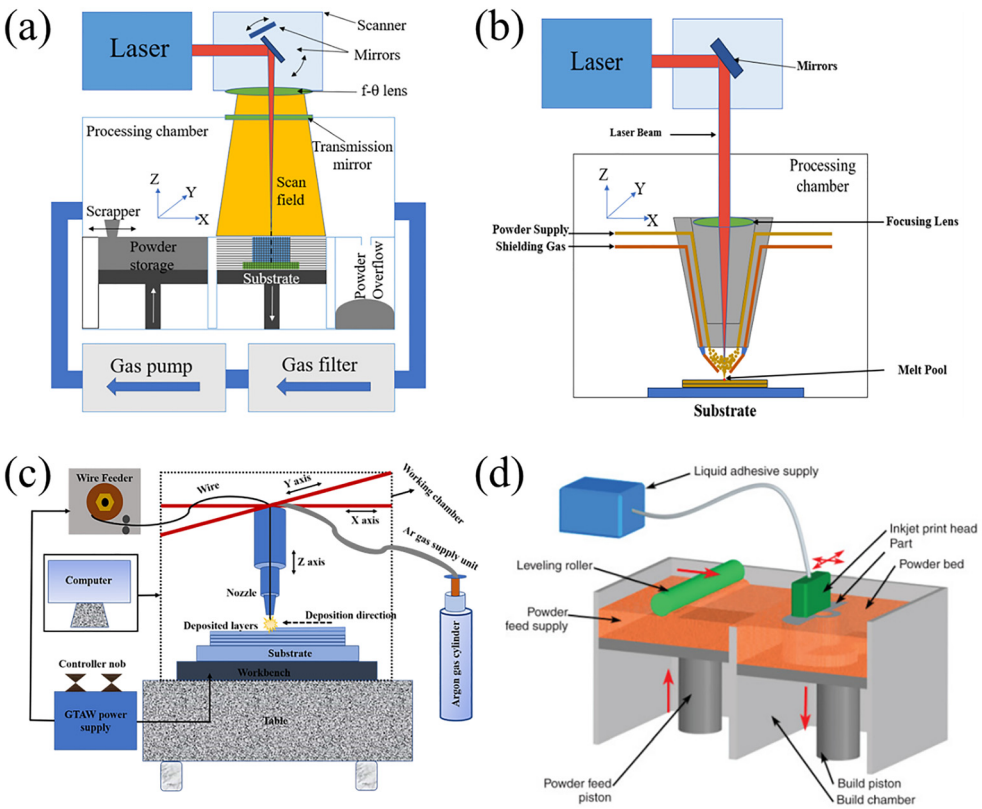


Fig. 2 Schematic representation of (a) LPBF process; (b) laser engineering net shaping (LENS); (c) wire arc AM process; (d) binder jetting (reproduced from ref. 57 with permission from Elsevier, Copyright 2018).

resulting in significant degradation of the material and component geometry. Similarly, the same group performed a study to analyze the effect of process factors on the microstructure by multi-layer melting of Mg powders.[58] The pulsed laser over the continuous laser was utilized to enhance surface performance, owing to the higher peak force, so that the oxide powder coating could be melted. The hardness value in the melted zone rose as the grain size reduced and lowered as the laser's energy density increased.[58]

Zhang *et al.*[59] reported the fabrication of pure Mg and pure Al alloy using selective laser melting (SLM). A low relative density value, *i.e.*, 82%, was attained due to a low laser energy absorption rate and low scanning speed. Wei *et al.*[72] compared the properties of LPBF-fabricated AZ91D Mg alloy with the as-cast AZ91D alloy. It was reported that LPBF-fabricated AZ91D alloy samples exhibited superior microhardness and tensile properties. Zumdick *et al.*[60] compared mechanical behaviour and microstructural properties of as-cast, powder-extruded, and additively manufactured WE43 Mg samples. An LPBF method was employed for preparing the WE43 Mg samples. It was concluded that additively manufactured WE43 Mg possessed a higher tensile strength than as-cast and powder-extruded samples. Kumar *et al.* recently developed a Mg–Ag–Sn based biomedical alloy *via* novel *in situ* alloying with excellent properties.[77]

An efficient LPBF system for preparing Mg parts for implants was reported in 2016 by Yang *et al.*[63] It was found that at the optimum laser energy density of 10 J mm$^{-3}$, the dense Mg components could be obtained without forming pores or cracks. Furthermore, its degradation behaviour was analyzed by immersing the LPBF Mg component in simulated body fluid (SBF). A slow degradation rate during the latter immersion period was observed owing to the formation of $Mg(OH)_2$, which acts as the protective layer and delays the contact between Mg and SBF solution. Nopova *et al.*[78] processing of AZ91D alloy demonstrated that relative densities exceeding 99% can be achieved under optimized parameters, although Mg evaporation slightly alters alloy composition during LPBF. Laser power and laser speed in the range of 150–210 W and 325–750 mm s$^{-1}$ respectively was used. Finally, it was reported that highly dense Mg samples were found at laser power = 180 W, scanning speed = 612.5 mm s$^{-1}$, hatch distance = 0.133 mm and layer thickness = 0.05 mm. Subsequent investigations have focused on optimizing process parameters such as laser power and scan speed to control melt pool stability. Moderate laser power combined with relatively high scan speeds is often preferred to limit excessive heat accumulation and evaporation while ensuring sufficient fusion. Reviews on LPBF of biodegradable Mg alloys indicate that maintaining a balanced thermal input is essential to suppress defects such as balling at low energy density ($E_v$) and vapor-induced porosity at high $E_v$.[79] Although $E_v$ values are not always explicitly reported, typical optimal ranges for Mg alloys are generally inferred to lie between ~50 and 150 J mm$^{-3}$, depending on alloy composition and system configuration. In the context of porous structures, LPBF has enabled the fabrication of Mg-based scaffolds with controlled architectures for biomedical applications. Similar to Zn systems, achieving high strut density while maintaining designed porosity requires careful optimization of $E_v$. Studies report that moderate energy densities (~80–130 J mm$^{-3}$) can produce dense struts with minimal defects, ensuring adequate mechanical integrity and corrosion performance.

The microstructural, electrochemical behaviour, *in vitro* corrosion, and biocompatibility of samples prepared by LPBF of mechanically mixed Mg powders, such as Mg–*x*Zn,[124] Mg–*x*Sn,[71] Mg–*x*Mn,[67] Mg–Sn–Zn,[68] Mg (JBDM powder)[19] and Mg–Zn–Zr[69,70] alloys, were studied and recorded. In this context, the *in vitro* properties of porous Mg alloy scaffolds prepared with LPBF of WE43 powder were studied for the first time, and their mechanical properties were reported to be sufficiently strong for proper mechanical support. In addition, the mechanical properties after 4 weeks of biodegradation were recorded, and it was found that the mechanical integrity was in the range desired for supporting trabecular bone. The completely interlinked porous structure was established with explicit topology control, and the corrosion rate of the biomaterials was acceptable after 28 days, with approximately 20% volume loss. Additively manufactured porous Mg scaffolds displayed cytotoxicity of <25% non-viable cells (*i.e.*, level 0 cytotoxicity) after a direct interaction with MG-63 for 72 h.[61]

Meenashisundaram *et al.*[73] manufactured a partially degradable Ti–Mg composite with good compressive and cytotoxicity characteristics using 3D inkjet printing for implant applications. A capillary-mediated pressure less infiltration technique followed the 3D printing process. The corrosion rate obtained for Ti–Mg composite was 23.44 μm per year for 5 days of immersion and 937.48 μm per year for 1 h immersion at 37 °C, respectively, using the NaCl immersion test. To demonstrate the viability of the semi-solid FFF process, Lima *et al.*[74] developed a biodegradable Mg–38Zn alloy scaffold, showcasing AM technology from novel perspectives. Table 5 summarizes the detailed findings from the reported works on developing fabrication techniques of Mg-based metals using AM. Fig. 3 provides a brief illustration of the various examples of 3D printing Mg scaffolds.[61,63,80,81]

### 3.2 Zn-based BMs

Pure Zn possesses inferior mechanical properties. It has a maximum tensile strength of about 20 MPa; however, its strength could be improved up to 200–600 MPa, greater than Mg alloys, with proper alloying and refining.[75] Lietaert *et al.*[82] used $N_2$-atomized and air-atomized pure Zn powders for direct metal printing (DMP) to fabricate pure Zn cubes having a high relative density of >99.70% DMP was found not suitable for nitrogen atomized Zn fabrication as the melted tracks look very unstable, mostly caused by powder morphology, but the parts by air atomized powder show good quality melted tracks. Zn samples were created using an open process container and a gas jet using the LPBF technique.[83] The purpose of such an arrangement was to avoid laser beam scattering and incomplete fusion, which were observed due to low vaporization temperature in a closed chamber. Part density higher than

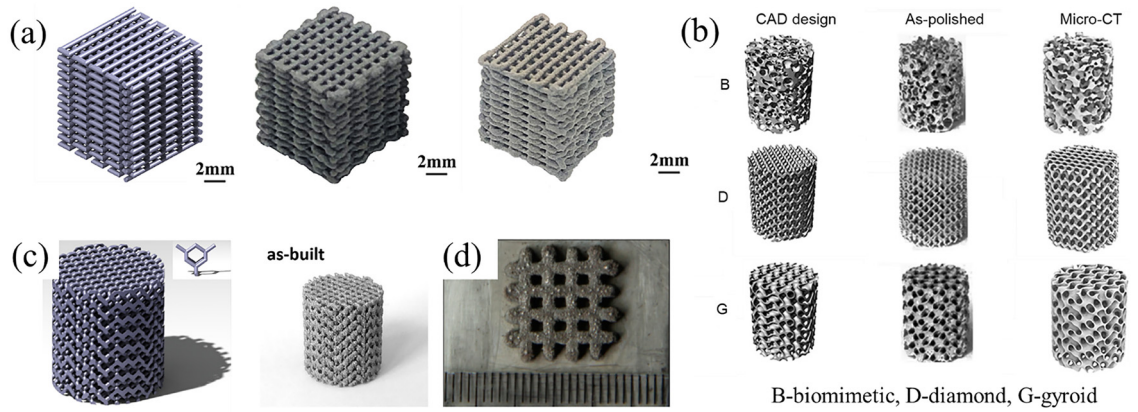


Fig. 3 Various examples of 3D printed porous Mg scaffold (a) CAD design, printed and sintered sample (reproduced from ref. 80 with permission from Elsevier, Copyright 2020); (b) CAD model, as polished and Micro-CT architectures of samples (reproduced from ref. 81 under Creative Common License from Elsevier, Copyright 2020); (c) CAD model and as-sintered 3D printed scaffold (reproduced from ref. 61 with permission from Elsevier, Copyright 2018); (d) 3D printed Mg part fabricated at laser energy density of 10 J $mm^{-1}$ (reproduced from ref. 63 with permission from Taylor & Francis, Copyright 2016).

99% was obtained under stable operating conditions. For the laser energy range varying from 40–115 J $mm^{-3}$, 98% density of the parts was obtained. Furthermore, it was observed that the microhardness of the parts formed by LPBF was found to be in the region between extruded Zn–0.15Mg and cold-worked pure Zn.

Wen *et al.*[84] analyzed the parameters such as densification, surface quality, and mechanical properties of Zn powder during the LPBF. High density greater than 99.50% was obtained with Hatch spacing ($H_s$ = 70 μm), layer thickness ($D_s$ = 30 μm), and volume energy ($E_v$) varying from 60 to 135 J $mm^{-3}$. High densification and good surface quality were achieved through sufficient processing power, optimal laser energy, moderate overlap remelting during LPBF, and control over the material properties of the Zn powder. Zn parts processed using LPBF have greater mechanical properties than those produced using other production techniques, which makes them more suitable for use as biodegradable implants. Qin *et al.*[85] used the LPBF process to fabricate Zn-*x*WE43 porous scaffolds. For all the used samples of various WE43 compositions of pure Zn under the same processing conditions, high densification of over 99.47% was achieved, and with increasing content of WE43, the tensile strength increased, and elongation decreased, which can be observed in Zn-5WE43 that had the highest tensile strength of 335.4 MPa, but the elongation was only 1% is obtained. Furthermore, Zn-8WE43 demonstrated a significantly higher processing porosity, which means that optimized processing conditions need to be modified according to alloy composition. Deng *et al.*[68] fabricated high-performance GZ112K alloy by LPBF technique, and the mechanical properties yield strength (162 MPa), ultimate tensile strength (122 MPa), and comparable elongation (0.4%), which were higher compared to as-cast alloy, were obtained at optimal processing values of scanning speed (300–700 mm $s^{-1}$) and hatch spacing (100 μm). In another study, Yang *et al.*[86] used a technique of combining rapid solidification using LPBF to maximize the mechanical properties of Zn. Also, Zn–*x*Mg (*x* = 0–4 wt%) alloys were evaluated as degradable load-bearing bone implants for their viability, where Zn–3Mg showed positive results of high mechanical properties with a yield strength (152.4 ± 4.8 MPa), ultimate tensile strength (222.3 ± 8.2 MPa), and elongation (7.2 ± 0.4%). Moreover, an acceptable degradation rate and good cytocompatibility with human MG-63 cells were obtained; it is therefore perfect for biodegradable implants. Similarly, to strengthen the mechanical properties *via* the LPBF method, Shuai *et al.*[87] introduced Ag into Zn; the $AgZn_3$ phase was produced when the content of Ag in Zn was increased, resulting in more grain refinement. Consequently, there was an approximate 100% increase in compressive strength and an 116% rise in hardness. However, with higher Ag content, the rapid increase in the $AgZn_3$ phase was observed, resulting in the grains coarsening, thereby resulting in a reduction in the mechanical properties. Due to galvanic corrosion, the Zn–*x*Ag alloys had a higher corrosion rate than Zn. Zn alloys with Ag were reported to be promising biomaterials for bone repair. Table 6 presents the data and findings of previously reported studies on the fabrication of Zn-based BMs using AM. Fig. 4 shows various shapes of 3D printed Zn-based BM samples.[88–90] Wen *et al.*[91] investigated the influence of processing parameters on the densification of Zn using an LPBF system equipped with a specialized gas circulation system to minimize issues such as Zn evaporation. While $E_v$ was not explicitly reported, it can be calculated from the laser spot size (75 μm), layer thickness (30 μm), laser power (60–120 W), hatch spacing (60–120 μm), and scan speed (400–1200 mm $s^{-1}$). Densities above 99% were obtained for $E_v$ values between 33 and 167 J $mm^{-3}$, whereas insufficient energy ($E_v$ < 30 J $mm^{-3}$) led to poor fusion and densities below 95%. In subsequent work, they studied the relationship between $E_v$, laser power, and scan speed, identifying an optimal $E_v$ range of 60–135 J $mm^{-3}$ for high-density parts with porosity under 0.5%. Lower $E_v$ caused incomplete fusion and cavities, while higher $E_v$ induced Zn evaporation and gas entrapment.

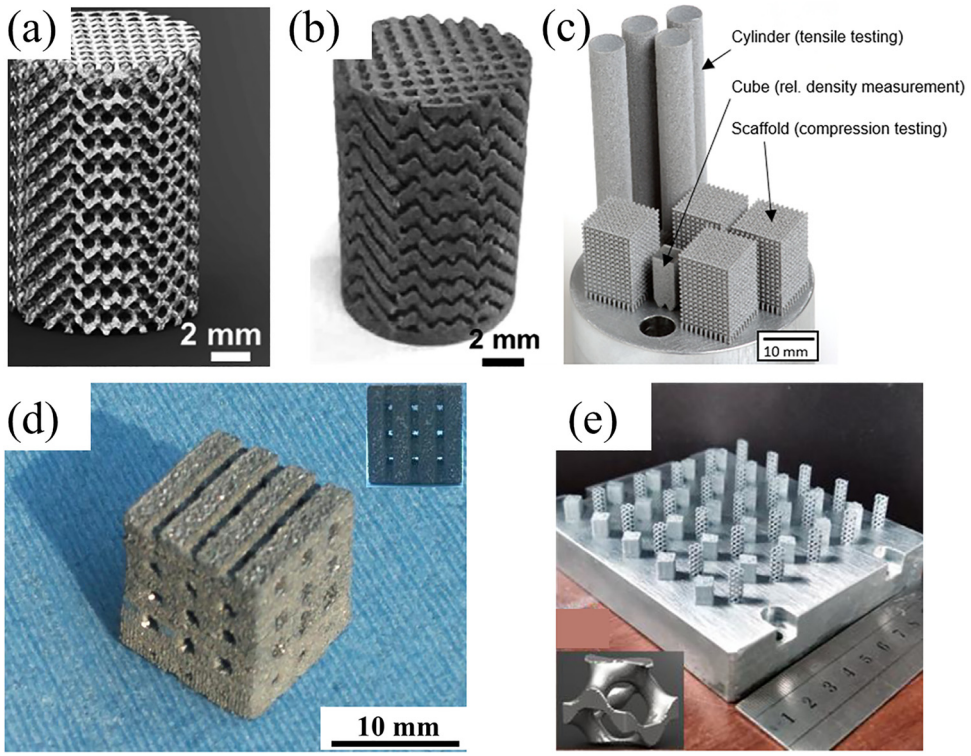


Fig. 4 Illustration of various AM fabricated samples (a) porous scaffold design (b) as-fabricated Zn–*x*Mg *via* LPBF (reproduced from ref. 92 with permission from Elsevier, Copyright 2022); (c) various 3D shaped LPBF manufactured samples (reproduced from ref. 88 with permission from Elsevier, Copyright 2022); (d) macro morphology of Zn–Mg–Ag alloy scaffold prepared using SLM (reproduced from ref. 89 under Creative Common License from Elsevier, Copyright 2022); (e) as fabricated Zn–0.7Li samples (inset showing the gyroid unit in design) (reproduced from ref. 90 with permission from Elsevier, Copyright 2022).

Building on these results, later studies applied optimized $E_v$ ranges to fabricate both bulk parts and porous scaffolds. For example, Zn scaffolds printed at $E_v$ = 95.2 J mm$^{-3}$ achieved strut densities exceeding 99.8%, and bulk parts reached relative densities above 99.5% with $E_v$ values between 54.4 and 126.9 J mm$^{-3}$. Zn alloys often required parameter adjustments from pure Zn to maintain high densification. Qin *et al.*[85] produced Zn-*x*WE43 ($x$ = 2, 5, 8 wt%) samples, achieving densities above 99%, though higher WE43 content (8 wt%) slightly reduced relative density. Similarly, Shuai *et al.*[232] optimized processing of Zn–2Al, identifying a stable $E_v$ range of 76–133 J mm$^{-3}$ for smooth track formation; lower or excessively high $E_v$ caused defects such as balling, incomplete fusion, or powder evaporation. Zn alloys with Mg, Li, and Ce have also been successfully processed. Yang *et al.*[93] fabricated Zn–*x*Mg ($x$ = 0–4 wt%) bulk parts at $E_v$ = 125 J mm$^{-3}$, with the highest density (98.2%) achieved at 3 wt% Mg, while porous scaffolds of pre-alloyed Zn–*x*Mg powders reached strut densities above 99.5% using $E_v$ = 100 J mm$^{-3}$.

Overall, these studies highlight the importance of energy density in LPBF of Zn and its alloys. Proper $E_v$ control ensures sufficient fusion, minimal porosity, and mitigates evaporation, while optimal ranges depend on material composition, geometry, and alloying elements. These insights provide a foundation for producing high-density Zn-based components and scaffolds, particularly for biomedical applications where structural integrity and reliability are critical.

### 3.3 Fe-based BMs

In comparison with Mg and Zn, Fe exhibits a comparatively delayed corrosion rate, which is the fundamental drawback of its use in biodegradable applications.[94] Additively manufactured Fe-based porous scaffolds demonstrate the potential in degradable implant applications, as the porous structure scaffolds can expedite the degradation process owing to the exposed surface area.[2] It is stated that Fe-based biomaterials and stainless steel have similarities in mechanical properties and the methods of fabrication.[23] Various attempts have been made to study and fabricate porous Fe scaffolds. In 2013, Chou *et al.*[95] reported inkjet 3D printing, a technique to produce Fe–30Mn (wt%) scaffolds using mechanically milled powders. Furthermore, the biocompatibility of 3D-printed Fe–30Mn parts was evaluated using direct and indirect pre-osteoblast MC3T3-E1 cell viability tests. Overall, the findings indicated that Fe–Mn 3-D printed could be beneficial for biomaterial applications, and a porosity of 36.3% was seen in the 3-D printed samples. Similarly, Hong *et al.*[96] examined sintered pallets of Fe–Mn–Ca and Fe–Mn–Mg alloys for corrosion and cytotoxicity properties, and it was observed that due to the addition of Mg or Ca, the corrosion density was increased and

open porosity of 39.3% and 52.9% were observed in Fe–Mn and Fe–Mn–1Ca alloys respectively which are 3D printed using binder jet method. Good cytocompatibility, when tested with MC3T3 cells using MTT cell viability assays, was obtained, and when compared with Fe–Mn alloy, Fe–Mn–1Ca exhibited higher corrosion rates in both electrochemical and immersion corrosion experiments. Sharma *et al.*[97] reported the preparation of hierarchically controlled porous biodegradable Fe30Mn scaffolds through a hybrid AM technique. They employed a combination of SLA 3D printing and pressureless liquid phase sintering. Furthermore, porosity = 23.08, CYS = 127.28 MPa, modulus of elasticity = 25.9 GPa and corrosion rate = 1.23 mmpy was found in the prepared samples. Similarly, Kumar *et al.*[94] fabricated Fe-HA samples using an advanced rapid tooling method. Prepared FeHA samples exhibited good biocompatibility and mechanical properties.

Mishra *et al.*[98] created a method for processing Fe scaffolds with various pore topologies that involves pressure less microwave sintering after micro-extrusion-based 3D printing. It was discovered that the artificial scaffolds' porosity and Young's modulus resembled those of human bone. Furthermore, an increase in the degradation rate in porous structures was reported. A method for manufacturing open-cell porous Fe scaffold using 3D printing and pressure less microwave sintering was reported by Sharma *et al.*[2] Electrochemical studies were used to analyze the porous Fe samples and found that they corroded at a higher rate than the solid Fe sample.[99] The maximum corrosion rate (2.245 ± 0.04 mmpy) obtained with topologically ordered porous iron scaffold (TOPIS) was much higher than the corrosion rate of 0.13 ± 0.01 mmpy in the dense Fe sample. The details of the mechanical characteristics and degradation rate of different Fe-alloy matrices are shown in Table 7.[100] Fig. 5 depicts various designed and fabricated TOPIS samples using 3D printing and rapid tooling techniques.

In general, pertaining to laser based AM process, fiber lasers are commonly used for Fe, with energy densities ranging from 10 to 2500 J $mm^{-3}$ for pure Fe and 10–113 J $mm^{-3}$ for Fe alloys. Palousek *et al.*[104] investigated dense pure Fe fabrication using laser powers of 100–400 W, scan speeds of 0.2–1.4 m $s^{-1}$, and hatch spacings of 90–150 μm at a constant layer thickness of 50 μm. Lower scan speeds (0.2–0.5 m $s^{-1}$) produced high-density parts (80–99%), while higher speeds (0.8–1.4 m $s^{-1}$) reduced density (45–97%), with an optimal window at 0.5–0.8 m $s^{-1}$ and 400 W. Song *et al.*[105] found that near-full density (~100%) was achievable only at 100 W and moderate scan speeds (0.1–0.4 m $s^{-1}$). Lower laser powers (60 and 80 W) or higher scan speeds (0.4–1.4 m $s^{-1}$) led to defects such as delamination, brittle fractures, and high porosity. Shuai *et al.*[106] fabricated dense Fe and Fe–25Mn scaffolds at lower energy density (~20 J $mm^{-3}$) using CW mode. Furthermore, Carluccio *et al.*[107] employed pulsed wave (PW) laser mode to produce both dense pure iron parts and porous scaffolds of pure Fe and Fe–35Mn alloys. Dense components reached a relative density of 99.2% using 200 W laser power, 100 μs pulse duration, 60 μm point spacing, 100 μm hatch spacing, and 50 μm layer thickness, corresponding to an energy density of approximately 67 J $mm^{-3}$.

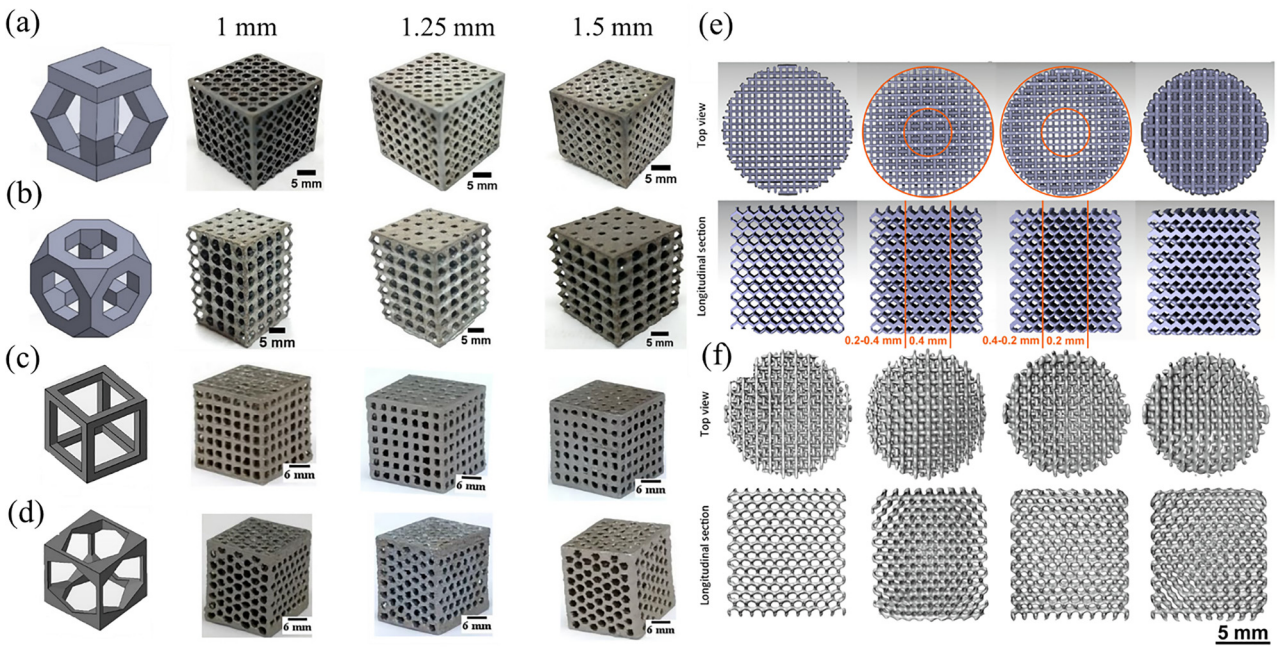


Fig. 5 Designed and fabricated various porous topological ordered Fe scaffold with different strut sizes (a) and (b) truncated octahedron and pyramid using rapid tooling technique (reproduced from ref. 101 with permission from Elsevier, Copyright 2018); (c) and (d), cubic and hexagonal (reproduced from ref. 102 with permission from Elsevier, Copyright 2021) using micro-extrusion-based 3D printing; (e) and (f) Topological design illustrations. Dense-in, dense-out, S0.2, and S0.4, from left to right. From top to bottom: the micro-CT reconstructions of the AM porous individuals' top view and longitudinal cross-section, as well as the top view and longitudinal cross-section derived from CAD models (reproduced from ref. 103 with permission from Elsevier, Copyright 2019).

Scaffold fabrication required slightly different settings: optimal parameters for pure Fe were 150 W, 60 μs, and 50 μm hatch/point spacing, while Fe–35Mn scaffolds performed best at 125 W, 50 μs, and 45 μm spacing. The higher energy requirement for pure Fe (72 J $mm^{-3}$ *vs.* 62 J $mm^{-3}$ for Fe–35Mn) was attributed to its higher melting point. Overall, dense parts require higher energy input and lower scan speeds, whereas scaffolds tolerate lower energy and higher speeds. Too low energy results in poor fusion and high porosity, while excessive energy induces thermal stress and deformation, or reduces lattice porosity by enlarging melt pools.

# 4. Process–parameter–structure–property correlations for additively manufactured biodegradable BMs

Mechanical performance of metallic materials is strongly influenced by microstructural evolution during processing and joining. Studies on welded alloys, pipeline steels, and thermomechanical processed materials have demonstrated that grain morphology, phase transformation, and interfacial characteristics significantly affect strength, hardness, and fracture behaviour.[108–110] Similar microstructure–property relationships govern the performance of additively manufactured biodegradable metals.[111,112] The processing parameters during fabrication significantly impact on the material's mechanical characteristics. The evolution of the microstructure is essential for determining the mechanical properties of metallic systems. Several studies on advanced steels have demonstrated that thermomechanical processing, intercritical annealing, and thermal ageing significantly modify grain refinement, phase distribution, and deformation mechanisms, leading to improved strength-ductility balance and corrosion behaviour.[113–117] These findings highlight the importance of process–structure–property relationships that are also relevant for additively manufactured biodegradable metals. The variance in process parameters has a significant impact on the mechanical characteristics of AM samples; the properties may vary at different locations within a single component. Therefore, in AM processes, an excellent comprehension of the material, process factors, and microstructure advancement is necessary to monitor or strengthen the mechanical properties.

## 4.1 Microstructure and mechanical properties

**4.1.1 Mg-based alloys.** The linear energy density, governed by the combined relationship between laser scan speed and laser power, is the most appealing parameter in LPBF that influences the microstructure of fabricated parts. The effects of linear energy density on the microstructures of continuous-wave LPBF fabricated samples have been reported by Ng *et al.*[62] The surface morphology of the melted zones in the samples at different laser energy densities is depicted in Fig. 6A. Different laser parameters led to variations in the solidification rates of the molten pool, causing dissimilarities in the microstructures of the deposited layers. The surface morphology affirms that all the deposited layers are merely equiaxed α-Mg single phase with highly dense inter-granular boundaries. The mean grain sizes of the deposited layers corresponding to the above-mentioned laser energy density were found to be about 2.30 μm, 2.82 μm, 3.65 μm, 4.10 μm, and 4.87 μm, respectively. As expected, a larger mean grain size was observed for the layers fabricated at increased laser energy density, as increasing laser energy density generally generates higher temperatures during laser melting. Thus, the melted zone with a slower cooling rate presents coarser grains. Lowering the cooling rate during solidification offers an extended time for coarsening of grain.[118] Therefore, increasing the laser energy density would lead to grain coarsening. Such a trend can elucidate the correlation between laser energy density and grain size in the melted region of the specimen, as depicted in Fig. 6D(a). Similarly, as presented in Fig. 6D(b) and (c), increasing the laser power or decreasing the laser scan speed makes the grains coarser in the melted region, as the higher laser power or lower scan speed offered additional driving force for the movement of grain boundaries, thereby supporting the growth of the grains.

The lack of fusion and a significant number of balling powder defects appear as the laser scanning speed rises to 1000 mm $s^{-1}$ in Mg alloy (GZ112K) processed using LPBF and the larger lack of fusion defects detected as the laser would not be able to melt all the powder in large regions.[68] When low hatch spacing was used, lower elongation was observed due to the wide area of overlapping region and poor efficiency of production. So, the LPBF mechanism can be affected by too high or too low hatch spacing. For better mechanical properties, optimum values of 300–700 mm $s^{-1}$ laser scanning speed and 100 μm hatch spacing were reported.[68] So, medium power and relatively slow scanning speed, which can be controlled by a processing parameter known as hatch spacing ($H_s$), have a great influence on the melting and evaporation properties of metals, *i.e.*, to avoid excessive evaporation and provide enough melting.[84] The presence of pores and relative density also influenced the mechanical behaviour of the material formed by PM or binder jet 3D printing, as the presence of pores causes stress concentration promoting crack initiation and propagation defects. So, with an optimal temperature range of 535–610 °C, as the temperature increases, values of density, elastic modulus, and compressive properties are improved for sintered parts of Mg–Zn–Zr alloy.[19] Because the bone tissues' elastic modulus ranges from 3 to 20 GPa, the higher the laser-melted Mg's elastic modulus, the less compatible the implant was with the tissue. The mechanical characteristics of laser-melted Mg were nearly identical to those of natural bone when compared to other metallic biomaterials, such as titanium alloy and stainless steel. As a result, the laser-melted magnesium exhibited a notable decrease in hardness and elasticity, which may have favorable effects as a bone fixation implant in the future. According to the Hall–Petch equation for the melted zone, the melted region hardness value of magnesium decreased as the laser energy density rose.[62] The LPBF processed part's average microhardness, as reported, was 85 to 100 HV, higher than that of traditional die-cast ingot (58 HV).[72] The improvement in microhardness of LPBF processed AZ91D alloy which was

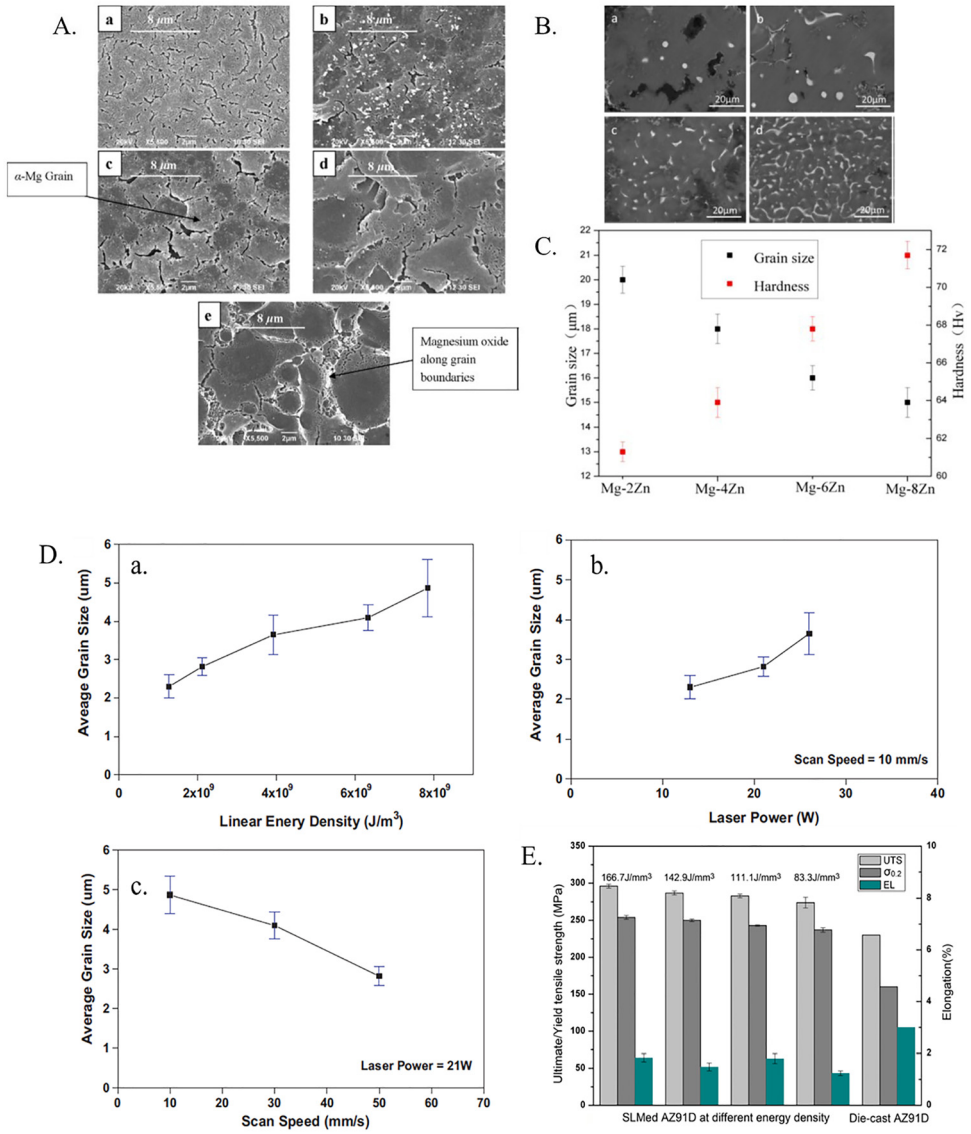


Fig. 6 (A) Surface morphology of the continuous wave laser melted surface deposited at particular laser energy densities (a) 1.27 × $10^9$ J $m^{-2}$, (b) 2.11 × $10^9$ J $m^{-2}$, (c) 3.92 × $10^9$ J $m^{-2}$, (d) 6.33 × $10^9$ J $m^{-2}$, and (e) 7.84 × $10^9$ J $m^{-2}$ (reproduced from ref. 62 with permission from Elsevier, Copyright 2011); (B) microstructure of (a) Mg–2Zn; (b) Mg–4Zn; (c) Mg–6Zn and (d) Mg–8Zn (reproduced from ref. 124 under Creative Common License from MDPI, Copyright 2016); (C) hardness of Mg–Zn alloys with respect to Zn content and grain size (reproduced from ref. 124 under Creative Common License from MDPI, Copyright 2016); (D) variation in the mean grain size under continuous wave irradiation w.r.t (a) laser energy density and (b) laser power and (c) scan speed (reproduced from ref. 62 with permission from Elsevier, Copyright 2011); (E) tensile performance of LPBFed and die-cast AZ91D samples at different $E_v$ values (reproduced from ref. 72 with permission from Elsevier, Copyright 2014).

fabricated at the energy input of 166.7 J $mm^{-3}$ was obtained mainly due to grain refinement, and due to the Al content in α-Mg of Mg–Al alloy using Hall–Petch equation. Fig. 6E shows the mechanical properties of LPBFed AZ91D components which were greater than die-cast AZ91D, though the elongation was dropped.[72] Although Mg possesses promising mechanical properties comparable to those of human bone, it progressively loses mechanical integrity after implantation due to degradation. Thus, to develop Mg-based implants that could sustain their mechanical integrity till recovery, numerous efforts have been made by researchers either by adopting different processing techniques or by implementing alloy design strategies.[1,76,119–122,233] Hardness is one of the considerable mechanical properties that informs whether the materials, especially alloys, could be acceptable for bone implants or not.[123] The content of the Mg matrix plays a prominent role in increasing the hardness of samples owing to the establishment of MgZn precipitated phases that act as a reinforcement. These phases work as hard particles and progressively boost the hardness as the size of the precipitated phases increases.[124] Moreover, grain refinement is driven by the cumulative presence of the MgZn phase and rapid solidification, both of which are encouraging factors for improving mechanical properties, particularly in hexagonal close-packed (HCP) Mg.[125] Fig. 6C shows the relation between the hardness of the MgZn

alloys regarding grain size and Zn content.[124] The research work shows that in compliance with the Hall–Petch model, grain refining increases the hardness of the biodegradable Mg sections. The LPBF-printed Mg holds its hardness between the range of 0.4 to 1.2 GPa.[75] The LPBF-manufactured product has good mechanical properties as it possesses refined grains due to rapid cooling and solidification. Fig. 6B[124] shows the micrographs of Mg–Zn alloys, which clearly demonstrate that the α-Mg phase makes up the majority of the Mg–2Zn alloys since Mg and Zn have different atomic numbers (Fig. 6B(a)). On the other hand, the Mg–6Zn and Mg–8Zn alloys exhibit Zn-rich secondary phases (Fig. 6B(c and d)). This secondary phase (represented as the lighter areas) appeared as tiny, dot-like structures along grain boundaries when the Zn content was less than 4%. The secondary phase in Mg–6Zn alloys was dispersed along grain boundaries, forming a network-like structure at Zn concentrations of 8 weight percent or more. These findings demonstrate that as the Zn content is enhanced, the secondary phase's size and volume fraction also increase. In another study,[62] LPBF was used to fabricate Mg with microstructural characteristics and mechanical properties (Young's modulus and hardness), which were examined for biomedical applications. The hardness (0.59 to 0.95 GPa) and Young's modulus (27 to 33 GPa) of the fabricated sample were in the range of human cortical bones.

**4.1.2 Zn-based BMs.** Normally, LPBF operates in a shielded chamber to maintain the stability of the process by dissipating the vapor products to improve the surface quality further. In addition, recoil evaporation forces splash the molten pool to deteriorate the quality of the surface.[126] Significant irregular and coarse α-Zn grains were obtained from pure Zn (Fig. 7A(a)), whereas a relatively fine crystal structure was obtained upon adding Mg into the Zn matrix (Fig. 7A(b–d)) with eutectics developed at the grain boundaries of α-Zn and Zn–Mg alloy. The highly magnified SEM image (inset of Fig. 7A(d)) depicts the homogenous distribution of eutectics at the grain boundaries. Additionally, Zn–4Mg represents a great quantity of the second phase with irregular polyhedral structures (Fig. 7A(e)). Fig. 7A(f) establishes a relation between the grain size and the Mg content in Zn matrix.[86] The phase diagram of Zn–Mg exhibits the existence of the $Mg_2Zn_{11}$ intermetallic phase because of the peritectic reaction.[127] Li *et al.*[128] reported that Zn–4Mg alloy possesses a polyhedral-shaped grain, which is the $MgZn_2$ phase, and it was further verified by Yang *et al.*[86] Fig. 7B shows the relationship between the laser energy ($E_v$) and the densification rate of the samples. The dynamic behaviour of the molten pool determines the densification rate of the LPBF processed parts, generally. At the same time, if the relative dynamic viscosity ($\mu$) of the liquid within the molten pool becomes high owing to the low $E_v$ to causes more pores.[232] Where $\mu = \frac{15}{16}\sqrt{\frac{m}{kT}}\gamma$; $m$ represents atomic mass, $T$ signifies liquid pool temperature, $k$ is the Boltzmann constant and $\gamma$ signifies the surface tension.

Fig. 7C presents the SEM pictures of the cross sections of the prepared specimens, grain size distribution, and the relation between the laser energy and average grain size. It is evident from Fig. 7C(c) that the average grain size tends to increase with the increase in laser energy.[232] Very fine columnar grains were obtained at low $E_v$, while these grains became coarsened at very high $E_v$. At low $E_v$, the molten pool temperature is low; therefore, the faster cooling of them due to conduction is obtained.[232] Thus, it may be concluded that grain growth is immensely affected by rapid change in solid–liquid interface, thereby resulting in significantly finer grains. Fig. 7D shows the microhardness values measured on high-density Zn parts fabricated by LPBF. The hardness value decreased when compared with the cold-rolled part, but no difference was observed when compared with different energy density level (fluence) conditions.[83,85] Generally, pure Zn shows less processability, thereby resulting in a porous structure.[129] The processability characteristic of Zn–2Al using LPBF resulted in enhanced hardness. LPBF may result in very fine grains (ranging from 2.21–6.62 mm) owing to quick solidification. As per Hall–Petch theory, the hardness is improved by refined grains under the fine-grain strengthening effect.[232] Apart from this, the uniform distribution of the precipitated phase in the matrix is preferred by the LPBF process, which also improves the material's hardness. Energy density ($E_v$) has an important role in the LPBF process. The tensile properties of the LPBF processed material increased with the increase in $E_v$, thereby establishing that the densification rate of the materials is the major parameter influencing the tensile properties of the materials. Moreover, the mechanical properties are also improved by the solution strengthening and second phase strengthening. The hardness and tensile characteristics of the Zn–2Al alloy made with LPBF are displayed in Fig. 7E. The improved mechanical characteristics could be attributed to the grain refinement process that occurred during the alloy treatment.[86,127] It may be worth noting that the tensile properties start degrading after adding 4 wt% of Mg in the Zn matrix because of muddled precipitation of $MgZn_2$, which is brittle in nature. The brittle $MgZn_2$ phase weakens the bonding of the strength of grains. In the LPBF process, powder melting is strongly influenced by the materials' laser energy absorption. Moreover, the densification of processed parts is influenced by input factors, *viz.* hatch spacing, power, and speed of the laser. The LPBF-processed parts possess improved mechanical properties due to densification and grain size compared to the parts processed by common manufacturing techniques such as casting, extrusion, and rolling.[91] Laser melting of pure Zn results in a very fine lamellar-like structure without any preferred orientation (Fig. 7F). This may be due to a higher cooling rate overheating concerning the melting temperature of Zn (*i.e.*, 420 °C).[129]

**4.1.3 Fe-based BMs.** In general, the manufactured parts were developed using LPBF-based AM techniques. The sample in LPBF passes through five major thermal cycles: (i) rapid heating of deposited layers due to absorption of thermal energy; (ii) rapid solidification of deposited layers due to fast heat transfer; (iii) substantial temperature gradients; (iv) accumulated heat; and (v) subsequent quick heating and cooling due to the heating of adjacent layers. Moreover, the rapid re-melting and re-solidifying of layers were found in progression as they were exposed to heat.[130]

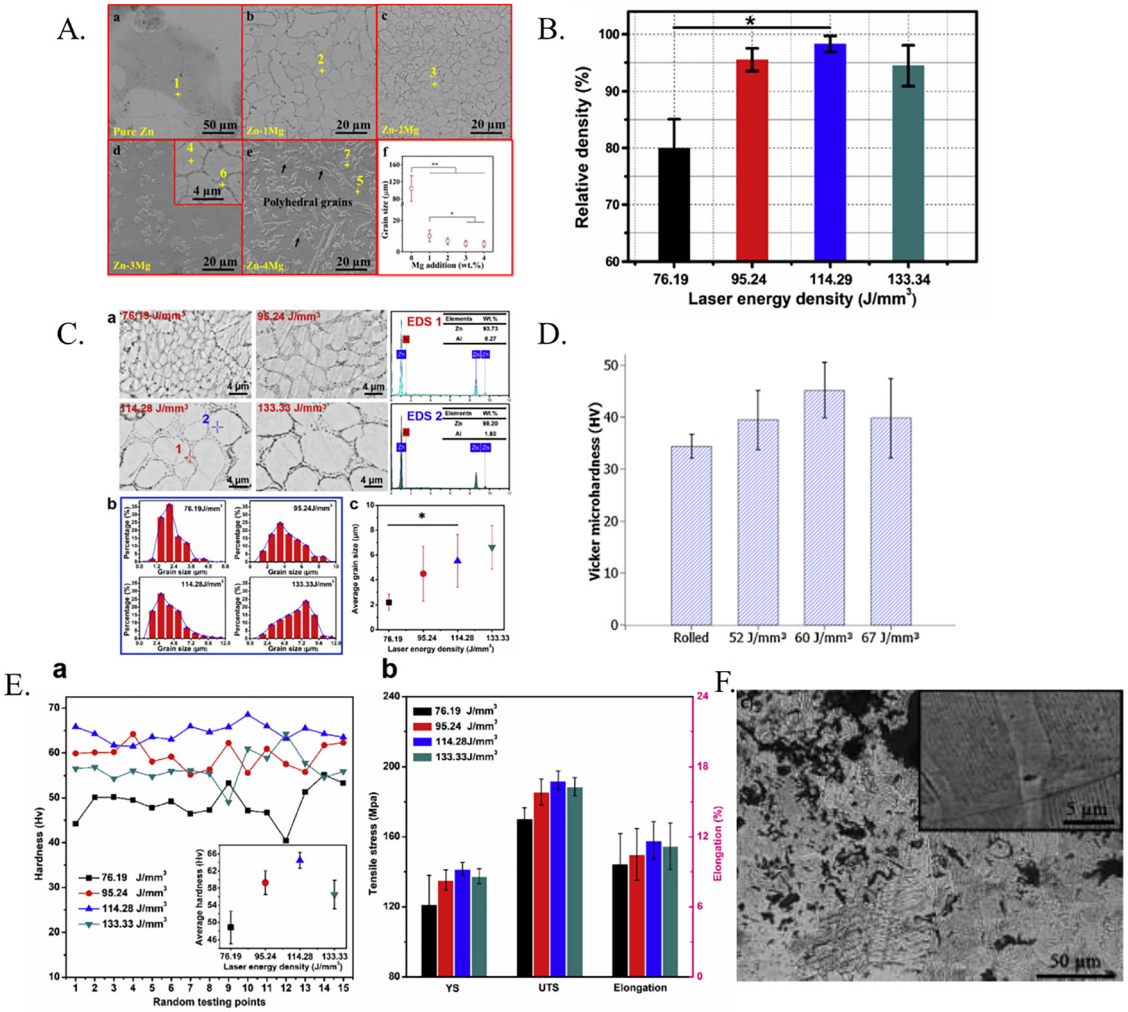


Fig. 7 (A) The scanning electron micrographs display the properties of the crystal structure of LPBF processed (a) pure Zn (b)–(d) Zn–*x*Mg. A high magnification SEM image of the eutectics developed at the grain boundaries is included in the inset of Figure d; The relationship between grain size and magnesium content is depicted in (f). Mean ± SD, $n = 3$, $^{*}p < 0.05$, $^{**}p < 0.01$ were the values (reproduced from ref. 86 with permission from Elsevier, Copyright 2018); (B) the connection between laser energy and the relative densification rate, $n = 3$, $^{*}p < 0.05$ (reproduced from ref. 232 with permission from Elsevier, Copyright 2019); (C) (a) the EDS results of points 1 and 2, indicated by intersecting symbols, and cross-sections of the as-built components acquired at four common $E_v$ from zone III. (b) Grain size distribution (c) and average grain size $n = 50$, $^{*}p < 0.05$ (reproduced from ref. 232 with permission from Elsevier, Copyright 2019); (D) Microhardness of LPBF produced Zn parts with high density (>98%) correlated to cold-rolled counterpart (reproduced from ref. 83 with permission from Elsevier, Copyright 2017); (E) (a) hardness (b) tensile properties of Zn–2Al alloy (reproduced from ref. 232 with permission from Elsevier, Copyright 2019); (F) Microstructure of LPBF processed pure Zn (reproduced from ref. 129 with permission from Emerald, Copyright 2017).

The development of microstructures in AM parts depended on the thermal history as discussed above. The main group of grain morphology that was observed in additively manufactured steel was divided into three major categories: (i) columnar structures, (ii) a combination of columnar and equiaxed structures, and (iii) equiaxed structures. As per the study,[130] the development of microstructure during heating was governed by the ratio of temperature gradient $G_t$ and the velocity of the solidification front $V_s$ *i.e.* $(G_t/V_s)$. The reported study has explained that in case of extremely large value of $(G_t/V_s)$, planar grain microstructure was obtained. The relatively higher value of $(G_t/V_s)$ induced column dendrites, whereas a smaller value results in the equiaxed structure. Generally, in LPBF, the heat is transmitted *via* conduction between the previously deposited layers. Consequently, a directional columnar structure developed due to the formation of temperature gradient in a particular direction.[131]

The melting of the powder layer in the SLM process primarily depends on the energy applied to the material, which is controlled by laser power and scanning speed, respectively. For the chosen range of these two variables, four processing windows could be identified, depending on the quality of the specimens formed during the SLM process.[105]

During solidification, the metal pool contains equiaxed grains in zone I, and columnar grains in zone II, as shown in Fig. 8b.[116] The typical cross-sectional microstructure of

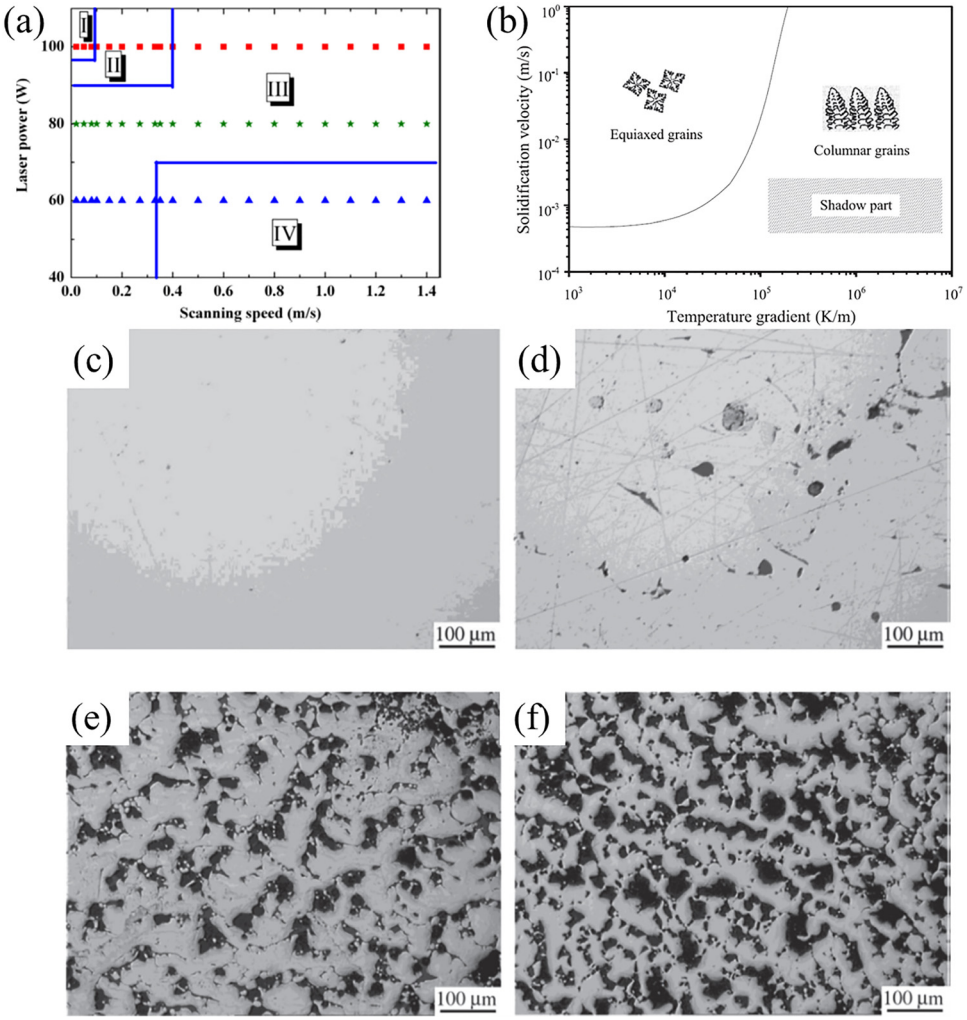


Fig. 8 (a) SLM processing windows of iron powder for laser power *versus* scanning speed (zone I: deformation zone, zone II: formation zone, zone III: poor formation zone, and zone IV: non-forming Zone) (reproduced from ref. 105 with permission from Elsevier, Copyright 2014); (b) a microstructure selection map for SS 316 that displays the various areas of columnar and equiaxed grains in relation to solidification parameters (reproduced from ref. 134 with permission from Elsevier, Copyright 2014); optical micrographs of Fe specimens fabricated at different laser power and scanning speed; (c) 100 W and 0.33 m $s^{-1}$; (d); 100 W and 0.5 m $s^{-1}$; (e) 80 W and 0.33 m $s^{-1}$; (f) 60 W and 0.33 m $s^{-1}$ (reproduced from ref. 105 with permission from Elsevier, Copyright 2014).

SLM-fabricated Fe samples made with varying processing parameters is depicted in Fig. 8(c–f); these samples primarily correspond to zones II and III. A completely dense microstructure was seen at 100 W and 0.33 m $s^{-1}$. Zone III showed a microstructure with a few pores when 100 W and 0.5 m $s^{-1}$ were used. A structure with several discontinuous layers developed at a laser scanning speed of 0.33 m $s^{-1}$ when the laser intensity was lowered to 80 W. It is evident that the partly melted powders were joined when the laser power was further reduced to 60 W. The sintering between the layers was also apparent at the same scanning speed of 0.33 m $s^{-1}$.[105] In LPBF technique, the growth of microstructures was complex because of the uninterrupted re-melting of metal powders during deposition and due to the Marangoni effect. In brief, the Marangoni effect is a kind of mass transfer between two phases due to differences in surface tension. Thereby, different grain growth structures were formed along different orientations. As per the study, the high-temperature gradient (such as around 106 K $m^{-1}$) in the case of LPBF caused columnar structure in most of the material structures.[132] These columnar structures exhibited excellent plasticity with weak mechanical strength. The main cause of the high-temperature gradient in LPBF was associated with a difference in thermal conductivity formed between powders and deposited solidified melted zone. Therefore, heat dissipation in the build direction was larger than in other directions, leading to anisotropy in grain morphology and mechanical characteristics in a specific direction. Moreover, the cooling rates were higher LPBF process because heat concentration areas during laser depositions were relatively small. Hence, small heat-affected zones and finer-grain structures were reported. It was observed from the study that Fe-based alloy (316L SS) that processed with LPBF exhibited higher yield strength as compared to forged materials.[133]

The mechanical characteristics of Fe-based alloys prepared using powder-based AM were more affected by the heating rate, laser power, and layer thickness. The inhomogeneity in the grain structure formed due to the rapid cooling rate in the top and bottom zones resulted in high micro-hardness as compared to the central zone. The reason was attributed to the highest micro-hardness in specific H13 Tool steel because of reheating during the process. The same behaviour was observed with 316 SS, wherein the clad surface accelerated its hardness properties. The ultimate and yield strength of Fe-based alloys prepared using LPBF parts were found to be greater than those developed using forging. These higher mechanical properties were obtained because of higher cooling rates and grain refinements. Although the parts processed using LPBF exhibited a lesser elongation to failure standards due to the high content of porosity and available additions within the products. Moreover, another major feature of the AM process in the context of tensile properties was the building orientation of the parts. In the summary of building orientation effects, it was observed that the deposition of materials in the *Z* and *Y* directions shows anisotropic behavior because of weak interfacial layer bonding.

Fig. 9 shows the compressive stress strain curves of additively manufactured Fe foam architectures.[101] The densification zone, the plateau region, and the linear elastic region comprised the bulk of the computed stress–strain curves. First, an elastic response was seen, where the applied strain caused the stress to increase linearly. It was found that the stress in the second region varied between the mean values because the cell structures in the OPTS sample failed. The third area is the general increase in stress caused by the densification of the cell structures. Upon examining the stress–strain curves, it became evident that the plateau regions that were generated were not smooth. There is a notable variation in stress because the unit cell structures in the produced OPTS samples fracture brittlely. Micropores and interstices are present in the struts of the manufactured TOPIF samples. Due to the concentration of stress caused by compressive force, these micropores served as the nuclei for the creation of cracks. The variance in compressive stress was caused by the rapid propagation of cracks as the compression load increased, which led to the breakdown of unit cell structures. It was assumed that the aforementioned component caused the decrease in compressive strength, even though the effect of these micropores on compression strength was not evaluated. The broken unit cell structures were forced together during additional compression, which raised the compressive stress once more. Until the subsequent unit cell structural rupture, this rise in compressive stress persisted.

**4.1.4 Comparative mechanical properties of Mg-, Zn-, and Fe-based alloys.** Mechanical properties play a crucial role in determining the suitability of biodegradable metallic implants, particularly for load-bearing orthopedic applications and cardiovascular stents. Magnesium (Mg), zinc (Zn), and iron

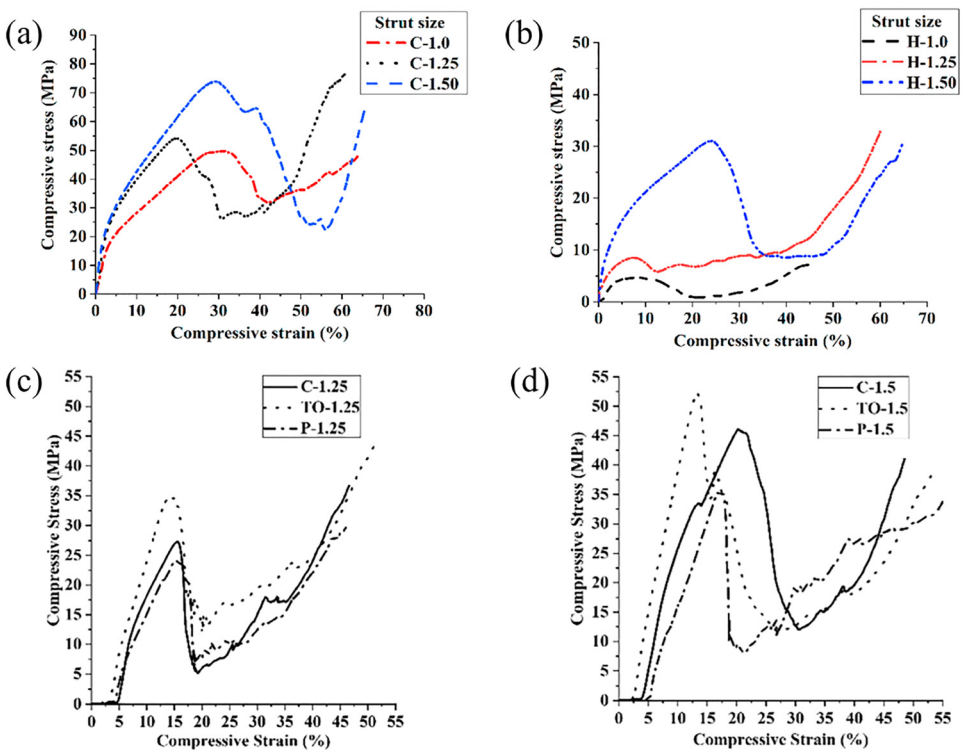


Fig. 9 Compressive stress–strain plot of additively fabricated (a) C-OPTS (b) H-OPTS (reproduced from ref. 102 with permission from Elsevier, Copyright 2021); (c) and (d) C-TOPIF, TO-TOPIF, and P-TOPIF of strut size 1.25 mm and 1.5 mm (reproduced from ref. 101 with permission from Elsevier, Copyright 2018). (C – cubic; H – hexahedron; TO – truncated Octahedron; P – pyramid; OPTS – ordered pore topological structures; TOPIF – topologically ordered open cell porous iron foam).

(Fe)-based alloys exhibit significantly different mechanical characteristics due to variations in crystal structure, alloy composition, and processing conditions. Mg-based alloys typically exhibit elastic modulus values in the range of 20–45 GPa, which are close to that of natural bone (3–20 GPa), thereby minimizing stress shielding effects. The ultimate tensile strength of Mg alloys generally ranges from 100 to 300 MPa, depending on alloying and processing routes such as additive manufacturing. These properties make Mg alloys particularly suitable for orthopedic implants requiring temporary mechanical support.[1,75,122,233] Zn-based alloys possess relatively lower mechanical properties compared to Mg and Fe systems. The elastic modulus of Zn alloys typically ranges from 70 to 110 GPa, while the tensile strength varies between 100 and 300 MPa depending on alloying and microstructural refinement. Studies have demonstrated that alloying Zn with Mg or Ag can significantly enhance its strength and ductility, making it suitable for biodegradable stent applications.[135] Fe-based alloys exhibit significantly higher mechanical strength, with elastic modulus values of approximately 180–210 GPa and tensile strength exceeding 300–600 MPa. These values are considerably higher than those of cortical bone, which may lead to stress shielding. However, their superior strength and ductility make them suitable for load-bearing applications where long-term mechanical stability is required.[136,137]

A comparative assessment indicates that Mg alloys provide mechanical compatibility with bone, Zn alloys offer moderate strength suitable for vascular applications, and Fe alloys provide high strength but may require structural or compositional modifications to reduce stiffness mismatch. Therefore, mechanical property tailoring through alloy design and additive manufacturing is essential to optimize performance for specific biomedical applications. As illustrated in Fig. 10(a–c), Mg-based alloys exhibit significantly lower elastic modulus values, Zn-based alloys demonstrate intermediate mechanical properties, while Fe-based alloys show markedly higher stiffness and strength among biodegradable metals. A comparative illustration of mechanical properties of biodegradable metals has been reported in previous studies, highlighting the lower elastic modulus of Mg, intermediate properties of Zn, and significantly higher stiffness and strength of Fe-based alloys (Table 1).[138–140]

### 4.2 Corrosion mechanism of BMs

Surface modification and protective coatings have been widely explored to improve corrosion resistance in metallic systems. Studies on coated steels and rebars demonstrate that epoxy, polyurethane, and alloy-based coatings significantly enhance corrosion resistance by forming protective barrier layers and reducing ion diffusion in aggressive environments.[143–146] For instance, colour-coated steels with polyurethane layers exhibit superior corrosion resistance compared to galvanised and galvalume steels due to their strong adherent barrier properties that inhibit corrosive species penetration.[147]. Such surface engineering strategies provide useful insights for controlling degradation behaviour of biodegradable metallic implants. While degradable metals are a promising research field to help meet the medical need for improved orthopedic, cardiovascular, and pediatric implants, the currently available *in vitro* and *in vivo* evidence appears to yield mixed results regarding their effectiveness. This is mainly due to the shortage of knowledge on the rate and biocompatibility of metal corrosion in varied conditions. It is difficult to degrade biodegradable metallic implants *in vivo*.[148] One way degradation might occur is through corrosion, in which electrolytes enter bodily fluids and react with hydroxides, oxides, hydrogen gas, and other substances to produce metal ions. Small amounts of corrosion materials can be safely absorbed by the human body, but prolonged exposure to large concentrations of certain ions, particles, and gases can have detrimental local and systemic effects.

**4.2.1 Mg-based BMs.** The degradation behavior is the primary factor that describes the life span of the biodegradable implant. It is a well-known fact that the restoration of fractured bone usually requires 3–12 months. This necessitates to retard the degradation rate (~0.5 mm per year) of the Mg-based biodegradable implants.[86] Prior studies showed that the secondary phases in the Mg alloy cause potential differences and could be categorized as the anode (Mg matrix) and cathode (secondary phases due to alloying elements) phases of microgalvanic corrosion.[149] Subsequently, the formation of galvanic pairs leads to galvanic current generation, thereby initiating pitting corrosion.[150] It is commonly assumed that $Mg(OH)_2$ films could not protect the surface for an extended period under the influence of chloride ions. Apart from the secondary

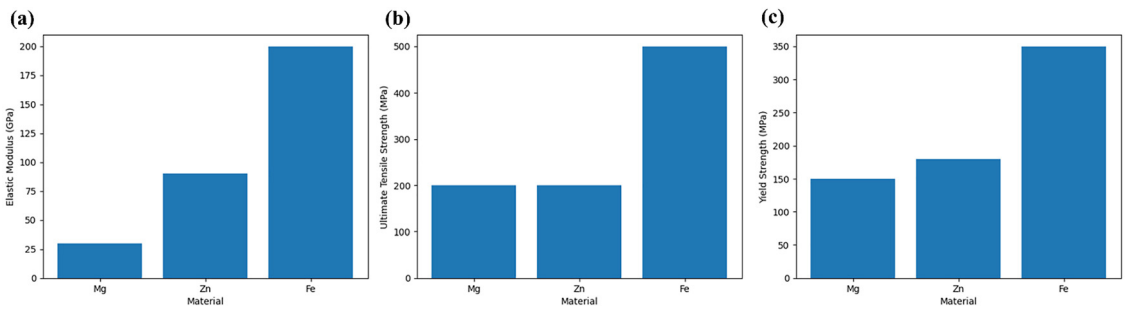


Fig. 10 Comparative mechanical properties of biodegradable Mg-, Zn-, and Fe-based alloys: (a) elastic modulus, (b) ultimate tensile strength, and (c) yield strength.

Table 1 Comparative mechanical properties of biodegradable metals

| Material | Elastic modulus (GPa) | Yield strength (MPa) | UTS (MPa) | Elongation (%) | Application | Ref. |
|---|---|---|---|---|---|---|
| Mg-based alloys | 20–45 | 65–200 | 100–300 | 5–20 | Orthopedic implants | 1, 75, 122 and 233 |
| Zn-based alloys | 70–110 | 100–250 | 100–300 | 1–10 | Cardiovascular stents | 135, 141 and 142 |
| Fe-based alloys | 180–210 | 200–500 | 300–600 | 10–40 | Load-bearing implants | 137 |

phases, the compositions and grain size also affect the degradation behavior of developed materials.[123,151] Several researchers have recently stated that the alloying operation of Mg alloys with rare-earth (RE) elements is an encouraging way to enhance the anti-corrosion behavior of pure Mg. The protection against the corrosion of Mg alloys usually depends on their passivating layers. Generally, the passivating layers formed on the surface of Mg consist of an outer $Mg(OH)_2$ layer and a thin inner MgO layer.[152] As a result, the inner oxide layer is meant to function as a useful film. Nonetheless, the Pilling Bedworth ratio (RP-B), which measures the molar volume of the unit cell of MgO compared to the amount of Mg, is 0.81.[153] The volume mismatches between the underlying Mg metal and the MgO result in a poor compact inner MgO layer. Fig. 11A represents the variation in the hydrogen evolution volume and pH values of ZK60-*x*Nd immersed in SBF. It could be evident from Fig. 11A(a) that the addition of Nd to a specific limit (up to 3.6 wt%) decreased the variation in both hydrogen evolution volume and pH values which indicates the reduction in the corrosion rate accordingly. This was mainly attributed to the RP-B (more than 1) of Nd. Therefore, the generation of $Nd_2O_3$ as a surface film on the ZK60-Nd boosted the compactness of the surface oxide film and thereby improved the ability to oppose the penetration of interacting fluids.

Grain refinement potentially raises the corrosion rate by increasing the number of grain boundaries. In PBF samples, the high cooling rate creates very small grains, and increased surface reactivity to corrosion is predicted as a result, but only in metals whose corrosion rate is not massive. The formation of corrosion products due to the use of fine grains in a passive

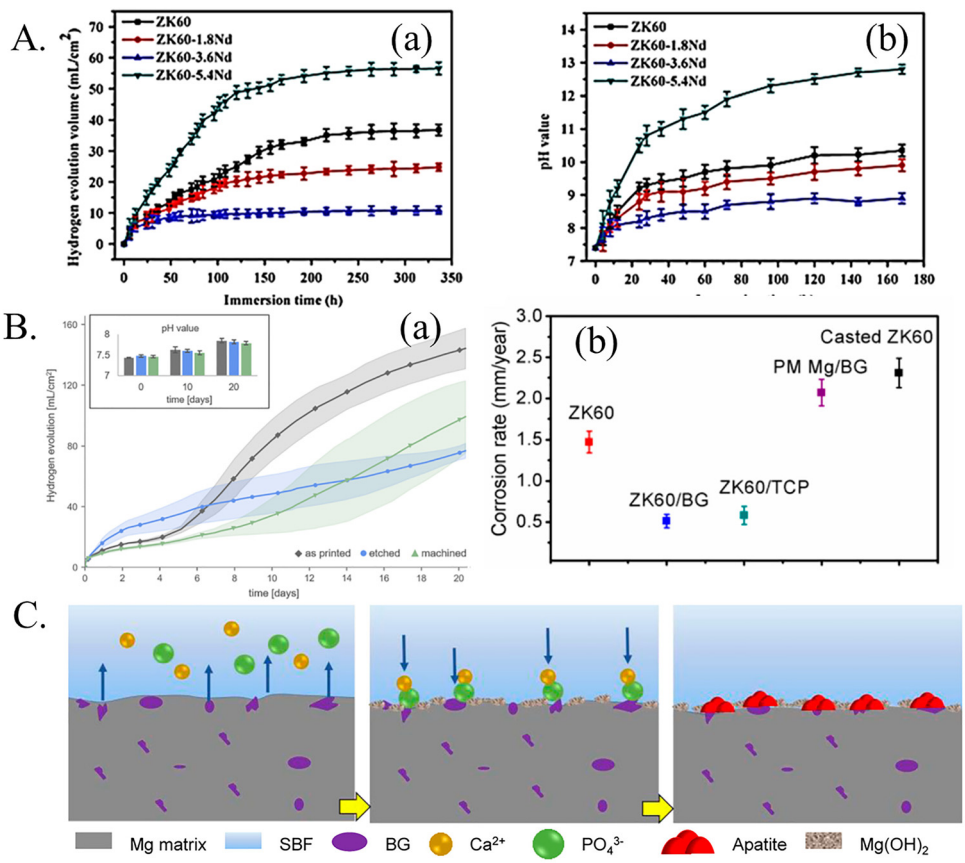


Fig. 11 (A) (a) Hydrogen evolution volume and (b) variation in pH values of ZK60-*x*Nd immersed in SBF (reproduced from ref. 71 with permission from Springer Nature, Copyright 2017); (B) (a) data on the hydrogen evolution of the three surface states in c-SBF during a 20-day period, including pH readings at various intervals (top left box) (reproduced from ref. 154 with permission from Elsevier, Copyright 2021) (b) computed corrosion rates of Mg-based composites (reproduced from ref. 155 with permission from Taylor and Francis, Copyright 2020); (C) the illustration demonstrated how apatite was deposited on ZK60/BG during immersion (reproduced from ref. 155 with permission from Taylor and Francis, Copyright 2020).

environment may lower the corrosion rate, which can be observed in Mg. Uniform corrosion products are formed due to the use of small grain size, which makes forming a dense layer of MgO and $Mg(OH)_2$ easier, reducing corrosion rate. So, grain size affects the corrosion rate, which can be seen in pure Fe as similar to Mg.[75] Rapid melting and solidification inherent to AM processes such as LPBF produce ultra-fine grains, supersaturated solid solutions, and a high density of secondary phases (*e.g.*, Mg–Zn, Mg–rare earth). These microstructural features, combined with process-induced defects such as porosity, lack-of-fusion voids, and melt pool boundaries, strongly influence degradation. In particular, the presence of secondary phases establishes micro-galvanic couples, where the Mg matrix acts as the anode and corrodes preferentially, leading to accelerated localized corrosion and pitting. Furthermore, porosity and surface roughness increase the effective surface area and act as preferential sites for corrosion initiation, thereby significantly increasing the corrosion rate. Although grain refinement can promote a more uniform corrosion front due to increased grain boundary density, the overall corrosion behaviour of AM Mg alloys is typically dominated by rapid degradation and hydrogen evolution. However, in certain compositions (*e.g.*, Mg–Al systems), supersaturation can enhance the formation of protective oxide films, slightly improving corrosion resistance.[156–159]

The specific surface area is another important factor that affects the corrosion rate. A higher corrosion rate is observed in the case of porous AM BMs due to a larger contact surface with the corrosive medium than in bulk samples. This property is mainly used in the case of Fe and Zn than in Mg due to the low degradable nature of the metal. There are no specific standards for measuring the *in vitro* corrosion rate of Mg. So, weight loss, hydrogen evolution measurement, electrochemical approaches, and micro-CT are among the methods developed by researcher.

Phosphoric etching and machining were used in succession to modify the surfaces of cylindrical Mg specimens that were made using LPBF.[154] After examining degradation behaviour and biocompatibility, it was shown that etched samples had the lowest overall degradation rates but also developed big pits, whilst reducing surface roughness caused degradation to occur more slowly. After 20 days of degradation, measurements of the pH value at certain time points during the experiment (upper left in Fig. 11B(a)) showed a slight increase in pH, starting at $7.4 \pm 0.15$ at the start and rising to $7.8 \pm 0.21$ at the end. Nonetheless, there was no discernible difference in the pH values over the series. The as-printed series displayed a noticeably higher value than the etched and machined series, which might be connected to the faster rate of degradation during the first three days (Fig. 11B(a)). Fig. 11B(b) also includes a comparison of the ZK60/BG after LPBF processing with various magnesium-based composites. Comparing LPBF-processed ZK60/BG to ZK60/TCP and powder metallurgy (PM)-processed Mg/BG, the former demonstrated a lower rate of degradation. It goes without saying that the composition had a big impact on how Mg-based products degraded. Si-containing BG might efficiently encourage the deposition of the mineralized layer in comparison to other bioactive ceramics. The schematic representation of the apatite deposition on ZK60/bioglass (BG) during immersion may be found in Fig. 11C. ZK60/BG first deteriorated *via* electrochemical corrosion in the same way as other magnesium alloys. $Ca^{2+}$ and $PO_4^{3-}$ should be released because of the significant amount of BG particles that were exposed to the surface. Importantly, the hydrolysis reaction of $SiO_2$, the primary constituent of BG, could result in the formation of a negatively charged silica gel layer. Thus, electrostatic adsorption would cause the $Ca^{2+}$ and $PO_4^{3-}$ to be absorbed on BG in succession. These absorbed $Ca^{2+}$ and $PO_4^{3-}$ groups then crystallized into apatite, which resembles bone. The deposited apatite had a stable and compact structure in contrast to $Mg(OH)_2$, which significantly delayed the breakdown of the Mg matrix. Nevertheless, the surface bioactivity of the magnesium alloys as bone implants was improved by the generated bone-like apatite, which was expected to produce an encouraging bone/implant interface to produce new bone when implanted *in vivo*.

**4.2.2 Zn-based BMs.** Zinc and zinc-based alloys provide an attractive mix of biocompatibility and biodegradation behavior in the field of biomedical implant applications. The regulated degradation kinetics of these materials guarantee a slow breakdown within the body in agreement with tissue regeneration and recovery.[160] Since zinc ions produced during degradation are essential for physiological functions, such as cell division and differentiation, the corrosion products of zinc and its alloys are usually non-toxic and even advantageous.[161,162]

The durability of the biodegradable implant immensely depends on the degradation rate. It is a fact that the repairing process of hard tissues generally takes 3 months to 12 months to accomplish. This instigates the requirement that a slower degradation rate ($\sim$0.5 mmpy) is required for biodegradable implants.[86] According to the current plateaus in anodic polarization, Zn–Mg alloys exhibited a passivation behaviour, as seen in Fig. 12A(a). The corrosion rate rose because of the higher magnesium content. Fig. 12A(b) illustrates how the pH level in Hank's solution changed throughout the immersion test. All of the samples showed fluctuation over the first ten days of immersion. A comparatively stable state was then attained. The pH values of Zn–5Mg were somewhat higher than those of Zn–1Mg and Zn–2Mg samples. The weight decrease following 28 days of immersion is seen in Fig. 12A(c). The corrosion rate marginally increased as the magnesium content rose, which is consistent with the electrochemical data. The samples with Zn–5Mg showed the highest rate of corrosion.[92] The Zn–Mg–Ag alloys made *via* SLM were tested for corrosion behaviour using electrochemical tests in an SBF solution. Fig. 12B(a) shows representative potentiodynamic polarization curves. Tafel fitting of the polarization curves was used to determine the electrochemical parameters, and the results showed a modest positive swing in the corrosion potential with increasing Ag concentration. The solid solution of noble Ag may be the reason for the higher positive potentials and lower current densities, which show that Ag doping improves the produced alloys' electrochemical resistance. Fig. 12B(b) displays the pH change with immersion time, and the alloy extracts under

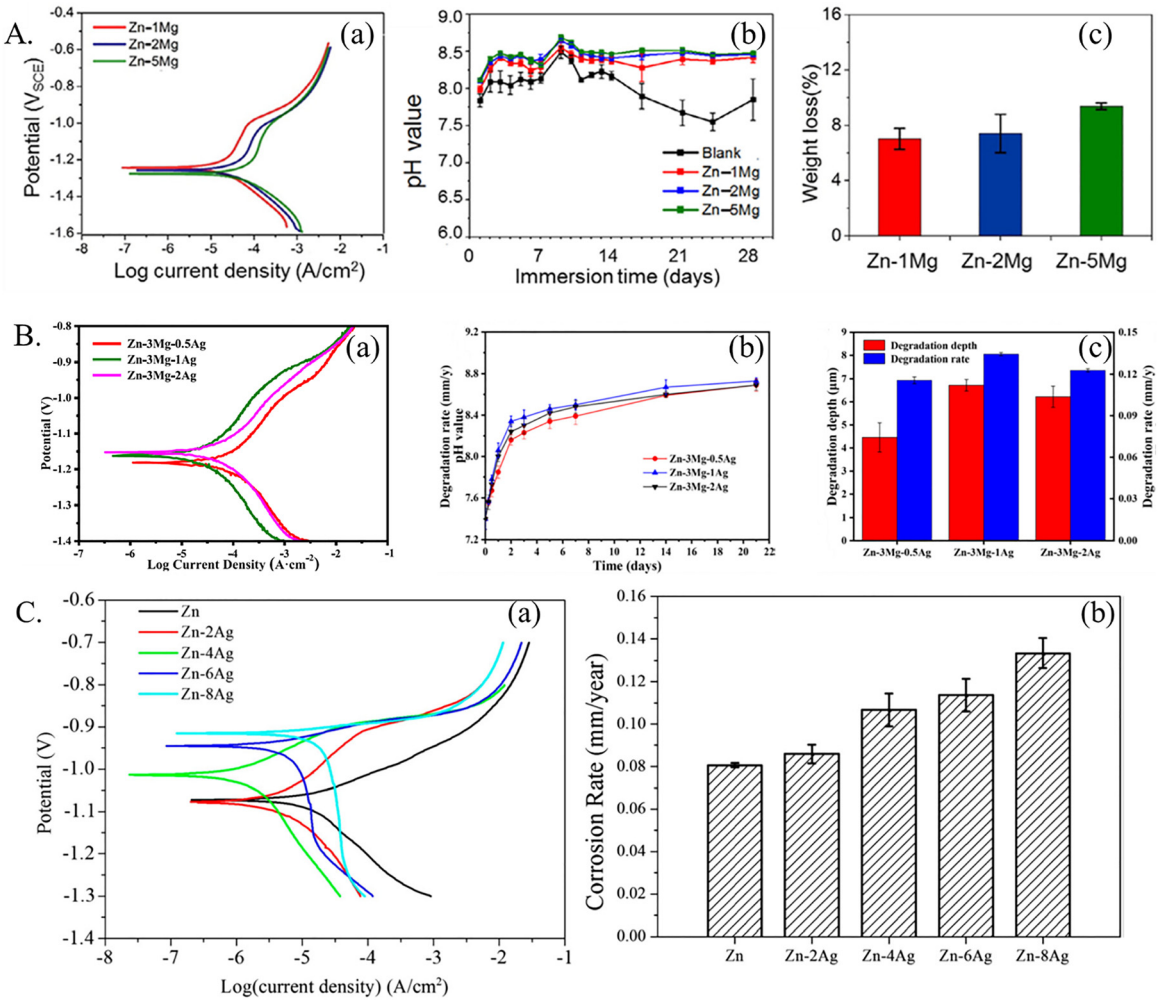


Fig. 12 (A) *In vitro* corrosion behaviour of Zn–*x*Mg alloys: (a) PP curves (b) pH variation (c) weight loss during immersion test (reproduced from ref. 92 with permission from Elsevier, Copyright 2022); (B) (a) PP curves for Zn–3Mg–*x*Ag alloys (b) pH variation with respect to immersion time (c) Weight loss-based calculations for degradation depth and rates (reproduced from ref. 89 under Creative Common License from Elsevier, Copyright 2022); (C) (a) PP curves (b) corrosion rate during 21 days of immersion of Zn–*x*Ag alloys in SBF at 37 °C (reproduced from ref. 163 with permission from Taylor & Francis, Copyright 2018).

investigation exhibit a similar pattern in the SBF. During the first five days of immersion, the pH rises noticeably before stabilizing. As the Ag content rises, Fig. 12B(c) and C(a) show that the degradation products' thickness first increases and then gradually decreases[89,163] and weight loss indicates a similar trend in the rate of decline. The Zn–3Mg–0.5Ag alloy experiences an increase in deterioration rate, followed by a modest drop in the Zn–3Mg–1Ag alloy. The amount and spacing of spiral eutectic may be the cause of this, since it not only caused microgalvanic corrosion but also influenced the quantity and resistance of microgalvanic couples, leading to varying rates of degradation following extended immersion.[89] Fig. 12C(b) displays the pace at which Zn–*x*Ag alloys corrode. The corrosion rate increased following alloying with Ag. The findings demonstrated that Zn–*x*Ag alloys corroded more quickly than Zn because of enhanced galvanic corrosion.[89]

Zinc (Zn)-based biodegradable materials produced *via* AM present an intermediate case, where the microstructure enables a more balanced corrosion response. Due to the relatively low melting and boiling points of Zn, AM processing often results in coarse grains, pronounced crystallographic texture, and moderate levels of porosity. Unlike Mg, Zn does not exhibit highly aggressive galvanic corrosion, although intermetallic phases (*e.g.*, Zn–Mg, Zn–Al) can introduce mild electrochemical heterogeneity. Grain boundaries in Zn tend to facilitate more uniform corrosion, while the absence of a strongly protective passive film allows for steady and controlled degradation. However, the presence of texture can lead to anisotropic corrosion behaviour, with certain crystallographic orientations degrading preferentially. Additionally, process-induced porosity and surface irregularities can slightly accelerate corrosion but do not typically result in severe localized attack as observed in Mg systems. Overall, the AM microstructure of Zn supports a moderate and relatively uniform corrosion rate, which is considered close to ideal for biodegradable implant applications.[38,164,165]

**4.2.3 Fe-based BMs.** Based on vitro experimentation, the application of Fe as a biodegradable implant was first proposed by Puster *et al.*[166] Pure Fe stents were implanted in porcine coronary arteries, and no evidence of inflammation and thrombosis was found. Overall, pure Fe was reported to be safe for degradable implant applications. Previous studies have reported that by incorporating surface modification and alloying, the degradation behavior of Fe can be improved significantly as compared to pure solid Fe. Moreover, developments of Fe-based alloys have been shown to benefit advantages to increase the degradation rate of Fe. From the reported studies,[11,167,168] it was observed that the incorporation of Mn in pure Fe has significantly influenced the increase in its degradation rate. The results have shown that the Fe35Mn-based alloys induced an anti-ferromagnetic austenitic structure that assists in accelerating the corrosion/degradation rate and is better suited for orthopedic applications. Further, more studies[169–171] have been reported wherein the authors have introduced a righteous element Pd that induced a more noble effect after combining with the FeMn matrix. The addition of the Pd phase in the matrix of FeMn matrix triggered noble micro-galvanic corrosion. In addition, the microsites available in the samples were charged with higher negative potential than base metals. As a result, increasing the dissolution of the anodic electrode increases with a less noble phase. Investigating how Fe-based alloys degrade, electrochemical testing, including potentiodynamic polarization and static immersion tests, were conducted. The potentiodynamic polarization test was performed to assess the immediate degradation of samples after monitoring the corrosion current. On the other side, a static immersion test was done by monitoring the weight-loss measurement of samples over a certain period.[65,169,170]

From the reported study,[172] it was depicted that the addition of alloying elements such as Pd, Pt, W, C, S, Si, and Ga in the Fe matrix has increased its degradation rate. When alloying elements like Ca and Mg are added to FeMnSi alloys, fine precipitates are formed, which helps to speed up the corrosion rate. Additionally, it was shown that metals having significant potential differences accelerated the degradation rate of Fe. The released ions of Au and Ag behave like an active cathode, intensifying microgalvanic corrosion. However, Ag is a kind of antiseptic material that has anti-toxicity properties that could be used as a suitable material for inflammatory bone disease. Hence, the addition of Ag in Fe could be beneficial in terms of increasing its degradation rate and hampering the spread of bacterial disease.[173]

Sotoudehbagha *et al.*[65] have presented the degradation study of the Fe–Mn-alloy matrix with the different contributions of Ag. The degradation study was performed using electrochemical testing in HBBS solution at 25 °C wherein they evaluated the potentiodynamic polarization. The potentiodynamic polarization was presented using Tafel's plot ($E_{corr}$ *vs.* $I_{corr}$) and the degradation rate was calculated as per the ASTM G59 standard:

$$CR = 3.7 \times 10^3 \frac{i_{corr} \times EW}{\rho(\text{density})}$$

The corrosion rate (CR) of the Fe alloy matrix was calculated by considering the oxidation of Fe to $Fe^{2+}$ and its equivalent weight (ER = 27.92 g eq.$^{-1}$). As per the study presented by Sotoudehbagha *et al.*,[65] it was observed that the addition of Ag in the Fe alloy matrix induced a significant increase in mechanical properties such as microhardness, density, and ultimate shear strength (USS). The authors also noticed that the increase in Ag wt% (in the range of 1–3%) in the Fe matrix showed a more uniform contribution within the austenite phase. Similarly, another study was performed wherein Fe–Au and Fe–Ag alloy was produced by Huang *et al.*[100] for the stent application in biomedical fields that can potentially replace the nitinol based cardiac stents.[174,175] The PM route technique was used by the authors with spark plasma sintering to produce these alloys. To mimic the body environment, the degradation study of Fe and its alloy matrix was performed Hank's salt solutions. The presence of foreign elements such as Au and Ag in the Fe alloy matrix yielded a much finer gain structure as compared to pure cast Fe attributed to improved mechanical properties. Further, this study was confirmed by XRD wherein two different phases such as alpha-Fe and Au phases, and alpha-Fe and Ag phases in Fe–Au, and Fe–Ag alloy matrix, respectively. Additionally, it was also shown that the improvement of mechanical properties with the inclusion of Ag and Au, mainly with the composition of Fe–5wt% Ag, has shown excellent mechanical properties. Fig. 13(a) and (c) make it clear that the corrosion potential in porous samples increased as the strut size increased. Furthermore, the corrosion potential of the C-TOPIS sample with alike strut size was higher than that of the TO-TOPIS sample with a 1.50 mm strut size. As the strut size increased, so did the corrosion current density of the prepared TO-TOPIS specimens. Additionally, it was discovered that the corrosion properties were strongly impacted by the unit cell structure. The corrosion current density was lower for the C-TOPIS sample with a 1.5 mm strut size than for the TO-TOPIS sample with a comparable strut size. The difference between the porosities may be one of the causes of the variance in corrosion current density of the samples.[176] The addition of Ca or Mg caused the current density of the Fe–Mn alloys to move to the positive side. A higher corrosion rate is inferred by an increase in corrosion current density caused by the substitution and incorporation of Mg and Ca since the corrosion rate and corrosion current density are linearly related. However, it's interesting to note that the corrosion potential of the Fe–Mn–Mg alloy was significantly higher than that of the binary Fe–Mn alloy, suggesting that it was likely more electrochemically stable (Fig. 13(b)).[177] Fe30Mn was found to have greater active corrosion potential values than Fe, which ultimately led to its higher DR (Fig. 13(d)).[97] Fig. 13(e) and (f) demonstrate the weight loss of C-TOPIS and H-OPTIF samples, respectively. It was clear that the TOPIS sample with the most weight loss had a truncated octahedron unit cell shape and a 1.5 mm strut size and OPTIF sample with a hexahedron shape of 2 mm strut size had a highest weight loss.[176,178]

Overall, in comparison to Mg and Zn, Fe based biodegradable materials processed *via* AM exhibit fundamentally different corrosion characteristics due to their intrinsically lower reactivity and strong passivation tendency. The AM process typically produces

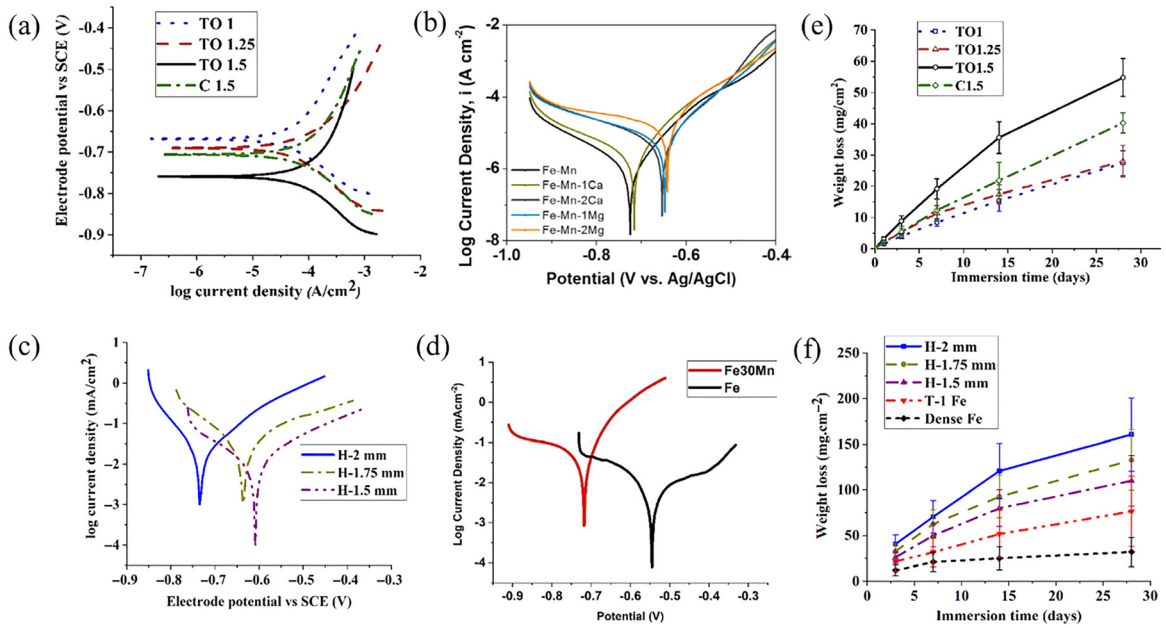


Fig. 13 Potentiodynamic polarization curves for (a) TOPIF samples prepared by rapid tooling (reproduced from ref. 176 with permission from Elsevier, Copyright 2020); (b) Fe alloys fabricated using binder jetting (reproduced from ref. 177 with permission from Elsevier, Copyright 2016); (c) OPTS samples fabricated using micro-extrusion technique (reproduced from ref. 178 with permission from Elsevier, Copyright 2022); (d) Fe alloys fabricated using hybrid 3D printing (reproduced from ref. 97 with permission from Elsevier, Copyright 2025); (e) and (f) Weight reduction of porous Fe samples during immersion testing (reproduced from ref. 176 and 206 with permission from Elsevier, Copyright 2020 and 2022).

relatively dense microstructures with refined grains and limited porosity when optimized processing parameters are used. A key factor governing corrosion in Fe is the formation of a stable and adherent oxide layer, which acts as a barrier to further degradation. Grain refinement in AM Fe slightly increases the number of sites for corrosion initiation; however, this effect is minor compared to the dominant influence of passivation. Additionally, microstructural heterogeneities such as retained austenite, oxide inclusions, and melt pool boundaries can introduce localized electrochemical variations, leading to mild micro-galvanic effects. Nevertheless, these are insufficient to significantly accelerate degradation, and the overall corrosion behaviour remains slow and relatively uniform. Consequently, AM Fe suffers from excessively low degradation rates, which limits its effectiveness for applications requiring timely resorption.[179–181]

**4.2.4 Comparative biodegradation behaviour of Mg-, Zn-, and Fe-based alloys.** Biodegradation behaviour is a critical parameter governing the clinical performance of biodegradable metallic implants, as it determines the duration of mechanical support and the interaction of degradation products with surrounding biological tissues. Magnesium (Mg), zinc (Zn), and iron (Fe)-based alloys exhibit significantly different degradation characteristics, which directly influence their suitability for specific biomedical applications. Mg-based alloys are characterized by relatively high degradation rates (~1–5 mm per year), primarily driven by electrochemical corrosion in physiological environments and accompanied by hydrogen gas evolution. This rapid degradation can result in premature loss of mechanical integrity and localized alkalization, limiting long-term applications.[182,183] Zn-based alloys exhibit intermediate degradation rates (~0.1–0.5 mm per year), which are considered suitable for biomedical applications such as vascular stents. Unlike Mg, Zn degradation does not produce hydrogen gas, and its corrosion products are generally well tolerated. Previous studies, including those by Hamid Reza Bakhsheshi-Rad, have reported that Zn alloys degrade more slowly than Mg while maintaining good biocompatibility.[135] In contrast, Fe-based alloys demonstrate very low degradation rates (~0.01–0.1 mm per year) due to the formation of stable passive oxide layers, which significantly retard corrosion. This slow degradation limits their effectiveness as fully biodegradable implants and may lead to long-term residue accumulation.[140,182] A schematic comparison of degradation behaviour among Mg-, Zn-, and Fe-based biodegradable metals has been reported in previous studies, illustrating the significantly higher degradation rate of Mg, intermediate behaviour of Zn, and slow degradation of Fe[182] and a similar comparison is added in Table 2. A comparative analysis indicates that Mg alloys are suitable for applications requiring rapid resorption (*e.g.*, temporary orthopedic fixation), Zn alloys provide a balanced degradation profile aligned with tissue healing rates, and Fe alloys are more appropriate for applications requiring extended mechanical support. Therefore, the selection of biodegradable metals must be tailored based on the required degradation kinetics and clinical application.

### 4.3 Biological behaviour of BMs

Fig. 14 shows the various factors that may adversely affect the biocompatibility of the implanted parts. There are many kinds of metallic trace metals in the body, including chromium (Cr), cobalt (Co), copper (Cu), Fe (Fe), manganese (Mn),

Table 2 Comparison of biodegradation behaviour of Fe, Mg, and Zn based biodegradable alloys

| Material | Degradation rate (mm year$^{-1}$) | Corrosion mechanism | Key limitation | Application | Ref. |
|---|---|---|---|---|---|
| Mg-based alloys | 1–5 | Electrochemical corrosion + $H_2$ evolution | Rapid degradation, gas formation | Orthopedic implants | 182,183 |
| Zn-based alloys | 0.1–0.5 | Uniform corrosion, no gas evolution | Lower mechanical strength | Cardiovascular stents | 135,182 |
| Fe-based alloys | 0.01–0.1 | Passive oxide layer formation | Very slow degradation | Load-bearing implants | 140,182 |

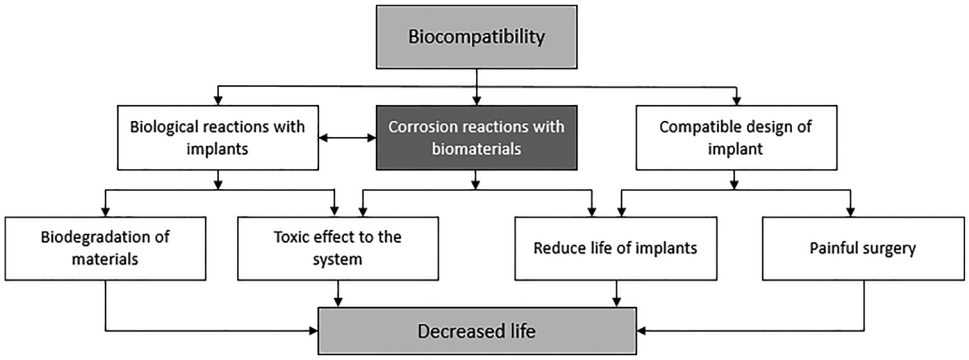


Fig. 14 Factors and their effects on biocompatibility.

molybdenum (Mo), nickel (Ni), and Zn. However, Mg and Ca can be identified in the human body as major metallic elements. Bioresorbable metals have primarily concentrated on Mg or Fe-based metals, and their different alloys, although some important research has also been reported recently on the use of Zn alloys for absorbable applications.[70,184] No noticeable research on these basic elements shows the cytotoxic behaviour of the body, which augments their viability as potential BMs. Nonetheless, it has been observed that excess amounts of any one of these elements beyond the recommended dietary allowance may cause other long-term effects to happen within the human body.

The differences between *in vitro* and *in vivo* experiments can be significant. In the *in vivo* test, up to 4 times delayed corrosion rate was found in comparison with the *in vitro* Mg alloy test. The most used cytotoxicity tests are the direct contact qualitative test, MTT quantitative test, *etc.* The biocompatibility of medical devices or biomaterials that particularly come into touch with living tissue other than skin, such as sutures, surgical ligation films, implantable devices, *etc.*, can be evaluated using tables.[1,2,185] During clinical use, these tests may measure devices intended for either short-term or long-term implantation. Both absorbable and non-absorbable components can be tested using implantation techniques. To incorporate a reasonable safety evaluation, the implant analysis should closely mirror the anticipated clinical use. The biocompatibility test result is also influenced by the implantation place or location, time, and geometrical and structural design.[75] For instance, pure Zn wire produced different results than pure Zn vascular stents. The corrosion rate measured for pure zinc samples during bone implantation is higher than during artery implantation, and the value changed over the course of implantation. For clinical applications, two methods are observed to know the degradation progress of Mg-based implants, which include hydrogen gas release measurements and metal detection. Most of the studies are based on *in vitro* tests, but detailed work *viz. in vivo* tests to determine the biological, chemical, and mechanical relation between implants and animals is required to be done in, which may help in controlling the mechanical properties in different locations and different heat conditions.[186]

**4.3.1 Mg-based BMs.** Amongst the different biodegradable metallic materials, Mg showed the required biocompatibility as an implant material for the human body, as it exhibits nontoxic behaviour to the cells and encourages cell attachment characteristics.[122,187,188] Moreover, the suggested daily consumption of Mg for adults is about 320–400 mg and the excess presence of Mg in the body can be excreted through the urine.[1] Therefore, it is believed that the decomposition of $Mg^{2+}$ ions from implant decay cannot cause any damage to tissues in the human body. No side effects of Mg overdose have been reported in the open literature. Apart from this, Mg does not express any toxicity to the cells, while serum-containing Mg levels exceeding 1.05 mmoll$^{-1}$ could lead to muscular diseases, low blood pressure, and respiratory distress. The production of extra hydrogen because of the body's corrosion reaction is the sole problem mentioned with the *in vivo* use of Mg.[189] Fig. 15(a) and (b) show the schematic illustration of AM of WE43 and the fabricated cylindrical specimens, respectively. Each group's pre-degraded samples underwent live-dead staining to further investigate cell adhesion to the different surface conditions in actual scenarios and assess the direct effects of Mg degradation and sample morphology on cell viability (Fig. 15(c)). The study was validated because, in contrast to the nontoxic control, which was heavily covered in spindle-shaped living cells (green), the toxic control had neither living nor nearly any dead cells. The A- and E-series surfaces were completely covered in living cells, some of which were spherical and spindle-shaped,

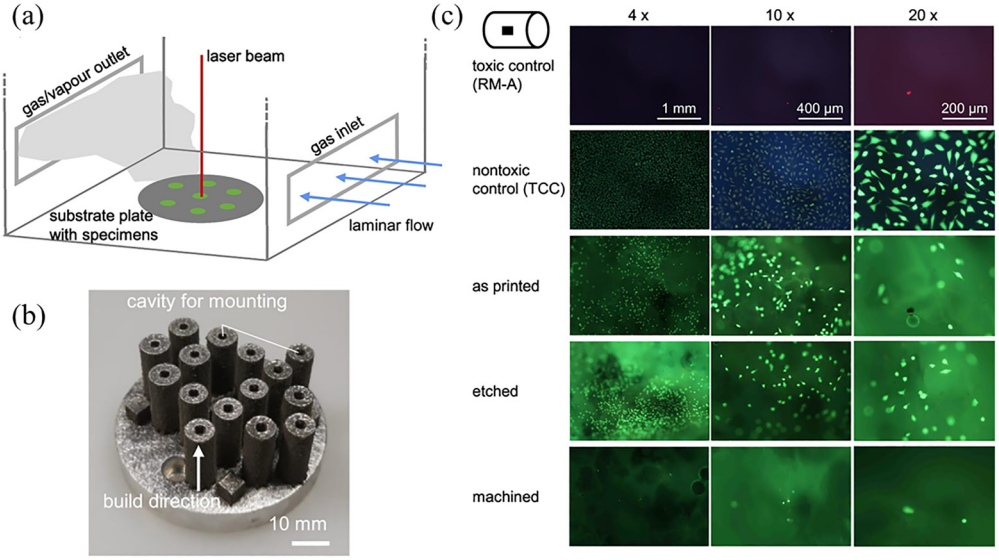


Fig. 15 (a) Process chamber schematic illustration during AM of Mg alloy; (b) cylindrical specimens affixed to the substrate plate; (c) live-dead staining of corroded samples for every surface condition of AM of WE43 (reproduced from ref. 154 with permission from Elsevier, Copyright 2021).

even though none of the three groups had any dead (red stained) cells. M-series samples, on the other hand, primarily displayed neither dead nor enough living cells on their surface, with very few living cells visible.[190]

**4.3.2 Zn-based BMs.** Zinc-based alloys are attractive options for a range of biological applications because of their encouraging cytocompatibility characteristics. Their biodegradability minimizes harmful effects while enabling the controlled release of vital zinc ions, which may foster tissue regeneration and cell proliferation. Research suggests that these alloys affect the behavior of important cell types such as endothelium and osteoblast involved in tissue regeneration, promoting responses that are favorable to healing. Their capacity to modify their surface and their low inflammatory response also contribute to their increased biocompatibility. Zn–2Al part fabricated using LPBF exhibited considerable cytocompatibility when exposed to CCK-8 assay for 7 days.[232] The number of cells in culture media grows considerably at prolonged culture time.[85] The cells tend to show a distinctive slender shape and start to construct an elongated filopodia after extended culture time (*i.e.*, after 4, 7 days). In the Zn alloy system, the increase in $Zn^{2+}$ and $OH^{-}$ concentration with osmotic pressure in the culture medium is caused by the degradation to further affect the survival and function of cells.[86] Zhang *et al.*[191] found that while an optimal alkaline environment encourages osteoblast cell growth, increasing osmolality may negatively affect osteoblast cell proliferation. Conversely, an excess amount of Zn can cause neurotoxicity.[86] Consequently, for long-term protection, regulating the degradation behaviour of either of these materials is important. In another work, cell viability cultivated, using the CCK-8 assay, in extracts of SLM processed Zn–*x*Mg for 1, 3, and 5 days was quantitatively examined; the findings are displayed in Fig. 16(a) Cell cytotoxicity was recognized to be acceptable when cell viability was more than 75%. Extracts at 100% concentration reduced cell viability to 65.5% to 78.3%. Cell viability rose with dilution to 50%. These findings showed that SLM-processed Zn–3Mg might stimulate MG-63 cell proliferation rather than cause cytotoxicity. Fig. 16(b) displays fluorescence microscopy pictures of MG-63 cells cultured in extracts of SLM-processed Zn–*x*Mg for varying lengths of time. Red and green staining were applied to the dead and living cells, respectively.[86] It was evident that each test group had a sizable number of dead cells. All examined groups' MG-63 cells showed a characteristic fusiform shape after a day of culture, indicating normal cell development. Three days later, MG-63 cells grown in extracts showed many pseudopods, released extracellular matrix, and started to spread to neighboring cells, indicating that cell spreading and proliferation were going well.

**4.3.3 Fe-based BMs.** Pure Fe has been reported to exhibit sufficient cytocompatibility. However, a high amount of Fe was reported to cause lesions, stomach pain, weakness, and liver damage in the gastrointestinal tract.[2,86] The cytocompatibility of Fe-based alloys can be improved by adding different biocompatible elements to them. In one of the studies, it was inferred that Ag offered sufficient micro-galvanic sites that were found to be beneficial for increasing the corrosion rate of Fe-based alloy. Besides, the higher content of Ag in the Fe alloy matrix (Fe–30Mg–3Ag) offered the highest antibacterial rate compared to the study presented by Sotoudehbagha *et al.*[65] are shown in Fig. 17A. The lower cellular molecular activity of Fe–30Mg–3Ag material towards human cells was attained when compared with (Fe–30Mg–1Ag).

Based on the better haemolysis results, it was recommended that developed Fe alloys could be used as excellent biomaterials. Furthermore, compared to cast pure Fe, the platelets that were deposited on the surface of sintered Fe-based products were found to be lower. The upper surface of the developed Fe alloys had a smooth, spherical platelet shape.[100]

The cytotoxicity behavior of Fe-based alloys was evaluated by preparing the liquid medium. This medium was cultured with

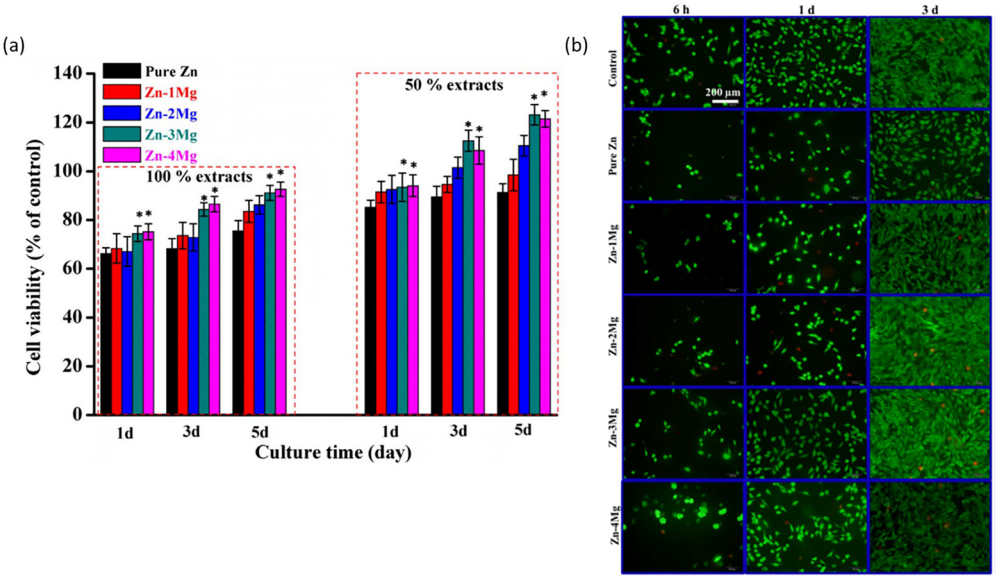


Fig. 16 (a) MG-63 cells grown in extracts of SLM-processed Zn–*x*Mg and their quantitative viability data. The control group was used to normalise the data. Between the test group and the pure Zn group, the values were mean ± SD, $n = 3$, $*p < 0.05$; (b) fluorescence microscopy pictures of cells grown for varying lengths of time in 100% extracts. For every image, the scale bar was 200 μm (reproduced from ref. 86 with permission from Elsevier, Copyright 2018).

Murine fibroblast cells (L-929), rodent vascular smooth muscle cells (VSMC), and human umbilical vein endothelial cells (ECV 304) in the Dulbecco's modified Eagle's medium (DMEM). Further, the prepared medium was treated under a humidified atmosphere with 5% $CO_2$ at 37 °C and then the extracted medium was collected and stored at 4 °C for cytotoxicity test.[192] From Fig. 17B, it was observed that the cell growth rate of VSMC was reduced because of the addition of ferrous ions in the culture media. The formation of ferrous ions was a degraded product of stent implementation. This result could have beneficial effects on the control of neointimal cell proliferation. The same results were also found in the study reported by Moravej *et al.*[193] According to Zhu *et al.*,[194] Fe ions essentially do not affect the metabolic activity of ECV304 cells when the concentration of Fe is less than 50 μg $ml^{-1}$. The current work found that ECV304 cells cultivated with Fe–X binary alloy (here, X = Mn, Co, Al, or W) extracts had greater viability than VSMC cells, which is a major benefit for use as coronary stents. After three days, the vitality of endothelial cells in the presence of iron was on par with 316L SS; however, viability was slightly lower over the first two days. On day four, the viability of the other two cell types, as well as endothelial cells, increased. The roles of the Fe storage protein ferritin and the Fe transport protein transferrins may be responsible for this.[192] In body fluids or tissues, Fe does not exist as a free ion. Bound to transferrin, just a minuscule portion of the body's total Fe circulates in the plasma and other extracellular fluids. Transferrin within Fe is transported across several cellular compartments by plasma and extracellular fluids. Most Fe loss occurs in the gastrointestinal system because of biliary haemoglobin breakdown products, shed enterocytes, and extravasated erythrocytes. Less is lost as skin cells shed and are lost in the urine. Although it is believed that Fe can be expelled from the body as ions, insoluble Fe hydroxide precipitate is the primary corrosion product of Fe in biological contexts. Fe-rich macrophage accumulations and multinucleated giant cell accumulations can occur in clusters or sparse, isolated locations. Despite the extensive research on Fe transportation in the human body, the relationship between Fe hydroxide precipitate and macrophages remains unclear. More research is needed to be done on the mechanism by which the human body excretes corrosion.

**4.3.4 Preclinical and clinical studies of biodegradable metallic implants.** The translation of biodegradable metallic biomaterials from laboratory-scale research to clinical applications has been supported by an increasing number of preclinical and early clinical studies. These studies provide critical insights into *in vivo* degradation behaviour, biocompatibility, mechanical integrity, and long-term performance of Mg-, Zn-, and Fe-based alloys in biomedical environments.[23]

Mg-based alloys are the most extensively studied biodegradable metals in both preclinical and clinical settings, particularly for orthopedic applications. Several *in vivo* animal studies have demonstrated that Mg-based implants, such as screws and plates, exhibit favourable biodegradation behaviour and promote bone regeneration without causing adverse inflammatory responses.[195,196] Clinical studies on Mg-based screws (*e.g.*, Mg-Y-RE-Zr alloys, commercialized as MAGNEZIX®) have shown successful outcomes in fracture fixation, with gradual degradation and replacement by natural bone tissue.[197,198] These findings indicate that Mg-based implants can provide sufficient mechanical support during healing while eliminating the need for secondary removal surgeries.

Zn-based alloys are currently in the preclinical stage but have shown promising results for cardiovascular and orthopedic applications. *In vivo* studies have demonstrated that Zn-based

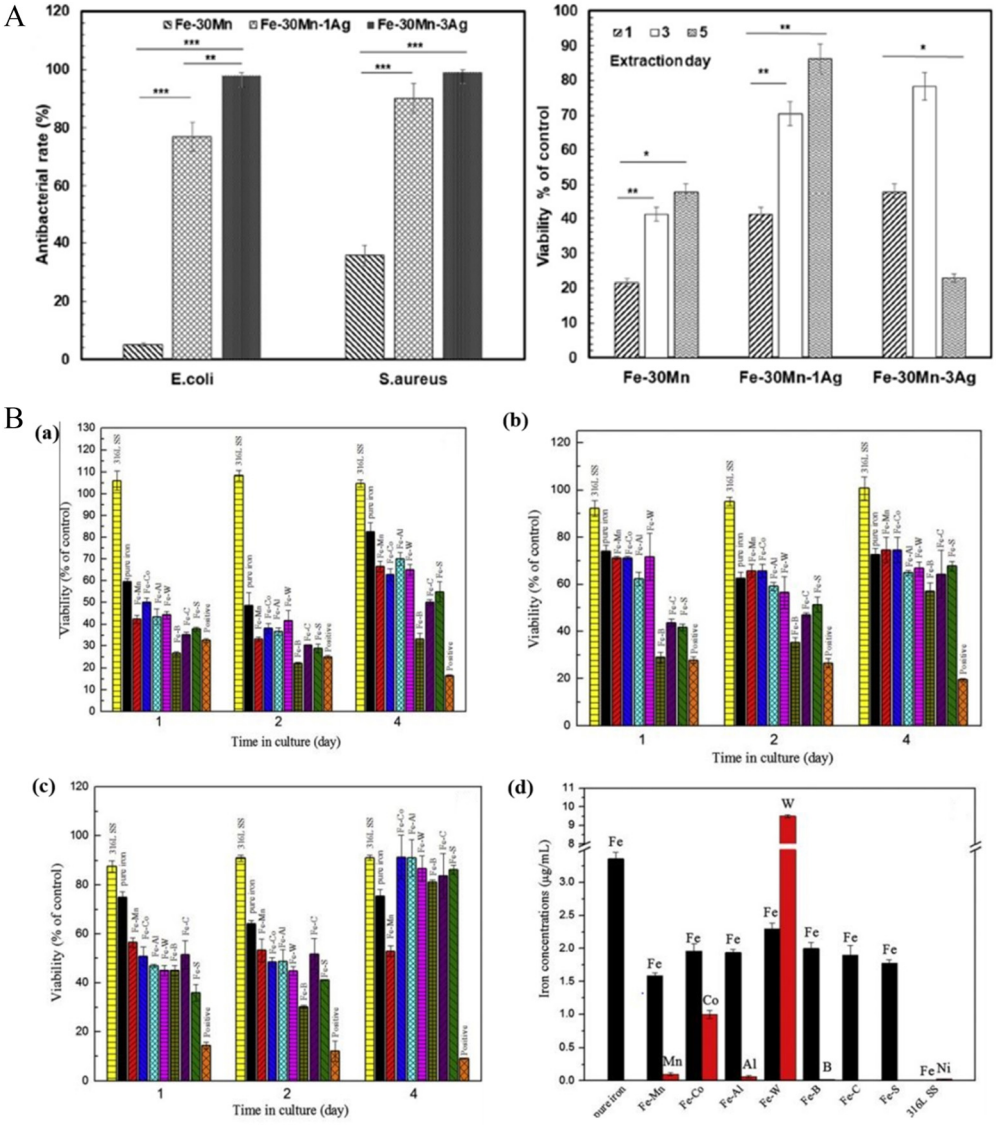


Fig. 17 (A) Illustration of antibacterial rate and cell viability of Fe–30Mn, Fe–30Mn–1Ag, Fe–30Mn–3Ag (reproduced from ref. 65 with permission from Elsevier, Copyright 2018); B. Illustration of cell viability of (a) L-929, (b) VSMC, (c) ECV304 after 1,2, and 4 days incubation and for reference consider stainless steel 316L and (d) released Fe ions concentration in the extract media utilized for cytotoxicity test (reproduced from ref. 192 with permission from Elsevier, Copyright 2011).

implants exhibit controlled degradation rates and good cytocompatibility, with minimal inflammatory response.[199,200] Zn-based stents have been investigated in animal models, showing uniform degradation and acceptable vascular healing behaviour.[165] However, further long-term studies and clinical trials are required to validate their safety and performance in human applications.

Fe-based alloys have also been evaluated in preclinical studies, particularly for cardiovascular stent applications. Early *in vivo* studies have demonstrated good biocompatibility and absence of thrombosis or severe inflammatory reactions.[179,201] However, the slow degradation rate of Fe remains a major limitation, as residual material may persist for extended periods. Strategies such as alloying with Mn or introducing porosity through additive manufacturing have been explored to accelerate degradation in vivo.[23]

Overall, while Mg-based alloys have reached early clinical application, Zn- and Fe-based systems are still under active investigation. Continued research focusing on degradation control, mechanical optimization, and long-term biological response is essential to enable the widespread clinical adoption of biodegradable metallic implants.

**4.3.5 Biosafety and cytocompatibility of Mg-, Zn-, and Fe-based alloys.** Biosafety and cytocompatibility are critical considerations for biodegradable metallic implants, as degradation products interact directly with surrounding tissues and physiological systems. The biological response depends on ion release, degradation rate, local pH changes, and accumulation

of corrosion products. Mg-, Zn-, and Fe-based alloys exhibit distinct biosafety profiles due to their differing degradation mechanisms and biological roles.

Mg-based alloys generally exhibit high cytocompatibility, as magnesium is an essential element involved in numerous biological processes. *In vitro* studies have demonstrated that Mg-based materials support cell adhesion and proliferation, with cell viability typically exceeding 80–90% under controlled degradation conditions. However, rapid degradation may lead to localized alkalization and hydrogen gas evolution, which can negatively affect surrounding tissues if not properly controlled.[148,188,233]

Zn-based alloys also demonstrate favourable cytocompatibility, with cell viability typically reported in the range of 75–90%, depending on alloy composition and ion concentration. Zinc plays a key role in cellular metabolism and enzymatic activity, and its controlled release can promote cell proliferation. However, excessive Zn ion concentrations may lead to cytotoxic effects, highlighting the importance of controlling degradation rates.[141,142]

Fe-based alloys exhibit moderate to high cytocompatibility, with reported cell viability values typically between 70–85%. Iron is an essential element involved in oxygen transport and metabolic processes; however, its slow degradation may result in prolonged exposure to corrosion products. Accumulation of iron ions and corrosion residues may influence local biological responses, necessitating careful control of degradation behaviour.[23]

Overall, Mg-based alloys provide excellent biological compatibility but require control over rapid degradation, Zn-based alloys offer a balanced cytocompatibility profile with controlled ion release, and Fe-based alloys demonstrate acceptable biosafety with limitations related to slow degradation. Therefore, optimization of composition, microstructure, and additive manufacturing parameters is essential to ensure safe clinical performance. Table 3 highlights key biosafety parameters.

### 4.4. Process characteristics

A thorough comparative analysis of AM process characteristics across Mg, Zn, and Fe biodegradable alloy systems reveals both commonalities and fundamental differences. Evaporation tendency follows the clear ranking with Zn being the highest and Fe lowest. This tendency is directly correlated with melting point and vapor pressure of alloy systems. Additionally, oxidation tendency appears to be highest for Mg and lowest for Zn specifically in terms of reactivity and processing challenges. Crack sensitivity is highest for Mg (thermal stress-induced), moderate for Zn (evaporation-coupled), and lowest for Fe (stable processing). A comparison table (Table 4) summarizes key characteristics and unified mechanism drivers for each material system. Mg requires a careful balance between suppressing evaporation and preventing cracking within a very narrow processing window, while also addressing powder handling and safety concerns. Zn on the other hand, experiences even more severe evaporation, which significantly restricts densification and results in the tightest process window among the three materials. In contrast, Fe exhibits comparatively stable processing with negligible evaporation, enabling greater emphasis on microstructural control rather than defect mitigation.

Future progress requires quantitative thermodynamic modeling, multi-physics simulation, *in situ* monitoring, and systematic

Table 3 Comparative cytocompatibility and biosafety

| Material | Cell viability (%) | Ion effect | Key biosafety concern | Ref. |
|---|---|---|---|---|
| Mg-based alloys | 80–95 | $Mg^{2+}$ supports cell growth | Rapid degradation, pH increase, $H_2$ evolution | 148, 188 and 233 |
| Zn-based alloys | 75–90 | $Zn^{2+}$ promotes enzymatic activity | Cytotoxicity at high ion concentration | 141 and 142 |
| Fe-based alloys | 70–85 | Fe ions support metabolism | Ion accumulation, slow degradation | 136 |

Table 4 Comparative analysis of AM process characteristics across Mg, Zn, and Fe biodegradable alloy systems

| Material system | Evaporation tendency | Oxidation tendency | Crack sensitivity | Key AM challenge | Unified mechanism driver |
|---|---|---|---|---|---|
| Mg based alloys | High evaporation during melting; requires continuous fume removal; constrains process windows[202,203] | Very high oxygen affinity; forms stable MgO; powder flammability; requires stringent atmosphere control[202,204] | High thermal stress induced microcracking; wide solidification ranges promote hot cracking[202–204] | Balancing evaporation avoidance with crack prevention in narrow energy window; powder safety[202,203] | Melt-pool temperature exceeds vapor pressure threshold; high thermal gradients induce residual stresses; reactive surface chemistry[202,203] |
| Zn based alloys | Very high to severe evaporation is dominant defect mechanism; narrowest process window; significant element loss and composition changes[84,91,205] | Moderate and forms ZnO with protective behavior; lower reactivity than Mg; controlled atmosphere ($<50$ ppm $O_2$) sufficient[206,207] | Moderate primarily evaporation coupled defects (porosity, keyholing, melt-pool instability) rather than thermal cracking[91,205] | Extreme evaporation limits densification; very narrow energy density window; melt-pool instability[91,205] | Lowest melting point and highest vapor pressure at processing temperatures drive mass loss; fluid dynamics disruption[84,205] |
| Fe based alloys | Minimal or almost negligible evaporation; stable melt pool behavior; no volatile element loss reported[208,209] | Moderate and controlled through atmosphere ($<0.1\%$ $O_2$); surface oxide formation; microalloying improves resistance[140,208] | Low stable solidification; defects primarily from lack of fusion or gas entrapment rather than cracking[208,209] | Microstructure control and degradation rate tuning rather than defect avoidance[140,210] | High melting point and low vapor pressure enable stable processing; broader energy density tolerance[208] |

Table 5 Study of mechanical, cytotoxicity, and immersion test properties of Mg and its alloys

| Ref | Material | AM tech | Mechanical properties | | | | | | In vitro test | Immersion test | Critical findings |
|---|---|---|---|---|---|---|---|---|---|---|---|
| | | | UTS | UCS | YS | E | Hardness | Elongation | | | |
| 58 | Mg (JBDM alloy) | LPBF | — | 32.34 ± 1.36 MPa | 16.25 ± 0.86 MPa | 0.760 ± 0.020 GPa | — | — | Cytotoxicity test Cells: MC3T3-E1 Incubation period: 6 h,1 d and 3 d Cck8 assay | 7d DMEM immersion test | Corrosion resistance and cytocompatibility increased with DCPD treatment on scaffolds compared to uncoated scaffolds |
| 19 | Mg alloy (Mg–5.9Zn–0.13Zr) | Binder-less 3D printing | — | 174 MPa | — | 18 GPa | — | — | — | — | AM of Mg samples had pore properties that resemble those of human bone, according to a mercury porosimetry investigation. |
| 60 | Mg alloy (WE43) | LPBF | 308.0± 1.0 MPa | — | 296.3 ± 2.5 MPa | 45.7 ± 1.5 GPa | — | — | — | — | AM creates samples with exceptionally high mechanical characteristics that resemble powder extruded samples and exhibit a homogeneous and dense microstructure, largely independent of the build direction. |
| 61 | Mg (WE43) | LPBF | — | — | 13 MPa | 750 MPa | — | — | Cytotoxicity test<br>Cell-MG-63<br>MTS assay Incubation period-72 h | −28 d immersion in SBF<br>Direct contact for 72 h of MG-63<br>Degradation rate = 20% volume loss in 4 weeks | Through topological design, AM of porous Mg may offer unique opportunities to modify the biodegradation profile.<br>Even after four weeks of biodegradation, the AM porous WE43 scaffolds' mechanical characteristics are comparable to those of trabecular bone. |
| 62 | Mg | LPBF | — | — | — | 0.59–0.95 GPa | 27–33 GPa | — | — | — | As the laser energy density increases, the grains in the molten zone coarsen and the average hardness value decreases |
| 63 | Mg | LPBF | — | — | — | — | 43.3 HV | — | — | 60 h SBF immersion test | The ideal laser energy density of 10.0 J $mm^{-1}$ produced dense magnesium parts free of pores and fractures.<br>As a protective layer, the degradation product $Mg(OH)_2$ reduced the rate of degradation. |
| 71 | Mg–*x*Sn (*x* = 0–7 wt%) | LPBF | — | 75 MPa | — | — | 65.7 HV | — | — | 10 d SBF immersion test | In the Mg–Sn alloy, with Zn content (0–4 wt%), the degradation rate decreases due to grain refinement and protective layer but with Zn content (4–8 wt%), it increases due to galvanic corrosion |
| 64 | Mg | LPBF | — | — | — | — | 52.4 HV | — | — | — | The surface morphology, roughness, and microhardness of LPBF bulk magnesium were clearly impacted by STI, a novel processing parameter. |
| 124 | Mg–*x*Zn (*x* = 2, 4, 6 and 8 wt%) | LPBF | — | — | — | — | 71.5 HV | — | — | 180 h SBF immersion test | Grain refinement and higher corrosion potential caused the degradation rate to slow down at a Zn concentration of 6%. |
| 66 | Mg Ca alloy | LAM | — | 111.19 MPa | — | 1.264 GPa | 60–68 HV | — | — | — | Because to grain refinement and solid solution strengthening, the microhardness is higher than that of as-cast pure Mg, and the porosity and surface morphology are dependent on the laser energy input. |
| 67 | Mg–*x*Mn (*x* = 0–3 wt%) | LPBF | — | 60.4 MPa | — | — | 61.3 HV | — | — | 250 h SBF immersion test | The improvement of Mg corrosion resistance was influenced by the refining of grains and the |

Table 5 (*continued*)

| Ref | Material | AM tech | Mechanical properties | | | | | | In vitro test | Immersion test | Critical findings |
|---|---|---|---|---|---|---|---|---|---|---|---|
| | | | UTS | UCS | YS | E | Hardness | Elongation | | | |
| | | | | | | | | | | | rise in corrosion potential brought on by the solid solution of Mn. |
| 68 | Mg–Gd–Zn–Zr alloy | LPBF | 332 ± 10 MPa | — | 325 ± 5 MPa | — | — | 4.0 ± 0.2% | — | — | During the LPBF process, element vaporization is mostly directed towards magnesium and zinc, with the ideal scanning speed and hatch spacing being 300–700 mm $s^{-1}$ and 100 μm, respectively. |
| 59 | Mg–9% Al | LPBF | — | — | — | — | 66–85 HV | — | — | — | During the experiment, a critical scanning speed of 0.02 m $s^{-1}$ can guarantee that the particles were thoroughly melted and did not evaporate. |
| 71 | Mg–5Sn–*x*Zn (*x* = 0, 2, 4, 6 and 8 wt%) | LPBF | — | — | — | — | 66–74 HV | — | — | 240 h SBF immersion test | As the Zn level grew, the alloys' rate of deterioration first dropped and subsequently increased, and their hardness also increased. The Mg-5Sn-4Zn alloy exhibited the best rate of deterioration. |
| 72 | Mg alloy AZ91D | LPBF | 296 MPa | — | 254 MPa | — | 100 HV | 1.24 –1.83% | — | — | Every sample's microhardness exhibits directional independence. Grain refinement and solid solution strengthening work together to give the LPBFed AZ91D better microhardness and tensile strength than the die-cast AZ91D. |
| 69 | Mg–5.2Zn–0.5Zr (ZK60) | LPBF | — | — | — | — | 78 HV | — | — | 48 h Hank's solution | At 94.05%, as-built components had the highest relative density. Following LPBF processing, a finer microstructure with less Mg–Zn precipitates was brought about by the compositional variation. |
| 70 | Mg–5.6Zn–0.5Zr (ZK60) | LPBF | — | — | — | — | 70.1–89.2 HV | — | — | — | ZK60 had an ideal hardness of 89.2 Hv, a relative density of 97.3%, and a hydrogen evolution rate of 0.006 ml $cm^{-2}$ $h^{-1}$ at a laser energy density of 600 J $mm^{-3}$. |
| 73 | Ti + Mg composite | Ink jet | — | 674 ± 58 MPa | 126 ± 12 MPa | 4.5 ± 1.0 MPa | — | — | Cytotoxicity test: Cells: SAOS-2 MTS assay Incubation period-1,3,5 days | 5 days 0.9%NaCl solution Immersion test | For porous Ti, the corrosion rate is nearly insignificant (∼1.14 μm per year), and for Ti–Mg composites, it is less than 1 mm peryear. The findings of the cell viability test showed that there was no to mild cytotoxicity. |
| 74 | Mg-38Zn | FFF | — | — | — | — | — | — | — | — | Because of the shear applied in the nozzle channel, the printed parts displayed a more refined microstructure than those that underwent statically applied heat treatment in the semi-solid stage. |

| Ref. | Material | AM tech | Mechanical properties | | | | | | | Immersion test | Critical findings |
|---|---|---|---|---|---|---|---|---|---|---|---|
| | | | UTS | CS | YS | E | Hardness | Elongation | *In vitro* test | | |
| 62 | Pure Mg | LPBF | — | — | — | 27–33 GPa | 56–94 Hv | — | | — | Fine equiaxed grains of the Mg phase were obtained owing to a higher cooling rate and rapid solidification during LPBF. The harness of the fabricated |

Table 5 (*continued*)

| Ref. | Material | AM tech | Mechanical properties | | | | | | *In vitro* test | Immersion test | Critical findings |
|---|---|---|---|---|---|---|---|---|---|---|---|
| | | | UTS | CS | YS | E | Hardness | Elongation | | | |
| | | | | | | | | | | | samples greatly improved according to the Hall–Petch equation. |
| 71 | ZK60-xNd | LPBF | — | 138.3–183.4 MPa | — | | 85.4–124.8 Hv | — | For 1 day culture, ZK60-3.6Nd extract (83.2%) showed higher cell viability of the MG-63 cells than ZK60 (67.5%), ZK60-1.8Nd (70.1%), and ZK60-5.4Nd (60.6%), which further increased to 93.5% for 5 days. | — | The combination of precipitation strengthening, fine grains strengthening, and solid solution strengthening played a major role in improving the micro-hardness of LPBFed-manufactured samples. |
| 211 | AZ61 (Al 6 wt%, Zn 1 wt. %, remaining Mg) | LPBF | — | — | — | — | 93 Hv | —- | — | 1.2 to 2.4 mm per year biodegradation rate following 24 to 144 hours of immersion | Mechanical properties like hardness were significantly increased due to grain refinement |
| 212 | Mg–6Al–1Zn*x*Y | Laser rapid melting | — | — | — | — | 90.9 Hv was observed for AZ61. Higher hardness was found as Y increased till 2 wt% from 0 wt% | — | | Increasing the Y content to 2 wt% in AZ61, demonstrated the least degradation rate ∼ 0.28 mmpy | Strengthening of the secondary phase led to the improvement in hardness values. |
| 213 | ZK30-*x*Cu | LPBF | — | — | — | — | 80–98 Hv | — | Under normal pH settings, it was discovered that combining 0.4% weight copper powder with ZK60 reduced the *Escherichia coli* colony count to zero after 72 hours, improving its antibacterial qualities. | Corrosion rate: ZK30–0.3Cu > ZK30–0.2Cu > ZK30–0.1Cu > ZK30 | Strengthening of the MgZnCu and $MgZn_2$ phases led to a boost in the hardness |
| 61 | Porous Mg (WE43) | LPBF | — | — | 0.012–0.015 GPa | 0.7–0.8 GPa | — | — | WE43 scaffolds showed less than 25% cytotoxicity. With the correct coating and design, Mg-based biomaterials could be a part of a new generation of functionally degradable biomaterials, especially in orthopedic applications, even though pure WE43 itself might not be the best surface for cell attachment. | — | The mechanical properties of LPBFed fabricated porous sample was found to be within the range of cancellous bone ($E$ = 0.5–0.8 GPa, $\sigma$ = 0.0001–0.016 GPa) even after 4 weeks of biodegradation. |

LPBF – laser powder bed fusion, LAM – laser AM, FFF – fused filament fabrication, STI – scanning time interval.

Table 6 Study of mechanical, cytotoxicity, and immersion test properties Zn and its alloys

| Ref. | Material | AM tech | Mechanical properties | | | | | | *In vitro* test | Immersion test | Critical findings |
|---|---|---|---|---|---|---|---|---|---|---|---|
| | | | UTS | UCS | YS | E | Hardness | Elongation | | | |
| 84 | Zn | LPBF | 137.9± 2.5 MPa | — | 122.± 2.61 MPa | 20.47 ± 5.71 GPa | 46.3 ± 2 HV | — | — | — | High densification and fine grains produced by ideal processing control of Zn evaporation and laser energy input were credited with the outstanding mechanical qualities. |
| 85 | Zn-*x* WE43 (*x* = 2,5 and 8) | LPBF | 154.1 MPa | 50.9 ± 3.1 MPa | 50.9 MPa | 2540 ± 203 MPa | — | — | — | — | Grain refining was the result of a rapid cooling rate and the addition of WE43. The structural design of porous scaffolds directly influenced their fracture behavior. |
| 68 | Mg-Gd–Zn–Zr alloy | LPBF | 332 ± 10 MPa | — | 325 ± 5 MPa | — | — | 4.0 ± 0.2% | — | — | The LPBFed GZ112K alloy has comparable elongation (+0.4%), a significantly higher YS (+162 MPa), and a UTS (+122 MPa) than the as-cast alloy. |
| 83 | Zn | LPBF | — | — | — | — | 42 ± 9 HV | — | — | — | Operating under inert gas in a confined chamber was insufficient. In an open chamber with an inert gas jet flow over the powder bed, process stability was achieved. Under ideal processing conditions, a part density of almost 99% was attained. |
| 214 | Zn | DMP | — | — | — | — | — | — | — | — | Appropriate process parameters were successfully estimated using single track scans. The hatch spacing in the 2D trials was selected to balance smoke generation and track overlap. The powder's flowability has a significant impact on the quality of the layers following DMP. |
| 86 | Zn–*x*Mg (*x* = 0–4 wt%) | LPBF | 166.4± 7.4 MPa | — | 131.6 ± 7.5 MPa | 57.5 ± 4.8 GPa | 198 ± 10.2 HV | — | More in Zn–3Mg than pure Zn; Cytotoxicity: Cck8 assay<br><br>Cell: MG-630 cytotoxicity | 7d SBF immersion 72 h;72 h;<br><br>Degradation rate = 0.10–0.18 mm per year; | Zn–3Mg alloy demonstrated enhanced cytocompatibility with human MG-63 cells. |
| 87 | Zn–*x*Ag (*x* = 0, 2, 4, 6, 8 wt%) | LPBF | — | 199–267 MPa | — | — | 55–80 HV | — | — | 21 d SBF immersion; Increase in corrosion rate with Ag | Because of the creation of galvanic micro-cells between the AgZn3 phase and the Zn matrix, the corrosion rate of Zn–x Ag alloys was improved compared to Zn, and the lowest grain was produced with 6 weight percent Ag. |

| Ref. | Material | AM tech | Mechanical properties | | | | | | *In vitro* test | Immersion test | Critical findings |
|---|---|---|---|---|---|---|---|---|---|---|---|
| | | | UTS | CS | YS | E | Hardness | Elongation | | | |
| 232 | Zn–2Al | LPBF | 192.2 ± 5.4 MPa | — | 141.7 ± 3.7 MPa | — | 64.5 ± 1.8 HV | 11.7 ± 1.9% | 0.13–0.16 mmpy | — | The energy density plays a vital role in the densification of the part, which further leads to enhance the mechanical properties of the Zn–2Al alloy. Zn–2Al alloy also showed good biocompatibility from *in vitro* cell experiments. |
| 86 | Zn–*x*Mg (*x* = 0–4 wt%) | LPBF | 43.2 ± 3.1–152.4 ± 4.8 MPa | — | 61.3 ± 5.0–222.3 ± 8.2 MPa | 12.2 ± 2.4–57.5 ± 4.8 GPa | 49.5 ± 5.6–198.6 ± 10.2 Hv | 1.7 ± 0.1–7.2 ± 0.4% | 0.10 ± 0.04 to 0.18 ± 0.03 mmpy | — | The incorporation of Mg up to 4 wt% in Zn resulted in improved mechanical properties without affecting its degradation rate and biocompatibility. The LPBF-processed Zn–Mg alloys showed adequate biocompatibility for the use of biomedical applications. |
| 215 | Pure Zn | LPBF | — | 99 ± 22 MPa | — | — | — | — | — | — | The findings demonstrated that laser melting produced a porous structure in Zn samples that resembled foam. The mechanical characteristics of materials processed with LPBF were contrasted with those of their rolled and as-cast equivalents. LPBF-processed Zn showed improved compressive strength to cast and wrought materials owing to the decrease in grain size and regardless of 12% of apparent porosity. |

Table 6 (*continued*)

| Ref. | Material | AM tech | Mechanical properties | | | | | | *In vitro* test | Immersion test | Critical findings |
|---|---|---|---|---|---|---|---|---|---|---|---|
| | | | UTS | CS | YS | E | Hardness | Elongation | | | |
| 126 | Pure Zn | LPBF | — | — | — | — | 43.8 Hv | — | — | — | For stable melting of Zn powder and to counter the adverse effects of vaporization, a gas flow arrangement was proposed. |
| 91 | Pure Zn | LPBF | 137.9 ± 2.48 MPa | — | 122.13 ± 2.61 MPa | 20.47 ± 5.71 GPa | 46.31 ± 2.02 Hv | 8.13 ± 0.55% | — | — | The LPBF-processed parts possessed a high density with superior mechanical properties. The main reason for the porous parts was the lack of laser energy and hindrance of gas flow due to the huge vaporization of Zn powders. |

DMP – direct metal printing.

Table 7 Study of mechanical, cytotoxicity, and immersion test properties of Fe and its alloys

| Ref. | Material | AM tech | Mechanical properties | | | | | | *In vitro* test | Immersion test | Critical findings |
|---|---|---|---|---|---|---|---|---|---|---|---|
| | | | UTS | UCS | YS | E | Hardness | Elongation | | | |
| 96 | Fe Mn Ca alloy | Binder jetting | 296.6 ± 45 MPa | — | 189.7 ± 25.6 MPa | 39.1 ± 0.5 GPa | — | — | Fe–Mn and Fe–Mn–1Ca has good cytocompatibility<br>Cytotoxicity test: cell-MC3T3 Incubation period: 72 h Direct live/dead and indirect MTT cell viability assays; | 28 d HBSS corrosion immersion | An increase in degradation rates was projected when Ca and Mg were added to a Fe-35 weight percent Mn solid solution.<br>In tensile tests, Fe–Mn–1Ca showed greater stiffness and brittle failure; however, a larger UTS was noted compared to Fe–Mn, most likely as a result of micropores. |
| 95 | Fe Mn Alloy powder | Inkjet | 115.53 MPa | — | 106.07 ± 8.2 MPa | 32.47 ± 5.05 GPa | — | — | Direct and indirect pre-osteoblast cell viability tests Cell-MC3T3-E1 Incubation period: 72 h | HBSS immersion test | The 3D printed Fe–Mn corroded far more quickly than pure Fe, according to electrochemical corrosion experiments. Additionally, cell infiltration into the 3D printed scaffolds' open pores was noted. |
| 98 | Fe (CIPs) | Micro extrusion-based 3D printing | 370 MPa | — | 35 MPa | 10 MPa | — | — | — | — | There was no discernible variance in the size of the planned porous scaffolds, and the established approach proved to be adaptable in producing various pore morphologies. |
| 2 | Fe (CIPs) | SLA | 218.67 MPa | — | 4.66 MPa | 13.17 MPa | — | — | — | SBF immersion test | Appropriate bonding of carbonyl Fe particles was accomplished even in the absence of pressure. |

CIP – carbonyl Fe particle, SLA – stereolithography.

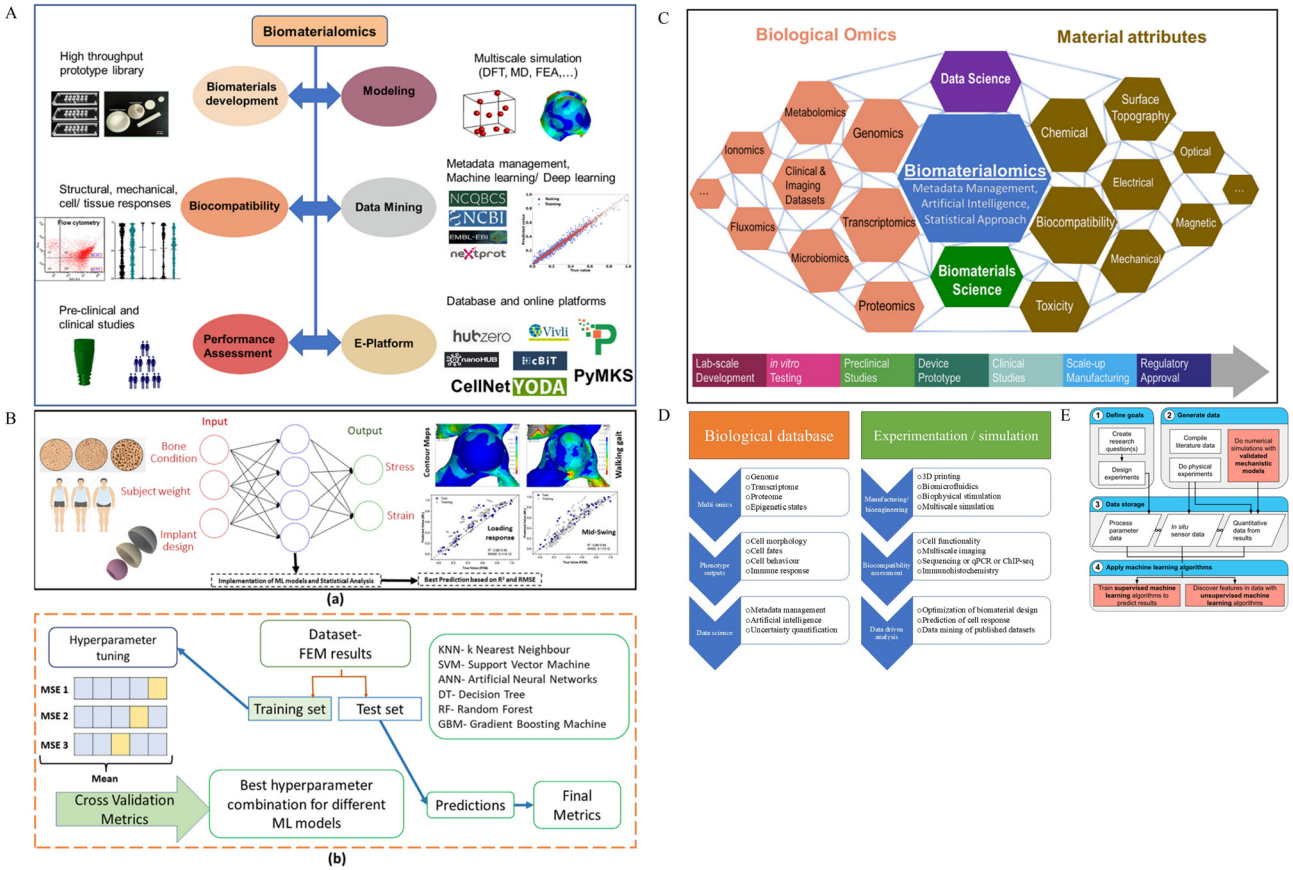


Fig. 18 (A) Utilizing computational, data science, informatics, and experimental technologies for design, characterization, and biocompatibility/performance evaluation are key components of Biomaterialomics (reproduced from ref. 217 with permission from Elsevier, Copyright 2022); (B) To provide individualised care, patient-dedicated implants with innovative design concepts are essential for musculoskeletal regeneration and reconstruction (reproduced from ref. 217 with permission from Elsevier, Copyright 2022); (C) introducing the idea of Biomaterialomics, an interdisciplinary field of study that aims to understand how biological information relates to the characteristics of materials (reproduced from ref. 217 with permission from Elsevier, Copyright 2022); (D) an example of the design process for next-generation biomaterials;[217] (E) application of ML in AM (reproduced from ref. 218 under Creative Common License from Elsevier, Copyright 2021).

evaluation of alternative AM processes. Material-specific optimization strategies should be developed while pursuing a deeper understanding of the underlying unified mechanisms.

## 5. Prospects of machine learning in AM of biodegradable materials

In additive manufacturing (AM), machine learning (ML) is becoming a game-changing technique, especially for the creation of BMs for use in biomedical applications.[216] ML offers a methodical way to address the issues mentioned in previous sections, such as microstructural control, defect development, and corrosion behaviour, by combining experimental data, process comprehension, and mechanistic models. Future biomaterials will be generated using AI, data science, and sophisticated machine learning algorithms, as shown in Fig. 18(A–D). The applications of ML are shown in Fig. 18E. The following categories apply to the main ML application situations in AM-BMs:

### 5.1 Process parameter optimization

Large datasets of process parameters, including laser power, scan speed, hatch spacing, and volumetric energy density (VED), can be analyzed by ML models to forecast the best configurations for obtaining the required microstructures and mechanical qualities.[218] The problems of anisotropy, porosity, and surface roughness can be immediately addressed by this method. For instance, in alloys, supervised learning algorithms and neural networks have been utilized to minimize porosity and prevent cracking, enhancing dimensional accuracy and structural integrity.[219]

### 5.2 Defect prediction and quality control

In AM-fabricated biomaterials, defects including porosity, lack-of-fusion, and hot cracks have a significant impact on corrosion rates and mechanical behavior. ML-based models can identify anomalies and forecast the development of defects by utilizing sensor data and real-time monitoring. Long short-term memory (LSTM) networks and convolutional neural networks (CNNs) are two methods that have shown promise in predicting these

flaws, allowing for proactive modification of process parameters to improve dependability and lower failure risk.[220]

### 5.2 Microstructure and property prediction

Microstructural parameters that directly affect corrosion behavior and degradation rates, such as grain size, phase distribution, and melt pool properties, can be linked by machine learning to processing settings. In order to develop implants with regulated biodegradation and mechanical strength, support vector machines and ensemble learning algorithms have been used to predict how changes in cooling rate or layer thickness effect microstructure.

### 5.3 Materials design and alloy development

By linking composition, processing parameters, and performance outcomes, machine learning speeds up the search for new biodegradable alloys. ML makes it easier to identify Fe-, Mg-, and Zn-based compositions that maximize mechanical characteristics, biocompatibility, and degradation rates by combining past experimental data with predictive modelling.[221]

### 5.4 Structural and biological performance optimization

ML is also used to design implant architecture, including porosity and surface topology, to enhance tissue integration and vascularization.[222] Algorithms can predict the effect of surface area, pore size, and distribution on cell proliferation and tissue growth, linking structural design with the biological performance discussed in Section 4.

### 5.5 Real-time monitoring and predictive maintenance

Continuous evaluation of implant quality and process stability is made possible by the combination of machine learning with *in situ* monitoring technologies. Real-time feedback systems reduce downtime and material waste while guaranteeing consistent quality in patient-specific implants by enabling the modification of parameters to minimize failures.

### 5.6 Challenges and future directions

The use of ML in AM-BMs has limits despite its potential. Experimental validation is still crucial, and high-quality, well-annotated datasets are necessary. It is also necessary to address ethical issues like data protection and model openness in medical applications. In order to create reliable, predictive frameworks for the production of biodegradable implants, future research will profit from integrating mechanistic knowledge, experimental data, and machine learning.

## 6. Challenges of employing AM of BMs

A number of challenges prevent additive manufacturing (AM) from being widely adopted for biomedical applications, despite its many benefits in producing Fe-, Mg-, and Zn- based BMs. These difficulties can be broadly divided into five categories: material-related, process-related, post-processing-related, economic-related, and operational constraints.

### 6.1 Material-related

The restricted choice of appropriate materials is one of the main drawbacks of AM in biodegradable biomaterials. Despite extensive research on systems based on Fe, Mg, and Zn, the variety of alloys that may be used with AM methods is still limited, which limits design flexibility. Another crucial issue is achieving accurate material characteristics and regulated degradation rates. Degradation and tissue healing rates must coincide for implant performance to be successful. However, it can be challenging to guarantee consistent degrading behavior[223] when AM techniques induce microstructure diversity, which could have a negative impact on clinical outcomes. Furthermore, maintaining material homogeneity is still difficult, especially in alloy systems. Variations in mechanical properties might result from inhomogeneous composition and microstructural irregularities, which eventually impact the biomaterial's performance and dependability.

### 6.2 Process-related

Layer-by-layer fabrication is a fundamental aspect of AM techniques, often resulting in anisotropic material properties. This anisotropy must be carefully taken into account during design and application since it can affect mechanical strength and long-term performance. The limited resolution of some AM methods is another drawback. The creation of complex biomedical implants may be hampered by the inability to produce extremely fine features or complex geometries with high precision. Additionally, AM-produced components frequently include flaws and surface roughness, particularly in powder-based methods. Both mechanical performance and biocompatibility may be adversely affected by surface roughness.[224] Further research is still needed in this field, even though recent studies (such as high-throughput techniques[225]) have shown possible strategies to minimize surface roughness without considerable post-processing.

### 6.3 Post-processing and quality control

Near-net-shape fabrication is made possible by AM, but in order to obtain the required mechanical and biological qualities, post-processing procedures like heat treatment, surface finishing, and polishing are frequently required.[226] These extra processes lengthen the production time, complicate the process, and may require certain tools and knowledge. Furthermore, it remains difficult to guarantee reproducibility and consistent quality across batches, especially when multiple post-processing stages are involved.

### 6.4 Economic and scalability constraints

Limited scalability is a major obstacle from an industrial standpoint. Although AM is very useful for small-batch production and prototyping, its use in large-scale manufacturing is currently limited. Its widespread usage is further limited by the high cost of equipment, particularly for metal-based AM systems. For applications that require large production volumes, these expenses may be unaffordable, potentially affecting overall economic viability.

### 6.5 Operational

The technical skills and specialized understanding are necessary for the successful application of AM technology. Skilled workers are needed for material selection, equipment handling, and process optimization. The successful acceptance and scalability of AM in biological applications may be hampered by the present lack of qualified personnel.

Although AM offers novel opportunities to produce biodegradable biomaterials, its full potential for creating sophisticated medical implants must be realized by acknowledging and addressing these constraints and disadvantages. The goal of current research and technological developments is to overcome these obstacles and improve AM's potential for biodegradable biomaterials.

## 7. Future prospects and research gaps

### 7.1 Critical research gaps

Despite significant progress in the development of biodegradable metallic biomaterials, several critical research gaps remain that limit their widespread clinical adoption. One of the primary challenges is the precise control of degradation behaviour, particularly for Mg- and Fe-based alloys. Mg alloys exhibit excessively rapid degradation, leading to premature loss of mechanical integrity and hydrogen gas evolution, while Fe alloys degrade too slowly, resulting in long-term residue accumulation. Zn-based alloys offer intermediate degradation rates; however, further optimization is required to tailor degradation kinetics for specific clinical applications.

Another key challenge lies in the optimization of mechanical properties to match those of biological tissues. While Mg alloys exhibit elastic modulus values close to natural bone, their strength decreases rapidly during degradation. In contrast, Fe-based alloys possess high strength but significantly higher stiffness than bone, leading to stress shielding. Zn alloys provide moderate mechanical performance but require further strengthening for load-bearing applications. Therefore, achieving a balance between mechanical integrity and controlled degradation remains a major research focus.

Biosafety and long-term biological response also require further investigation. Although Mg, Zn, and Fe are essential elements in the human body, excessive ion release, local pH changes, and accumulation of corrosion products may affect cellular response and tissue regeneration. Standardized *in vitro* and *in vivo* evaluation protocols are currently lacking, making it difficult to directly compare results across studies.

From a manufacturing perspective, additive manufacturing (AM) introduces additional complexities, including process-induced defects, anisotropy, and variability in microstructure. Further research is needed to establish robust process–structure–property relationships and to ensure reproducibility and scalability of AM-fabricated biodegradable implants.

### 7.2 Future research directions

Future research directions should focus on:

- Advanced alloy design and compositional tuning to control degradation and mechanical properties
- Surface modification and coating strategies to enhance corrosion resistance and biocompatibility
- Development of functionally graded and porous structures using AM to tailor mechanical and biological performance
- Integration of machine learning and data-driven approaches for process optimization and predictive modelling
- Establishment of standardized testing protocols for degradation, cytocompatibility, and mechanical evaluation

Addressing these challenges will be essential for advancing biodegradable metallic biomaterials toward reliable and widespread clinical applications.

With continuous developments in technology, materials science, and biomedical engineering, the field of biomaterials, especially those based on Fe, Mg, and Zn, presents a very promising future for AM. The following significant opportunities and developments are influencing AM's path in the creation of biodegradable implants:

**7.2.1 Material innovation and alloy development.** One of the main areas of research continues to be the creation of biocompatible and biodegradable metals. In order to fit particular biomedical applications, ongoing efforts are focused on creating Fe-, Mg-, and Zn-based alloys with customized degradation rates and optimal mechanical properties.[56] Advanced material compositions are being investigated concurrently to enhance mechanical performance and control over deterioration behavior. Better implant integration and long-term functionality are the goals of these advancements.[227]

**7.2.2 Design and structural optimization.** AM makes it possible to create extremely complex and bioresorbable structures, creating new opportunities for patient-specific implant design.[224,228] Implant adaptability to specific anatomical requirements is improved by the capacity to produce complex geometries. Customized porosity and microstructure control, which may be adjusted during the AM process to encourage tissue ingrowth, vascularization, and ideal implant integration, present a significant possibility. Additionally, the integration of various biomaterials into a single construction is made possible by developments in multi-material printing.[50,229] This feature makes it easier to develop hybrid implants with multifunctional performance and region-specific characteristics.

**7.2.3 Process advancements and precision control.** It is anticipated that future advancements will make it possible to precisely regulate degradation rates, enabling implants to deteriorate in tandem with tissue repair mechanisms.[230] This will lower problems and greatly improve clinical outcomes. Another revolutionary approach is the idea of *in situ* 3D printing for surgical purposes. Personalized medicine and emergency treatment could be revolutionized by real-time implant creation in the operating room. Furthermore, including real-time monitoring and feedback systems into AM procedures and implants will yield insightful information about patient reaction, implant performance, and degradation behavior.

**7.2.4 Functional and smart biomaterials.** An important development is the creation of bioactive implants, which actively encourage tissue regeneration and repair by incorporating therapeutic substances like medications or growth factors

Table 8 Comparative properties and biomedical applications of biodegradable Mg-, Zn-, and Fe-based alloys

| Property | Mg-based alloys | Zn-based alloys | Fe-based alloys |
|---|---|---|---|
| Degradation rate (mm per year) | 1–5 | 0.1–0.5 | 0.01–0.1 |
| Elastic modulus (GPa) | 20–45 | 70–110 | 180–210 |
| Ultimate tensile strength (MPa) | 100–300 | 100–300 | 300–600 |
| Biocompatibility | High | High | Moderate–high |
| Corrosion behaviour | Rapid electrochemical corrosion with $H_2$ evolution | Uniform corrosion without gas evolution | Passive oxide layer formation |
| Key limitation | Rapid degradation, hydrogen gas formation | Lower mechanical strength | Very slow degradation |
| Typical biomedical applications | Orthopedic implants (bone screws, plates, scaffolds) | Cardiovascular stents, temporary implants | Load-bearing implants, structural devices |
| Suitability summary | Bone-like modulus, fast resorption | Balanced degradation and strength | High strength, long-term support |
| Ref. | 21, 29, 75 and 231 | 75, 141 and 142 | 21 and 138 |

inside the biomaterial. The development of smart biomaterials, which react to changes in the environment or physiological stimuli, is closely related. These materials improve patient care by enabling dynamic implant adaptation, real-time feedback, and possibly therapeutic reactions.

**7.2.5 Personalized medicine and patient-specific solutions.** AM is anticipated to be a key player in the development of precision medicine by creating implants tailored to individual patients. Implants can be tailored to enhance compatibility, functionality, and treatment results by utilizing patient data, such as anatomical geometry and medical history.

**7.2.6 Regulatory, standardization, and sustainability aspects.** Regulations are being revised to account for the unique properties of additively manufactured biomaterials as AM technology advances.[50] Faster clinical translation and adoption will be made possible by streamlined approval procedures. Furthermore, to guarantee uniformity, safety, and dependability in AM-produced biomaterials, international cooperation and standardization initiatives among academics, business, and regulatory organizations are crucial. Lastly, efforts to promote sustainability are becoming more significant, with an emphasis on eco-friendly materials, lower energy use, and effective production techniques. These initiatives improve AM's appeal for widespread use and match it with global sustainability goals.[54]

A comparative summary of the key mechanical properties, degradation behaviour, and biomedical applications of Mg-, Zn-, and Fe-based biodegradable alloys is presented in Table 8, providing a framework to guide material selection and future research directions.

The prospects for AM of biomaterials based on Fe, Mg, and Zn in the future are characterized by the convergence of advancements in technology, materials, and regulations. As these trends develop, AM's potential in the biomedical domain is set to transform patient care by providing never-before-seen levels of biodegradable implant customization, accuracy, and functionality.

# 8. Conclusion

This review provides a comprehensive overview of additive manufacturing of biodegradable Mg-, Zn-, and Fe-based metallic biomaterials, with emphasis on process-structure–property relationships and their implications for biomedical applications. A comparative analysis of these materials reveals distinct advantages and limitations that influence their clinical suitability.

Mg-based alloys exhibit elastic modulus values (20–45 GPa) comparable to natural bone, making them highly suitable for orthopedic applications. However, their rapid degradation rates (1–5 mm per year) and hydrogen gas evolution remain key challenges that require further control. Zn-based alloys demonstrate moderate mechanical properties and controlled degradation rates (0.1–0.5 mm per year), positioning them as promising candidates for cardiovascular stents and temporary implants. Their balanced combination of degradation behaviour and cytocompatibility makes them particularly attractive for applications requiring gradual resorption. Fe-based alloys offer superior mechanical strength (300–600 MPa) and structural stability, but their slow degradation rates (0.01–0.1 mm per year) limit their effectiveness as fully biodegradable implants. Strategies such as alloying and structural design are necessary to enhance their degradation performance. In terms of cytocompatibility, Mg and Zn alloys generally exhibit higher cell viability ($>80$–90%), while Fe-based systems show moderate cytocompatibility ($\sim$70–85%), primarily influenced by degradation behaviour and ion release.

Overall, Mg alloys are best suited for applications requiring rapid resorption and bone compatibility, Zn alloys provide an optimal balance between degradation and biological performance, and Fe alloys are suitable for load-bearing applications where prolonged mechanical support is required. Despite significant advancements, challenges related to degradation control, mechanical optimization, biosafety, and manufacturing reproducibility remain. Future research integrating advanced alloy design, additive manufacturing optimization, and data-driven approaches will play a crucial role in enabling the successful clinical translation of biodegradable metallic implants.

# Conflicts of interest

The authors declare no conflicts of interest.

# Data availability

No primary research results, software or code have been included and no new data were generated or analysed as part of this review.

## References


1 A. Kumar and P. M. Pandey, *J. Magnesium Alloys*, 2020, **8**, 883–898.
2 P. Sharma and P. M. Pandey, *Proc. Inst. Mech. Eng., Part C*, 2018, **233**, 1876–1895.
3 P. Sharma and P. M. Pandey, *Mater. Des.*, 2018, **160**, 442–454.
4 D. K. Pathak and P. M. Pandey, *Proc. Inst. Mech. Eng., Part C*, 2020, **234**, 2863–2880.
5 F. Witte, F. Feyerabend, P. Maier, J. Fischer, M. Störmer, C. Blawert, W. Dietzel and N. Hort, *Biomaterials*, 2007, **28**, 2163–2174.
6 R. del Campo, B. Savoini, A. Muñoz, M. A. Monge and R. Pareja, *J. Mech. Behav. Biomed. Mater.*, 2017, **69**, 135–143.
7 M. Mozafari, A. Bordbar-Khiabani and B. Yarmand, *Emerging Mater. Res.*, 2020, **8**, 305–319.
8 E. Ghasali, M. Alizadeh, M. Niazmand and T. Ebadzadeh, *J. Alloys Compd.*, 2017, **697**, 200–207.
9 J. M. Seitz, A. Lucas and M. Kirschner, *Jom*, 2016, **68**, 1177–1182.
10 A. Francis, Y. Yang, S. Virtanen and A. R. Boccaccini, *J. Mater. Sci. Mater. Med.*, 2015, **26**, 1–16.
11 H. Hermawan, H. Alamdari, D. Mantovani and D. Dubé, *Powder Metall.*, 2008, **51**, 38–45.
12 M. F. Ulum, A. Arafat, D. Noviana, A. H. Yusop, A. K. Nasution, M. R. Abdul Kadir and H. Hermawan, *Mater. Sci. Eng., C*, 2014, **36**, 336–344.
13 S. Zhu, N. Huang, L. Xu, Y. Zhang, H. Liu, H. Sun and Y. Leng, *Mater. Sci. Eng., C*, 2009, **29**, 1589–1592.
14 Y. Li, H. Jahr, K. Lietaert, P. Pavanram, A. Yilmaz, L. I. Fockaert, M. A. Leeflang, B. Pouran, Y. Gonzalez-Garcia, H. Weinans, J. M. C. Mol, J. Zhou and A. A. Zadpoor, *Acta Biomater.*, 2018, **77**, 380–393.
15 T. Huang, J. Cheng, D. Bian and Y. Zheng, *J. Biomed. Mater. Res., Part B*, 2016, **104**, 225–240.
16 H. Yang, B. Jia, Z. Zhang, X. Qu, G. Li, W. Lin, D. Zhu, K. Dai and Y. Zheng, *Nat. Commun.*, 2020, **11**, 401.
17 G. Tripathi and P. M. Pandey, *Proc. Inst. Mech. Eng., Part C*, 2023, **237**, 5933–5950.
18 M. Yazdimamaghani, M. Razavi, D. Vashaee, K. Moharamzadeh, A. R. Boccaccini and L. Tayebi, *Mater. Sci. Eng., C*, 2017, **71**, 1253–1266.
19 M. Salehi, S. Maleksaeedi, M. A. Bin Sapari, M. L. S. Nai, G. K. Meenashisundaram and M. Gupta, *Mater. Des.*, 2019, **169**, 107683.
20 K. Schindhelm and B. K. Milthorpe, *Australas. Phys. Eng. Sci. Med.*, 1986, **9**, 1000176.
21 M. Heiden, E. Walker and L. Stanciu, *J. Biotechnol. Biomater.*, 2015, **5**(2), 1–9.
22 L. Tan, X. Yu, P. Wan and K. Yang, *J. Mater. Sci. Technol.*, 2013, **29**, 503–513.
23 Y. F. Zheng, X. N. Gu and F. Witte, *Mater. Sci. Eng., R*, 2014, **77**, 1–34.
24 H. Hermawan, *Prog. Biomater.*, 2018, **7**, 93–110.
25 S. Todros, M. Todesco and A. Bagno, *Processes*, 2021, **9**, 1949.
26 F. Witte and A. Eliezer, *Degradation of Implant Materials*, 2012, 9781461439, pp. 93–109.
27 D. Hernández-Escobar, S. Champagne, H. Yilmazer, B. Dikici, C. J. Boehlert and H. Hermawan, *Acta Biomater.*, 2019, **97**, 1–22.
28 G. L. Song, *Corrosion of magnesium alloys*, 2011.
29 G. L. Song and A. Atrens, *Adv. Eng. Mater.*, 1999, **1**, 11–33.
30 G. Song, *Adv. Eng. Mater.*, 2005, **7**, 563–586.
31 K. Gusieva, C. H. J. Davies, J. R. Scully and N. Birbilis, *Int. Mater. Rev.*, 2015, **60**, 169–194.
32 S. V. Dorozhkin, *Surface Modification of Magnesium and Its Alloys for Biomedical Applications*, 2015, vol. 2, pp. 151–191.
33 J. Zhou, Y. Yang, M. Alonso Frank, R. Detsch, A. R. Boccaccini and S. Virtanen, *ACS Appl. Mater. Interfaces*, 2016, **8**, 26482–26492.
34 S. Bandekian, M. Z. Baghbaderani, J. W. Drelich, S. Sharif, A. F. Ismail and H. R. Bakhsheshi-Rad, *J. Mater. Res. Technol.*, 2025, **36**, 5484–5508.
35 F. Badkoobeh, H. Mostaan, M. Rafiei, H. R. Bakhsheshi-Rad, S. RamaKrishna and X. Chen, *J. Magnesium Alloys*, 2023, **11**, 801–839.
36 N. Sezer, Z. Evis and M. Koç, *J. Magnesium Alloys*, 2021, **9**, 392–415.
37 E. Khalid, A. B. Radwan, M. M. Rehman, N. E. Putra, L. E. Fratila-Apachitei, J. Zhou, A. A. Zadpoor and N. Al-Qahtani, *Mater. Adv.*, 2025, **6**, 7685–7721.
38 J. Venezuela and M. S. Dargusch, *Acta Biomater.*, 2019, **87**, 1–40.
39 V. P. M. Rabeeh and T. Hanas, *Prog. Biomater.*, 2022, **11**, 163–191.
40 J. Čapek, D. Vojtěch and A. Oborná, *Mater. Des.*, 2015, **83**, 468–482.
41 Z. S. Seyedraoufi and S. Mirdamadi, *J. Mech. Behav. Biomed. Mater.*, 2013, **21**, 1–8.
42 J. G. Miranda-Hernández, H. Herrera-Hernández, C. O. González-Morán, J. N. Rivera Olvera, I. Estrada-Guel and F. Botello Villa, *Advances in Materials Science and Engineering*, 2017, 7967848.
43 A. Mahajan and S. S. Sidhu, *Materials Technology*, 2018, **33**, 93–105.
44 M. Razavi and Y. Huang, *Biomater. Sci.*, 2019, **7**, 2241–2263, DOI: 10.1039/c9bm00289h.
45 K. Saptaji, M. A. Gebremariam and M. A. B. M. Azhari, *Int. J. Adv. Des. Manuf. Technol.*, 2018, **97**, 2255–2292.
46 B. K. Mahajan, X. Yu, W. Shou, H. Pan and X. Huang, *Small*, 2017, **13**, 1700065.
47 J. He, F. L. He, D. W. Li, Y. L. Liu, Y. Y. Liu, Y. J. Ye and D. C. Yin, *RSC Adv.*, 2016, **6**, 112819–112838.
48 P. Kustra, A. Milenin, B. Płonka and T. Furushima, *J. Mater. Eng. Perform.*, 2016, **25**, 2528–2535.
49 Y. Wang, P. Fu, N. Wang, L. Peng, B. Kang, H. Zeng, G. Yuan and W. Ding, *Engineering*, 2020, **6**, 1267–1275.
50 S. Bose, D. Ke, H. Sahasrabudhe and A. Bandyopadhyay, *Prog. Mater. Sci.*, 2018, **93**, 45–111.
51 T. DebRoy, H. L. Wei, J. S. Zuback, T. Mukherjee, J. W. Elmer, J. O. Milewski, A. M. Beese, A. Wilson-Heid, A. De and W. Zhang, *Prog. Mater. Sci.*, 2018, **92**, 112–224.

52 A. Bandyopadhyay, S. Ciliveri and S. Bose, *J. Indian Inst. Sci.*, 2022, **102**, 561–584.
53 M. Javaid, A. Haleem, R. P. Singh, R. Suman and S. Rab, *Adv. Ind. Eng. Polym. Res.*, 2021, **4**, 312–322, DOI: 10.1016/j.aiepr.2021.07.005.
54 S. Ford and M. Despeisse, *J. Clean. Prod.*, 2016, **137**, 1573–1587.
55 S. A. M. Tofail, E. P. Koumoulos, A. Bandyopadhyay, S. Bose, L. O'Donoghue and C. Charitidis, *Materials Today*, 2018, **21**, 22–37.
56 A. Bandyopadhyay, K. D. Traxel, M. Lang, M. Juhasz, N. Eliaz and S. Bose, *Mater Today*, 2022, **56**, 207–224, DOI: 10.1016/j.mattod.2021.11.026.
57 T. Moritz and S. Maleksaeedi, *Additive Manufacturing: Materials, Processes, Quantifications and Applications*, 2018, 105–161.
58 Y. Wang, P. Fu, N. Wang, L. Peng, B. Kang, H. Zeng, G. Yuan and W. Ding, *Engineering*, 2020, **6**, 1267–1275.
59 B. Zhang, H. Liao and C. Coddet, *Mater. Des.*, 2012, **34**, 753–758.
60 N. A. Zumdick, L. Jauer, L. C. Kersting, T. N. Kutz, J. H. Schleifenbaum and D. Zander, *Mater. Charact.*, 2019, **147**, 384–397.
61 Y. Li, J. Zhou, P. Pavanram, M. A. Leeflang, L. I. Fockaert, B. Pouran, N. Tümer, K. U. Schröder, J. M. C. Mol, H. Weinans, H. Jahr and A. A. Zadpoor, *Acta Biomater.*, 2018, **67**, 378–392.
62 C. C. Ng, M. M. Savalani, M. L. Lau and H. C. Man, *Appl. Surf. Sci.*, 2011, **257**, 7447–7454.
63 Y. Yang, P. Wu, X. Lin, Y. Liu, H. Bian, Y. Zhou, C. Gao and C. Shuai, *Virtual Phys. Prototyp.*, 2016, **11**, 173–181.
64 D. Hu, Y. Wang, D. Zhang, L. Hao, J. Jiang, Z. Li and Y. Chen, *Mater. Manuf. Processes*, 2015, **30**, 1298–1304.
65 P. Sotoudehbagha, S. Sheibani, M. Khakbiz, S. Ebrahimi-Barough and H. Hermawan, *Mater. Sci. Eng., C*, 2018, **88**, 88–94.
66 C. Liu, M. Zhang and C. Chen, *Mater. Sci. Eng., A*, 2017, **703**, 359–371.
67 Y. Yang, P. Wu, Q. Wang, H. Wu, Y. Liu, Y. Deng, Y. Zhou and C. Shuai, *Materials*, 2016, **9**(4), 216.
68 Q. Deng, Y. Wu, Y. Luo, N. Su, X. Xue, Z. Chang, Q. Wu, Y. Xue and L. Peng, *Mater. Charact.*, 2020, **165**, 110377.
69 K. Wei, Z. Wang and X. Zeng, *Mater. Lett.*, 2015, **156**, 187–190.
70 C. Shuai, Y. Yang, P. Wu, X. Lin, Y. Liu, Y. Zhou, P. Feng, X. Liu and S. Peng, *J. Alloys Compd.*, 2017, **691**, 961–969.
71 C. Shuai, Y. Zhou, X. Lin, Y. Yang, C. Gao, X. Shuai, H. Wu, X. Liu, P. Wu and P. Feng, *J. Mater. Sci. Mater. Med.*, 2017, **28**, 13.
72 K. Wei, M. Gao, Z. Wang and X. Zeng, *Mater. Sci. Eng., A*, 2014, **611**, 212–222.
73 G. K. Meenashisundaram, N. Wang, S. Maskomani, S. Lu, S. K. Anantharajan, S. T. Dheen, S. M. L. Nai, J. Y. H. Fuh and J. Wei, *Mater. Sci. Eng., C*, 2020, **108**, 110478.
74 D. D. Lima, K. N. Campo, S. T. Button and R. Caram, *Mater. Des.*, 2020, **196**, 109161.
75 Y. Qin, P. Wen, H. Guo, D. Xia, Y. Zheng, L. Jauer, R. Poprawe, M. Voshage and J. H. Schleifenbaum, *Acta Biomater.*, 2019, **98**, 3–22, DOI: 10.1016/j.actbio.2019.04.046.
76 C. C. Ng, M. M. Savalani, H. C. Man and I. Gibson, *Virtual Phys. Prototyp.*, 2010, **5**, 13–19.
77 A. Kumar, M. Yadav, C. P. Paul, S. Mishra, S. Suwas and K. Chatterjee, *Mater. Adv.*, 2025, **6**, 6243–6256.
78 K. Nopová, J. Jaroš, O. Červinek, L. Pantělejev, S. Gneiger, S. Senck and D. Koutný, *Appl. Sci.*, 2023, **13**, 1377.
79 X. Wu, J. Liu, Y. Yang, J. Bai, C. Shuai, J. Buhagiar and X. Ning, *Int. J. Extreme Manuf.*, 2024, **7**, 022007.
80 J. Dong, Y. Li, P. Lin, M. A. Leeflang, S. van Asperen, K. Yu, N. Tümer, B. Norder, A. A. Zadpoor and J. Zhou, *Acta Biomater.*, 2020, **114**, 497–514.
81 Y. Wang, P. Fu, N. Wang, L. Peng, B. Kang, H. Zeng, G. Yuan and W. Ding, *Engineering*, 2020, **6**, 1267–1275.
82 K. Lietaert, W. Baekelant, L. Thijs, J. Vleugels and P. Mellin, Direct metal printing of zinc: From single laser tracks to high density parts – KU Leuven, https://kuleuven.limo.libis.be/discovery/fulldisplay?docid=lirias1561649&context=SearchWebhook&vid=32KUL_KUL:Lirias&search_scope=lirias_profile&adaptor=SearchWebhook&tab=LIRIAS&query=any,contains,LIRIAS1561649&offset=0, (accessed 9 April 2026).
83 A. G. Demir, L. Monguzzi and B. Previtali, *Addit. Manuf.*, 2017, **15**, 20–28.
84 P. Wen, M. Voshage, L. Jauer, Y. Chen, Y. Qin, R. Poprawe and J. H. Schleifenbaum, *Mater. Des.*, 2018, **155**, 36–45.
85 Y. Qin, P. Wen, M. Voshage, Y. Chen, P. G. Schückler, L. Jauer, D. Xia, H. Guo, Y. Zheng and J. H. Schleifenbaum, *Mater. Des.*, 2019, **181**, 107937.
86 Y. Yang, F. Yuan, C. Gao, P. Feng, L. Xue, S. He and C. Shuai, *J. Mech. Behav. Biomed. Mater.*, 2018, **82**, 51–60.
87 C. Shuai, L. Xue, C. Gao, Y. Yang, S. Peng and Y. Zhang, *Virtual Phys. Prototyp.*, 2018, **13**, 146–154.
88 M. Voshage, S. Megahed, P. G. Schückler, P. Wen, Y. Qin, L. Jauer, R. Poprawe and J. H. Schleifenbaum, *Mater. Today Commun.*, 2022, **32**, 103805.
89 C. Gao, C. Li, S. Peng and C. Shuai, *Chin. J. Mech. Eng.: Addit. Manuf. Front.*, 2022, **1**, 100022.
90 Y. Qin, H. Yang, A. Liu, J. Dai, P. Wen, Y. Zheng, Y. Tian, S. Li and X. Wang, *Acta Biomater.*, 2022, **142**, 388–401.
91 P. Wen, L. Jauer, M. Voshage, Y. Chen, R. Poprawe and J. H. Schleifenbaum, *J. Mater. Process. Technol.*, 2018, **258**, 128–137.
92 Y. Qin, A. Liu, H. Guo, Y. Shen, P. Wen, H. Lin, D. D. Xia, M. Voshage, Y. Tian and Y. Zheng, *Acta Biomater.*, 2022, **145**, 403–415.
93 Y. Yang, M. Yang, C. He, F. Qi, D. Wang, S. Peng and C. Shuai, *Composites, Part B*, 2021, **216**, 108882.
94 A. Kumar, M. Yadav and P. Sharma, *Prog. Addit. Manuf.*, 2025, **10**, 8509–8522.
95 D. T. Chou, D. Wells, D. Hong, B. Lee, H. Kuhn and P. N. Kumta, *Acta Biomater.*, 2013, **9**, 8593–8603.
96 D. Hong, D. T. Chou, O. I. Velikokhatnyi, A. Roy, B. Lee, I. Swink, I. Issaev, H. A. Kuhn and P. N. Kumta, *Acta Biomater.*, 2016, **45**, 375–386.
97 P. Sharma, A. Kumar and A. Kumar, *Mater. Lett.*, 2025, **380**, 137701.

98 D. K. Mishra and P. M. Pandey, *Mater. Sci. Eng., A*, 2020, **783**, 139293.
99 P. Sharma and P. M. Pandey, *Mater. Sci. Eng., C*, 2019, **99**, 838–852.
100 T. Huang, J. Cheng, D. Bian and Y. Zheng, *J. Biomed. Mater. Res., Part B*, 2016, **104**, 225–240.
101 P. Sharma and P. M. Pandey, *Mater. Des.*, 2018, **160**, 442–454.
102 D. K. Mishra and P. M. Pandey, *Mater. Sci. Eng., A*, 2021, **804**, 140759.
103 Y. Li, H. Jahr, P. Pavanram, F. S. L. Bobbert, U. Puggi, X. Y. Zhang, B. Pouran, M. A. Leeflang, H. Weinans, J. Zhou and A. A. Zadpoor, *Acta Biomater.*, 2019, **96**, 646–661.
104 D. Palousek, L. Pantelejev, T. Zikmund and D. Koutny, *MM Sci. J.*, 2017, 1738–1743.
105 B. Song, S. Dong, S. Deng, H. Liao and C. Coddet, *Opt. Laser Technol.*, 2014, **56**, 451–460.
106 C. Shuai, W. Yang, Y. Yang, H. Pan, C. He, F. Qi, D. Xie and H. Liang, *Mater. Res. Express*, 2020, **7**, 015404.
107 D. Carluccio, C. Xu, J. Venezuela, Y. Cao, D. Kent, M. Bermingham, A. G. Demir, B. Previtali, Q. Ye and M. Dargusch, *Acta Biomater.*, 2020, **103**, 346–360.
108 J. K. Saha, R. Samanta, G. Mandal, M. Yadav and S. K. Ghosh, *Sādhanā*, 2024, **49**, 300.
109 S. K. Ghosh and M. Yadav, *Advances in Solid-State Welding and Processing of Metallic Materials*, CRC Press, 2025, pp. 17–34, DOI: 10.1201/9781003513926-3.
110 S. K. Ghosh and M. Yadav, *J. Mater. Eng. Perform.*, 2025, **35**, 11759–11774.
111 *Additive Manufacturing for Biomedical Applications: Recent Trends and Challenges*, ed. A. Dixit, A. Kumar and D. K. Pathak, 2024, DOI: 10.1007/978-981-97-5456-4.
112 *Biodegradable Metallic Materials: Design, Development and Characterization*, ed. A. Dixit, A. Kumar and D. K. Pathak, 2025, DOI: 10.1007/978-981-95-2401-3.
113 V. K. Gupta, N. K. Tewary, M. Yadav and S. K. Ghosh, *Metallogr., Microstruct., Anal.*, 2022, **11**, 602–616.
114 S. K. Ghosh and M. Yadav, *Met. Sci. Heat Treat.*, 2024, **66**, 237–242.
115 S. K. Ghosh and M. Yadav, *Materwiss. Werksttech.*, 2023, **54**, 676–692.
116 M. Yadav and S. K. Ghosh, *Metallogr., Microstruct., Anal.*, 2026, DOI: 10.1007/s13632-026-01314-6.
117 S. K. Ghosh and M. Yadav, *Metallogr., Microstruct., Anal.*, 2024, **13**, 817–831.
118 M. Ahmadi, S. A. A. B. Tabary, D. Rahmatabadi, M. S. Ebrahimi, K. Abrinia and R. Hashemi, *J. Mater. Res. Technol.*, 2022, **19**, 1537–1562.
119 D. Schmid, J. Renza, M. F. Zaeh and J. Glasschroeder, *Phys. Procedia*, 2016, **83**, 927–936.
120 M. Salehi, H. L. Seet, M. Gupta, H. Farnoush, S. Maleksaeedi and M. L. S. Nai, *Addit. Manuf.*, 2021, **37**, 101655.
121 I. Antoniac, D. Popescu, A. Zapciu, A. Antoniac, F. Miculescu and H. Moldovan, *Materials*, 2019, **12**, 1–13.
122 A. Kumar and P. M. Pandey, *J. Magnesium Alloys*, 2021, **9**, 1989–2008.
123 D. K. Pathak and P. M. Pandey, *J. Mater. Eng. Perform.*, 2021, **30**, 3510–3523.
124 J. Chen, P. Wu, Q. Wang, Y. Yang, S. Peng, Y. Zhou, C. Shuai and Y. Deng, *Metals*, 2016, **6**, 259.
125 H. Okuda, T. Horiuchi, T. Tsukamoto and S. Ochiai, *Scr. Mater.*, 2013, **68**, 575–578.
126 P. Wen, Y. Qin, Y. Chen, M. Voshage, L. Jauer, R. Poprawe and J. H. Schleifenbaum, *J. Mater. Sci. Technol.*, 2019, **35**, 368–376.
127 C. Yao, Z. Wang, S. L. Tay, T. Zhu and W. Gao, *J. Alloys Compd.*, 2014, **602**, 101–107.
128 B. Li, A. Dong, G. Zhu, S. Chu, H. Qian, C. Hu, B. Sun and J. Wang, *Surf. Coat. Technol.*, 2012, **206**, 3989–3999.
129 M. Montani, A. G. Demir, E. Mostaed, M. Vedani and B. Previtali, *Rapid Prototyp. J.*, 2017, **23**, 514–523.
130 J. D. Hunt, *Mater. Sci. Eng.*, 1984, **65**, 75–83.
131 L. Scime and J. Beuth, *Addit. Manuf.*, 2018, **19**, 114–126.
132 L. Thijs, K. Kempen, J. P. Kruth and J. Van Humbeeck, *Acta Mater.*, 2013, **61**, 1809–1819.
133 I. Yadroitsev, I. Yadroitsava and I. Smurov, *Laser-based Micro- and Nanopackaging and Assembly V*, SPIE, 2011, vol. 7921, p. 79210C.
134 K. Zhang, S. Wang, W. Liu and X. Shang, *Mater. Des.*, 2014, **55**, 104–119.
135 H. R. Bakhsheshi-Rad, E. Hamzah, H. T. Low, M. Kasiri-Asgarani, S. Farahany, E. Akbari and M. H. Cho, *Mater. Sci. Eng., C*, 2017, **73**, 215–219.
136 Y. F. Zheng, X. N. Gu and F. Witte, *Mater. Sci. Eng., R*, 2014, **77**, 1–34, DOI: 10.1016/j.mser.2014.01.001.
137 I. Yadroitsev, I. Yadroitsava and I. Smurov, *Laser-based Micro- and Nanopackaging and Assembly V*, SPIE, 2011, vol. 7921, p. 79210C.
138 G. Gąsior, J. Szczepański and A. Radtke, *Materials*, 2021, **14**, 3381.
139 A. R. Khan, N. S. Grewal, C. Zhou, K. Yuan, H. J. Zhang and Z. Jun, *Results in Engineering*, 2023, **20**, 101526.
140 I. Limón, J. Bedmar, J. P. Fernández-Hernán, M. Multigner, B. Torres, J. Rams and S. C. Cifuentes, *Materials*, 2024, **17**, 6220.
141 N. Eliaz, *Degradation of Implant Materials*, Springer New York, NY, 2012.
142 D. Hernández-Escobar, S. Champagne, H. Yilmazer, B. Dikici, C. J. Boehlert and H. Hermawan, *Acta Biomater.*, 2019, **97**, 1–22.
143 M. Yadav, J. K. Saha and S. K. Ghosh, *J. Mater. Eng. Perform.*, 2025, **34**, 1177–1192.
144 M. Yadav, I. Dey and S. K. Ghosh, *Mater. Res. Express*, 2022, **9**, 056504.
145 M. Yadav, J. K. Saha and S. K. Ghosh, *Eng. Res. Express*, 2023, **5**, 015064.
146 I. Dey, P. Manna, M. Yadav, N. K. Tewary, J. K. Saha, S. K. Ghosh, I. Dey, P. Manna, M. Yadav, N. K. Tewary, J. K. Saha and S. K. Ghosh, *Stainless Steels*, IntechOpen, 2021, vol. 1, pp. 1–22.
147 M. Yadav, J. K. Saha and S. K. Ghosh, *Arch. Metall. Mater*, 2024, **69**, 865–879.

148 R. Karunakaran, S. Ortgies, A. Tamayol, F. Bobaru and M. P. Sealy, *Bioact. Mater.*, 2020, **5**, 44–54.
149 B. Das, M. Yadav, S. Kundu and T. Mandal, *Corros. Eng., Sci. Technol.*, 2023, **58**, 124–137.
150 A. Bahmani, S. Arthanari and K. S. Shin, *J. Magnesium Alloys*, 2020, **8**, 134–149.
151 C. Shuai, C. He, P. Feng, W. Guo, C. Gao, P. Wu, Y. Yang and S. Bin, *Virtual Phys. Prototyp.*, 2018, **13**, 59–69.
152 G. Baril and N. Pébère, *Corros. Sci.*, 2001, **43**, 471–484.
153 D. Orlov, K. D. Ralston, N. Birbilis and Y. Estrin, *Acta Mater.*, 2011, **59**, 6176–6186.
154 F. Benn, N. Kröger, M. Zinser, K. van Gaalen, T. J. Vaughan, M. Yan, R. Smeets, E. Bibiza, S. Malinov, F. Buchanan and A. Kopp, *Mater. Sci. Eng., C*, 2021, **124**, 112016.
155 Y. Yang, C. Lu, S. Peng, L. Shen, D. Wang, F. Qi and C. Shuai, *Virtual Phys. Prototyp.*, 2020, **15**, 278–293.
156 N. T. Kirkland and N. Birbilis, *SpringerBriefs in Materials*, 2014, pp. 73–94.
157 D. Li, D. Zhang, Q. Yuan, L. Liu, H. Li, L. Xiong, X. Guo, Y. Yan, K. Yu, Y. Dai, T. Xiao, Y. Li and C. Wen, *Acta Biomater.*, 2022, **141**, 454–465.
158 S. Li, Y. Che, C. Li, Y. Shu, J. He, B. Yang and J. Song, *J. Magnesium Alloys*, 2022, **10**, 721–729.
159 J. Wang, L. Xu, R. Wu, J. Feng, J. Zhang, L. Hou and M. Zhang, *Acta Metall. Sin.*, 2020, **33**, 490–499.
160 M. Yadav, A. Kumar and G. C. Verma, *Additive Manufacturing for Biomedical Applications: Recent Trends and Challenges*, Springer Nature, 2024, pp. 105–160, DOI: 10.1007/978-981-97-5456-4_7.
161 D. K. Pathak and P. M. Pandey, *J. Biomed. Mater. Res., Part B*, 2021, **109**, 436–450.
162 P. Das, D. K. Pathak, P. Sharma and P. M. Pandey, *Corrosion Reviews*, 2025, **43**, 279–300.
163 C. Shuai, L. Xue, C. Gao, Y. Yang, S. Peng and Y. Zhang, *Virtual Phys. Prototyp.*, 2018, **13**, 146–154.
164 J. Liu, B. Yin, P. Wen and Y. Tian, Proc. SPIE, Advanced Laser Processing and Manufacturing V, 2021, vol. 11892, pp. 9–19, DOI: 10.1117/12.2601287.
165 P. K. Bowen, J. Drelich and J. Goldman, *Adv. Mater.*, 2013, **25**, 2577–2582.
166 M. Peuster, P. Wohlsein, M. Brügmann, M. Ehlerding, K. Seidler, C. Fink, H. Brauer, A. Fischer, G. Hausdorf and I. Care, *Heart*, 2001, **1000**, 563–569.
167 H. Hermawan, D. Dubé and D. Mantovani, *J. Biomed. Mater. Res. A*, 2010, **93**, 1–11.
168 H. Hermawan, D. Dubé and D. Mantovani, *Advanced Materials Research*, Trans Tech Publications, 2007, vol. 15–17, pp. 107–112.
169 M. Schinhammer, I. Gerber, A. C. Hänzi and P. J. Uggowitzer, *Mater. Sci. Eng., C*, 2013, **33**, 782–789.
170 M. Schinhammer, A. C. Hänzi, J. F. Löffler and P. J. Uggowitzer, *Acta Biomater.*, 2010, **6**, 1705–1713.
171 S. Gambaro, C. Paternoster, B. Occhionero, J. Fiocchi, C. A. Biffi, A. Tuissi and D. Mantovani, *Mater. Today Commun.*, 2021, **27**, 102250.
172 A. M. Roman, V. Geantă, R. Cimpoeşu, C. Munteanu, N. M. Lohan, G. Zegan, E. R. Cernei, I. Ioniţă, N. Cimpoeşu and N. Ioanid, *Materials*, 2022, **15**, 568.
173 C. Tonna, C. Wang, D. Mei, S. V. Lamaka, M. L. Zheludkevich and J. Buhagiar, *Bioact. Mater.*, 2022, **7**, 426–440.
174 M. Yadav, A. Kumar, D. Kumar, S. Nilawar, M. Amirthalingam, S. Suwas and K. Chatterjee, *J. Mater. Chem. B*, 2025, **13**, 8844–8865.
175 A. Kumar, I. A. Palani and M. Yadav, *Mater. Today Commun.*, 2024, **38**, 107881.
176 P. Sharma, K. G. Jain, P. M. Pandey and S. Mohanty, *Mater. Sci. Eng., C*, 2020, **106**, 110247.
177 D. Hong, D. T. Chou, O. I. Velikokhatnyi, A. Roy, B. Lee, I. Swink, I. Issaev, H. A. Kuhn and P. N. Kumta, *Acta Biomater.*, 2016, **45**, 375–386.
178 D. K. Mishra and P. M. Pandey, *J. Biomed. Mater. Res., Part B*, 2022, **110**, 1439–1459.
179 H. Hermawan, D. Dubé and D. Mantovani, *Acta Biomater.*, 2010, **6**, 1693–1697.
180 J. Liu, S. Zhao, X. Zhang, X. Lin and Y. Hu, *J. Manuf. Process.*, 2022, **82**, 657–664.
181 B. Wegener, A. Sichler, S. Milz, C. Sprecher, K. Pieper, W. Hermanns, V. Jansson, B. Nies, B. Kieback, P. E. Müller, V. Wegener and P. Quadbeck, *Scientific Reports*, 2020, **10**, 9141.
182 H. Kabir, K. Munir, C. Wen and Y. Li, *Bioact. Mater.*, 2021, **6**, 836–879.
183 A. Gracheva, I. Polozov and A. Popovich, *Metals*, 2025, **15**, 754.
184 B. Song, S. Dong, S. Deng, H. Liao and C. Coddet, *Opt. Laser Technol.*, 2014, **56**, 451–460.
185 T. Huang, J. Cheng, D. Bian and Y. Zheng, *J. Biomed. Mater. Res., Part B*, 2016, **104**, 225–240.
186 J. W. Drelich, M. Sikora-Jasinska, E. Mostaed, H. Liu, P. Maier, J. M. Seitz and N. Hort, *JOM*, 2020, **72**, 1830–1832.
187 R. Karunakaran, S. Ortgies, A. Tamayol, F. Bobaru and M. P. Sealy, *Bioact. Mater.*, 2020, **5**, 44–54.
188 A. Kumar and P. M. Pandey, *Mater. Manuf. Processes*, 2021, **36**, 1365–1376.
189 F. Witte, *Acta Biomater.*, 2010, **6**, 1680–1692.
190 F. Bär, L. Berger, L. Jauer, G. Kurtuldu, R. Schäublin, J. H. Schleifenbaum and J. F. Löffler, *Mater. Sci. Eng., C*, 2021, **124**, 112016.
191 L. Zhang, J. Pei, H. Wang, Y. Shi, J. Niu, F. Yuan, H. Huang, H. Zhang and G. Yuan, *ACS Appl. Mater. Interfaces*, 2017, **9**, 9437–9448.
192 B. Liu and Y. F. Zheng, *Acta Biomater.*, 2011, **7**, 1407–1420.
193 M. Moravej, F. Prima, M. Fiset and D. Mantovani, *Acta Biomater.*, 2010, **6**, 1726–1735.
194 S. Zhu, N. Huang, L. Xu, Y. Zhang, H. Liu, H. Sun and Y. Leng, *Mater. Sci. Eng., C*, 2009, **29**, 1589–1592.
195 F. Witte, J. Fischer, J. Nellesen, H. A. Crostack, V. Kaese, A. Pisch, F. Beckmann and H. Windhagen, *Biomaterials*, 2006, **27**, 1013–1018.
196 X. N. Gu, W. R. Zhou, Y. F. Zheng, Y. Cheng, S. C. Wei, S. P. Zhong, T. F. Xi and L. J. Chen, *Acta Biomater.*, 2010, **6**, 4605–4613.

197 H. Windhagen, K. Radtke, A. Weizbauer, J. Diekmann, Y. Noll, U. Kreimeyer, R. Schavan, C. Stukenborg-Colsman and H. Waizy, *Biomed. Eng. Online*, 2013, **12**, 62.
198 H. Waizy, A. Weizbauer, C. Modrejewski, F. Witte, H. Windhagen, A. Lucas, M. Kieke, B. Denkena, P. Behrens, A. Meyer-Lindenberg, F. W. Bach and F. Thorey, *Biomed. Eng. Online*, 2012, **11**, 12.
199 S. Bahrani, S. A. Hashemi, S. M. Mousavi and R. Azhdari, *Drug Metab. Rev.*, 2019, **51**, 356–377.
200 K. Chen, P. Li, Q. Guan, X. Gu, L. Zhao, L. Huang, C. Huang, Y. Qin, C. Yu, T. Zhang, H. Li, Y. Huang and Y. Zheng, *Adv. Sci.*, 2025, **12**, e06513.
201 M. Peuster, C. Hesse, T. Schloo, C. Fink, P. Beerbaum and C. von Schnakenburg, *Biomaterials*, 2006, **27**, 4955–4962.
202 Z. Wang, B. Liu, B. Yin, Y. Zheng, Y. Tian and P. Wen, *Front. Chem.*, 2022, **10**, 1066103.
203 B. Peng, H. Xu, F. Song, P. Wen, Y. Tian and Y. Zheng, *J. Mater. Sci. Technol.*, 2024, **182**, 79–110.
204 R. E. Hendea, D. Raducanu, A. Nocivin, S. Ivanescu, D. Stanciu, C. Trisca-Rusu, R. S. Campian, S. I. Drob, V. D. Cojocaru and B. M. Gălbinaşu, *Materials*, 2022, **15**, 2561.
205 F. Meng and Y. Du, *Materials*, 2024, **17**, 4309.
206 K. Chen, J. Dong, N. E. Putra, J. Li, M. Klimopoulou, M. A. Leeflang, L. E. Fratila-Apachitei, J. Zhou and A. A. Zadpoor, *Acta Biomater*, 2026, **213**, 737–756.
207 Y. Li, P. Pavanram, J. Zhou, K. Lietaert, F. S. L. Bobbert, Y. Kubo, M. A. Leeflang, H. Jahr and A. A. Zadpoor, *Biomater. Sci.*, 2020, **8**, 2404–2419.
208 D. Carluccio, M. Bermingham, D. Kent, A. G. Demir, B. Previtali and M. S. Dargusch, *Adv. Eng. Mater.*, 2019, **21**, 1900049.
209 Y. Li, K. Lietaert, W. Li, X. Y. Zhang, M. A. Leeflang, J. Zhou and A. A. Zadpoor, *Corros. Sci.*, 2019, **156**, 106–116.
210 F. Wang, Q. Tan, T. Liu, J. Venezuela, Z. Shi, S. Hurley, A. Ly, C. Xu, D. U. Erbulurt, J. Yin, Y. Zhao and M. Zhang, *Addit. Manuf. Lett.*, 2025, **15**, 100321.
211 C. He, S. Bin, P. Wu, C. Gao, P. Feng, Y. Yang, L. Liu, Y. Zhou, M. Zhao, S. Yang and C. Shuai, *Metals*, 2017, **7**, 105.
212 L. Liu, F. Yuan, M. Zhao, C. Gao, P. Feng, Y. Yang, S. Yang and C. Shuai, *Materials*, 2017, **10**, 477.
213 C. Shuai, L. Liu, M. Zhao, P. Feng, Y. Yang and W. Guo, *J. Mater. Sci. Technol.*, 2018, **34**, 1944–1952.
214 K. Lietaert and K. U. Leuven, *World PM2016-AM-Special Aspects in AM Powders Direct Metal Printing of Zinc: From Single Laser Tracks to High Density Parts*, 2016.
215 M. Montani, A. G. Demir, E. Mostaed, M. Vedani and B. Previtali, *Rapid Prototyp. J.*, 2017, **23**, 514–523.
216 T. DebRoy, T. Mukherjee, H. L. Wei, J. W. Elmer and J. O. Milewski, *Nat. Rev. Mater.*, 2020, **6**, 48–68.
217 B. Basu, N. H. Gowtham, Y. Xiao, S. R. Kalidindi and K. W. Leong, *Acta Biomater.*, 2022, **143**, 1–25.
218 H. L. Wei, T. Mukherjee, W. Zhang, J. S. Zuback, G. L. Knapp, A. De and T. DebRoy, *Prog. Mater. Sci.*, 2021, **116**, 100703.
219 W. Zhang, A. Mehta, P. S. Desai and C. F. Higgs, Solid Freeform Fabrication 2017: Proceedings of the 28th Annual International Solid Freeform Fabrication Symposium – An Additive Manufacturing Conference, 2017, pp. 1235–1248.
220 S. Gerdes, A. Gaikwad, S. Ramesh, I. V. Rivero, A. Tamayol and P. Rao, *J. Intell. Manuf.*, 2024, **35**, 1055–1077.
221 K. Xue, F. K. Wang, A. Suwardi, M. Y. Han, P. Teo, P. Wang, S. Wang, E. Ye, Z. Li and X. J. Loh, *Mater. Today Bio*, 2021, **12**, 100165.
222 G. Al-Kharusi, N. J. Dunne, S. Little and T. J. Levingstone, *Bioengineering*, 2022, **9**, 561.
223 Y. Li, H. Jahr, J. Zhou and A. A. Zadpoor, *Acta Biomater.*, 2020, **115**, 29–50.
224 T. DebRoy, T. Mukherjee, J. O. Milewski, J. W. Elmer, B. Ribic, J. J. Blecher and W. Zhang, *Nat. Mater.*, 2019, **18**, 1026–1032.
225 Y. Du, T. Mukherjee, N. Finch, A. De and T. DebRoy, *J. Manuf. Process.*, 2022, **81**, 65–77.
226 M. Javaid, A. Haleem, R. P. Singh, R. Suman and S. Rab, *Adv. Ind. Eng. Polym. Res.*, 2021, **4**, 312–322.
227 A. Bandyopadhyay, I. Mitra, S. B. Goodman, M. Kumar and S. Bose, *Prog. Mater. Sci.*, 2023, **133**, 101053.
228 N. E. Putra, M. J. Mirzaali, I. Apachitei, J. Zhou and A. A. Zadpoor, *Acta Biomater.*, 2020, **109**, 1–20.
229 A. Bandyopadhyay and B. Heer, *Mater. Sci. Eng., R*, 2018, **129**, 1–16.
230 E. A. Guzzi and M. W. Tibbitt, *Adv. Mater.*, 2020, **32**, 1901994.
231 X. Yao, J. Tang, Y. Zhou, A. Atrens, M. S. Dargusch, B. Wiese, T. Ebel and M. Yan, *J. Magnesium Alloys*, 2021, **9**, 2155–2168.
232 C. Shuai, Y. Cheng, Y. Yang, S. Peng, W. Yang and F. Qi, *J. Alloys Compd.*, 2019, **798**, 606–615.
233 A. Kumar and P. M. Pandey, *Proc. Inst. Mech. Eng., Part C*, 2021, **235**, 2416–2425.